Fabrication and Characterization of Polyvinylidene Fluoride Materials

With and Without Conductive Fillers for Selective Applications

Prissana Rakbamrung

A Thesis Submitted in Fulfillment of the Requirements

for the Degree of Doctor of Philosophy in Physics

Prince of Songkla University

2011

Thesis Title   Fabrication and Characterization of Polyvinylidene Fluoride Materials With and Without Conductive Fillers for Selective Applications

Author   Ms. Prissana Rakbamrung

Major Program   Physics

Major Advisor :

…………………………………...
(Assoc. Prof. Dr. Nantakan Muensit)

Examining Committee :

………………………..………..Chairperson
(Prof. Dr. Tawee Tunkasiri)

………………………………………
(Assoc. Prof. Dr. Nantakan Muensit)

………………………….……..
(Dr. Chanchana Thanachayanont)

……………………………….
(Asst. Prof. Dr. Saad Riyajan)

The Graduate School, Prince of Songkla University, has approved this thesis as fulfillment of the requirements for the Doctor of Philosophy Degree in Physics

………………………………………
(Prof. Dr. Amornrat Phongdara)
Dean of Graduate School

ชื่อวิทยานิพนธ์ การเตรียมและศึกษาลักษณะเฉพาะวัสดุพอลิไวนิลิดีนฟลูออไรด์ที่เติมและไม่เติม
ตัวนำไฟฟ้าเพื่อการประยุกต์ใช้งานเฉพาะอย่าง

ผู้เขียน นางสาวปริศนา รักบำรุง

สาขาวิชา ฟิสิกส์

ปีการศึกษา 2553

บทคัดย่อ

งานวิจัยนี้นำเสนอการเตรียมและการปรับปรุงคุณสมบัติของพอลิเมอร์
พอลิไวนิลิดีนฟลูออไรด์ หรือ PVDF โดยการเติมอนุภาคนำไฟฟ้าซึ่งมีความหนาแน่นต่ำ แต่ความ
หนาแน่นอิเล็กตรอนสูง เช่น อนุภาคทองแดง ทั้งระดับไมโครเมตรและนาโนเมตร และได้เลือกใช้
สารลดแรงตึงผิวชนิดไม่มีขั้ว คือ ไกลคอลโดเดซิลอีเธอร์ หรือ Brij-30 เพื่อช่วยให้การกระจายตัว
ของทองแดงในเมทริก PVDF ดีขึ้น พบว่าสามารถเติมทองแดงเป็นสัดส่วนปริมาตรสูงถึง 0.7 ซึ่ง
เป็นผลให้ PVDF ที่เตรียมขึ้นด้วยการหล่อบาง มีการนำไฟฟ้าสูง และจากการเปลี่ยนแปลงอย่าง
รวดเร็วของการนำไฟฟ้าและค่าคงที่ไดอิเล็กทริกนี้เอง ทำให้ได้เปอร์โคเลชันของคอมโพสิทที่
สัดส่วนการเติมทองแดงโดยปริมาตรเท่ากับ 0.6 มีค่าคงที่ไดอิเล็กทริกที่ 1 กิโลเฮิรตซ์สูงถึง 8 ทั้งๆ
ที่ยังไม่ได้โพล ซึ่งปกติจะมีค่าเพียง 2-3 สำหรับ PVDF บริสุทธิ์ แต่อย่างไรก็ตามการสูญเสีย
ไดอิเล็กทริกมีค่าสูงเกินไป ในขณะที่เมื่อเติมอนุภาคทองแดงระดับนาโนในปริมาณน้อย ส่งผลให้
ค่าคงที่ไดอิเล็กทริกย่านความถี่ต่ำ (100 Hz) สูงประมาณ 50 ซึ่งเป็นค่าที่เป็นประโยชน์ในการเก็บ
เกี่ยวพลังงาน และเนื่องจากการเก็บเกี่ยวพลังงานได้มีการพัฒนาเร็วๆนี้ ให้สามารถใช้งานใน
เทคโนโลยีด้านเซนเซอร์ไร้สาย และอุปกรณ์อิเล็กทรอนิกส์แบบพกพา งานวิจัยนี้จึงสนใจการใช้
PVDF และคอมโพสิทในงานด้านการเก็บเกี่ยวพลังงาน ดังนั้นเพื่อเพิ่มความเป็นผลึกและสมบัติ
ไพอิโซอิเล็กทริก PVDF จึงต้องผ่านกระบวนการยืดและโพลิง แต่เนื่องจากก้อนขนาดเล็กมากของ
อนุภาคทองแดงยังคงหลงเหลืออยู่ในเมทริก PVDF ของคอมโพสิท และกลายเป็นจุดก่อตัวของการ
ฉีกขาดในระหว่างทดสอบการสั่นทางกล ดังนั้นงานวิจัยนี้จึงนำ PVDF (ที่ไม่มีตัวเติม) มาเป็นตัว
เก็บเกี่ยวพลังงาน โดยได้ทำการศึกษาการแปลงพลังงานจากการสั่นเชิงกลให้เป็นพลังงานไฟฟ้าด้วย
วิธีการมาตรฐานและวิธีการไม่เป็นเชิงเส้นแบบ SSHI เปรียบเทียบระหว่างวัสดุไพอิโซเซรามิกส์
สองชนิด คือ PMN-PT และ Mn-PZT เมื่อใช้วิธีการมาตรฐาน พลังงานที่เก็บเกี่ยวโดย
PMN-25PT มีค่าเป็น 160 เปอร์เซ็นต์ของ PZT-1mol%Mn ในขณะที่เมื่อใช้วงจร SSHI มีค่า
พลังงานเก็บเกี่ยวสูงกว่าวิธีแรก 3-6 เท่า นอกจากนี้ความสามารถในการแปลงพลังงานของวัสดุทั้ง

สองนี้มีค่าต่างกันเพียงเล็กน้อยในกรณีนี้ แสดงให้เห็นว่าพลังงานที่ได้จากวัสดุไพอิโซเซรามิกส์สูง
เพียงพอที่จะนำไปใช้ในวงจร SSHI ซึ่งทำงานได้เองโดยดึงพลังงานส่วนหนึ่งจากพลังงานเก็บ
เกี่ยว เป็นที่น่าเสียดายว่าเมื่อใช้หลักการเก็บเกี่ยวพลังงานแบบ SSHI กับวัสดุ PVDF ค่าพลังงานที่
เก็บเกี่ยวได้ไม่ปรากฏ ดังนั้นจึงเลือกใช้วงจรมาตรฐานในกรณีนี้ โดยมีการกระตุ้นให้ระบบคานซึ่ง
มี PVDF ติดบนคานสั่นที่เรโซแนนซ์ ช่วง 60-70 เฮิรตซ์ ด้วยแอมปลิจูดการสั่นของคานคงที่
พบว่าพลังงานที่เก็บเกี่ยวได้จาก PVDF มีค่า 2 μW ด้วยโหลดที่สอดคล้องกัน 1.6 MΩ เป็นที่
น่าสนใจว่าถึงแม้วัสดุไพอิโซเซรามิกส์จะสามารถใช้ได้กับเทคนิคไม่เป็นเชิงเส้น แต่ความหนาแน่น
พลังงานมีค่าเพียง 15-30 μW$\cdot$cm^{-3} ซึ่งน้อยกว่าความหนาแน่นพลังงานที่เก็บเกี่ยวได้จาก PVDF
(22-70 μW$\cdot$cm^{-3}) โดยเทคนิคมาตรฐาน ดังนั้น PVDF เหมาะสมเป็นอย่างยิ่งที่จะใช้เป็นตัวเลือก
หนึ่งในการเก็บเกี่ยวพลังงาน และจะเห็นได้ว่าสิ่งสำคัญที่จะต้องพิจารณามีทั้งสมบัติของวัสดุและ
วงจรที่ใช้ และงานวิจัยที่จะดำเนินต่อไปในอนาคตมีความจำเป็นอย่างยิ่งที่จะนำ PVDF ไปใช้ใน
เทคโนโลยีการเก็บเกี่ยวพลังงาน เช่น เซนเซอร์ไร้สาย อุปกรณ์อิเล็กทรอนิกส์แบบพกพา และ
อุปกรณ์อิเล็กทรอนิกส์ที่ขับเคลื่อนด้วยตนเอง

Thesis Title   Fabrication and Characterization of Polyvinylidene Fluoride Materials With and Without Conductive Fillers for Selective Applications

Author   Ms. Prissana Rakbamrung

Major Program Physics

Academic Year 2010

ABSTRACT

This work presents the fabrication of the poly(vinylidene fluoride) or PVDF polymer and alters its material properties by adding conductive filler of low density and high electron density such as micro- and nano-copper into the PVDF matrix. The non-ionic surfactant of glycol dodecyl ether (Brij-30) was chosen to enhance the dispersion of the filler in the PVDF matrix. It was established that the volume fraction of the filler could be as high as its maximal value of 0.7. This resulted in a very high electrical conductivity of the cast PVDF. From an abrupt change in electrical conductivity and dielectric constant, it could be seen that the percolation threshold of the filler in the composite was 0.6. The unpoled composite had a good dielectric constant (1 kHz) of 8 while it was 2-3 for the as-received and unpoled PVDF. However, the dielectric loss was higher as the filler content was larger. It was found that when the nano-copper was used for a small amount, the obtained composite had a good dielectric constant (100 kHz) of about 50. This value is usually useful for energy harvesting applications. As energy harvesting is an advanced application recently developed, it can be integrated into wireless technology and portable electronics, the present work thus focuses on investigating the PVDF and its composite for this selective application, i.e., energy harvesting. In order to enhance the crystallinity and piezoelectric phase, the PVDF sample was stretched and poled. The composite sample was also applied and the mechanical stretched was torn. This was mainly due to the tiny aggregations of the fillers in the polymer which still existed and became the origin of the rupture of the composite. The stretched and poled PVDF (without filler) was, therefore, further studied as a piezoelectric energy harvester. For converting the mechanical vibration into usable electrical energy, the

comparison was first made between two well-known piezoceramics, i.e. PMN-PT and Mn-PZT using either standard or SSHI harvesting circuit. It was found that when using the first, the PMN-25PT gain was 160% to that of PZT-1mol%Mn. By using the latter, the output power was 3-6 times higher than that of the standard one. In addition, there was a slight difference in energy conversion capability the between two compositions. The SSHI power with the piezoceramics was high enough to be dissipated in related circuitry and thus the self-powering vibrating system could be carried out in this case. When the concept of the nonlinear SSHI processing was applied to the PVDF element, the output power was not obtained. The standard circuit was then selected. At a resonance of 60-70 Hz of the vibrating system with the PVDF sample attached onto the beam and a constant amplitude of the displacement of the beam, the output power of 2 μW was delivered by the PVDF element at the matching load of 1.6 MΩ. It is interesting to note that although the piezoceramics were compatible with the nonlinear technique, the power density was 15-30 μW$\cdot$cm^{-3} which is less than that of the PVDF (22-70 μW$\cdot$cm^{-3}) obtained by using the standard approach. Therefore, the PVDF material is highly promising as a candidate in energy harvesting. It is important that both the material property and the interconnected electronics are taken into account. The implementation of the PVDF element into a technological advancement in energy harvesting applications and related technologies such as wireless sensor, portable electronics and self-powered devices is necessary to do further investigation.

ACKNOWLEDGEMENTS

I would like to thank my thesis advisors, Associated Professor Dr. Nantakan Meunsit for her continous support and valuable suggestions. I am grateful to Professor Dr. Daniel Guyomar and Associated Professor Dr. Mickaël Lallart for their help and guidance while I was doing my research in the Laboratoire de Génie Electrique et Ferroélectricité (LGEF), INSA de Lyon, France as well as during their visits to the Prince of Songkla University.

I would like to thank the Examining Committee, Professor Dr. Tawee Tunkasiri, Faculty of Science, Chaing Mai University, Dr.Chanchana Thanachayanont, National Metals and Materials Technology Center, and Assistant Professor Dr. Saad Riyajan, Department of Materials Science and Technology, Faculty of Science, Prince of Songkla University.

I am indebted to the encouragement from my friends in the Material Physics Laboratory, Prince of Songkla University and in the Laboratoire de Génie Electrique et Ferroélectricité (LGEF), INSA de Lyon, France. Finally, I deeply thank you my beloved parents, my aunt, sister and brother, and in particular, Ms. Preeyanan Thepnuan for their love and support throughout the years of my PhD study.

Prissana Rakbamrung

TABLES OF CONTENTS

LIST OF FIGURES (cont.)

LIST OF FIGURES (cont.)

LIST OF TABLES

CHAPTER 1

INTRODUCTION

1.1 Statement of the Problem

Novel materials have always been sought after. One of the most useful materials to date is the development of ferroelectric ceramics in bulk and film forms. So far, ferroelectric ceramics of lead zirconate titanate with various compositions and dopants have been widely used in electrical and electronic devices such as capacitors, actuators, accelerometers, medical ultrasounds, transducers and sensors because of their excellent electromechanical properties. However, public concerns due to toxic elements that can cause serious problems to the environment at all stages from the manufacturing to the recycling of used devices and equipments has driven us to use non-lead materials instead. An outstanding candidate alternative to lead-based ceramics is polyvinylidene fluoride polymer or PVDF. It has been extensively investigated since the first observation of its piezoelectricity in 1969 (Kawai, 1969). In general, polymers have common attractions in a manner that they can be easily processed, are light in weight and flexible. In addition, the development of their integration into modern microsystems also consumes relatively low cost. Specifically, PVDF polymer has long been commercially used in various applications in home and in industries (Lang and Munesit, 2006). PVDF-based materials are thus the subject of this work. Nowadays, several efforts have designed new families of polymers by adding the fillers of different types and sizes in a polymer matrix to produce polymer composites (Fishcher *et al*., 1997; Glatkowski, 2003; Moisala *et al.*, 2006; Rothon, 2002; Smith *et al*., 2004). This work thus aims to study the formation of metal particles in the PVDF matrix and measures the properties of the polymer composites. Novel technologies relating to scavenge energy from ambient vibrations and heat with ferroelectric materials have been developed for about a decade. Ferroelectric materials are of great interest because the coupling between mechanical and electrical properties can be done through piezoelectric activity while the thermal and electrical

1

mechanisms can be coupled through pyroelectricity. In order to make use of the energy harvested in ambient, the researches on micro-energy harvester which is designed to provide micro-watts of power to enable smart sensors to indefinitely function have become an exciting area. Recently, PVDF has been recognized for thermal energy harvesting (Cuadras *et al*., 2010; Ng *et al*., 2000; Sebald *et al*., 2008; Xie *et al*., 2010). PVDF-inserted shoe is a typical example of a piezoelectric harvester powering an interconnected force transducer while walking (Razian and Pepper, 2003). To increase the potential in commercial sectors of PVDF the present work aims to study the use of PVDF for converting energy available in the environment, hence, low-frequency vibration into usable electrical energy. As there are methods reported for energy conversion, either based on standard or non-linear approaches, this work employs both methods to comparatively characterize the energy conversion capability obtained from two ferroelectric ceramics, i.e PMN-PT and PZT-Mn. The method eligible for PVDF is described. An obtained electrical output and suggested applications are also discussed.

1.2 Thesis Outline

The thesis consists of six chapters. In the present chapter, the statement of the problem is addressed.

Chapter 2 presents the theoretical background on the piezoelectricity and a brief overview of electroactive PVDF polymers.

Chapter 3 reports the specific procedure and chemistry used for fabricating the PVDF-based materials in order to alter the material properties.

Chapter 4 describes the background on converting an ambient vibration into an electrical energy. The energy harvesting performance of two well-known piezoceramics is reported comparatively.

Chapter 5 overviews the use of PVDF materials in energy harvesting and, subsequently, their realization as a vibrational harvester is described theoretically and experimentally.

Chapter 6 summaries the conclusions stated in various chapters of the present work and the prognosis for future investigation is then given.

1.3 Objectives of Research

The objectives of this work are the following:

1. Fabrication and characterization of the PVDF-based materials with properties tailoring from piezopolymers to piezoceramics,

2. Study of energy harvesting using standard and nonlinear techniques on piezoceramics,

3. Investigation on the use of PVDF for converting low-frequency vibration to electrical output.

CHAPTER 2

THEORETICAL BACKGROUD

In this chapter, a theoretical background in piezoelectricity is presented. This includes general overview for electroactive polynyledene fluoride or PVDF polymers, polymer composites and porous polymer. Fabrication methods and techniques for material characterizations are also presented. Background on energy harvesting and its use in piezoceramics and PVDF are separately presented in Chapters 4 and 5, respectively.

2.1 Piezoelectricity and Related Properties

Piezoelectricity by definition is an electric charge generated in a material when it is applied a mechanical pressure. This is a direct effect. The opposite phenomena, i.e. converse or inverse piezoelectric is where a change in shape of a material is occurred when it is applied an electric field. These two effects for various cases are schematically depicted in Figure 2.1. Figures 2.1(a) and 2.1(b) respectively describe the direct effect for open and short circuit conditions in which a piezoelectric material acts as a sensor. Contrarily, in the inverse effect a piezoelectric element becomes an actuator. If the distortion of the material is prevented as shown in Figure 2.1(c), an elastic tension T occurs. A force F is thereby applied to the device. The converse effect can be observed in both static and oscillation conditions. Structures using piezoelectric materials as both sensors and actuators are referred to as "smart or intelligent structures" because of their ability to "sense" and "repair" their condition through control algorithms.

The piezoelectric effect has long been discovered in 1880 by the Curie Brothers, Jacques and Pierre in natural substances such as Rochelle salt, quartz etc. The first synthesized piezoelectric material was barium titanate, $BaTiO_3$ and the best piezoelectric element developed to date, lead titanate zirconate (PZT), was discovered during the following years (Jaffe and Roth, 1954). PZT piezoceramics offer great improvements in piezoelectric characteristics and physical properties and most used in
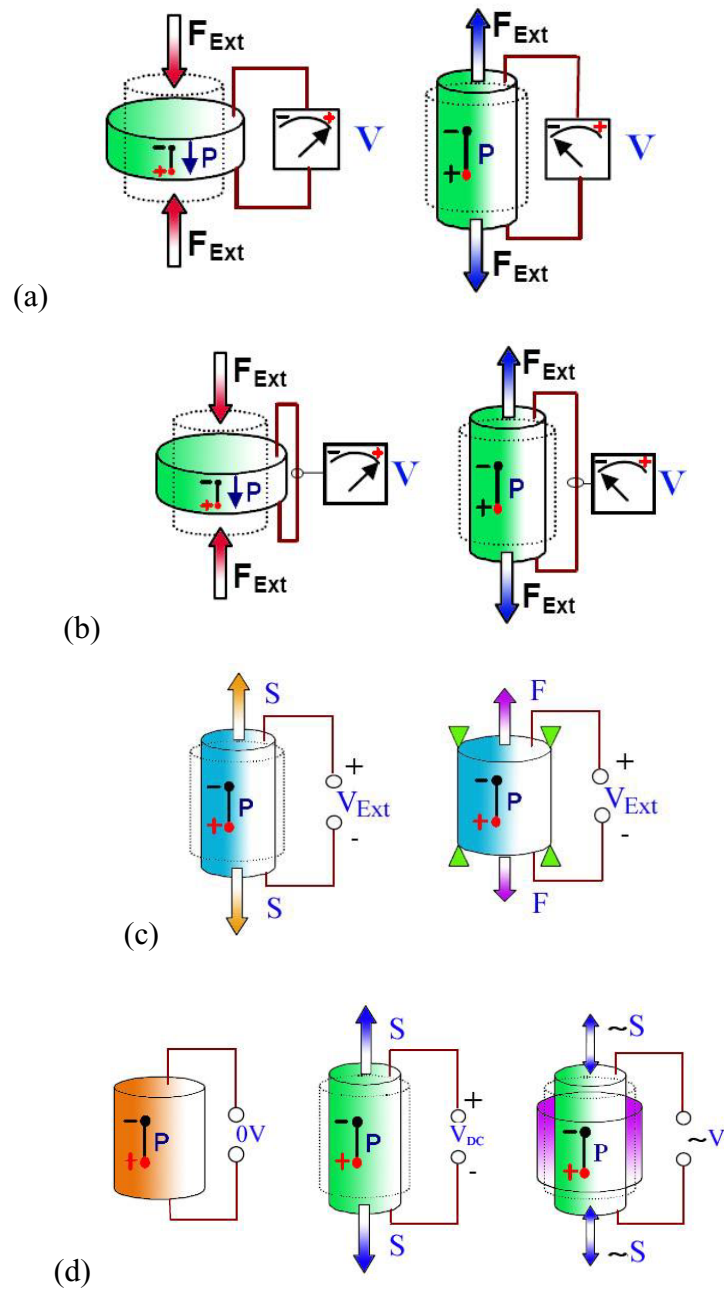
Figure 2.1 Schematic diagrams of the piezoelectric effect of various cases. Direct effect with a material in (a) open circuit and (b) short circuit conditions. Converse effect for a material (c) with free displacement S and with blocking force F and (d) at start, in static and dynamic operations, respectively.

plenty of applications of various types of transducers, sensors, actuators, power generators, piezoelectric motors etc.

The constitutive equations for piezoelectric materials describing the effects with respect to electrical and mechanical properties are presented in the following equations.

$$S = dE \tag{2.1}$$

$$E = \beta^S D - hS \tag{2.2}$$

$$D = \varepsilon^T E + dT \tag{2.3}$$

$$S = s^E T + d^t E \tag{2.4}$$

Where T, E, S, and D are the vectors of stress, electric field, strain, and electric displacement (charge per unit area), respectively. h and d are the piezoelectric coefficients, ^{S} is the dielectric impermeability at constant strain, s^E is the elastic compliance at constant electric field, ^{T} is the dielectric constant measured at constant stress, respectively. The superscript t denotes the transpose of a matrix.

In circuitry, the electric charge flows from one electroded surface to another across the piezoelectric material and there is the electric signal corresponding to the mechanical stimulus. The signal is varied with either stress applied to the electrode or the mechanical strain that the material experiences. Among the piezoelectric parameters, piezoelectric voltage coefficient (g) and piezoelectric strain coeffiicent (d) are of interest for regarding the piezoelectric material as energy harvester. They can be defined by the following partial differential equations (Taylor *et al*., 1985; Ikeda, 1990; Wang *et al*.,1988).

$$d = \left(\frac{\partial D}{\partial T}\right)_{E=0} \tag{2.5}$$

$$g = \left(\frac{\partial E}{\partial T}\right)_{D=0} \tag{2.6}$$

$$e = \left(\frac{\partial D}{\partial S}\right)_{E=0} \tag{2.7}$$

$$h = \left(\frac{\partial E}{\partial S}\right)_{D=0} \tag{2.8}$$

Where e is also the piezoelectric coefficient, open circuit (D=0) is labeled in [E] while short circuit (E=0) in [D], the electric field is in a unit of [V/m] while the electric displacement in [m].

Electromechanical coupling coefficient, k^2 is also an important parameter in energy harvesting. It is defined as either the ratio of stored mechanical energy to input electrical energy or the ratio of stored electrical energy to input mechanical energy. When an electrical field E is applied to piezoelectric material, k^2 can be calculated as (Ikeda, 1990).

$$k^2 = \frac{d^2}{\varepsilon_r s} \tag{2.9}$$

Hence, the piezoelectric strain constant, d is defined as

$$d = \frac{\text{strain developed}}{\text{applied field}} \left(\frac{m}{V}\right) \tag{2.10}$$

In practice, the effective electromechanical coupling (k_{eff}^2) is often used. It can be determined from the resonance (f_r) and anti-resonance (f_a) frequencies of the piezoelectric material oscillating in an alternating electric field (Mason and Jaffee, 1954),

$$k_{eff}^2 = \frac{f_a^2 - f_r^2}{f_r^2} \tag{2.11}$$

$_r$, which was mentioned in equation (2.9), is a relative permittivity or dielectric constant, relating the permittivity of vacuum (8.854×10^{-12} F·m^{-1}) or ε_0 to the material permittivity, as below,

$$\varepsilon_r\varepsilon_0 = \frac{d}{g} = \frac{e}{gh} \tag{2.12}$$

The dielectric constant is related to the electric displacement and polarization by

$$P = \varepsilon_0 \; E \qquad or \qquad D = \varepsilon_0\varepsilon_r E = \varepsilon E \tag{2.13}$$

Where   is the electric susceptibility.

The dielectric constant can express as the complex dielectric permittivity (Sadiku, 1995) given by

$$\varepsilon = \varepsilon_0\varepsilon_r = \varepsilon' - j\varepsilon'' \qquad or \qquad \varepsilon_r = \frac{\varepsilon'}{\varepsilon_0} - j\frac{\varepsilon''}{\varepsilon_0} = \varepsilon_r' - j\varepsilon_r'' \tag{2.14}$$

ε_r', is the real part of complex relative permittivity, referring to the amount of energy (applied from an external field) stored in the material. Meanwhile, the energy loss from the material to an external field is referred to ε_r'' which is the imaginary part and known as the loss factor. The loss factor includes the effect of both dielectric loss tangent (tan) and conductivity ( ) given as

$$\tan\delta = \frac{\varepsilon''}{\varepsilon'} = \frac{\varepsilon_r''}{\varepsilon_r'} = \frac{\sigma}{\omega\varepsilon'} \tag{2.15}$$

Where   is the angular frequency.

Concerning the dielectric properties, ferroelectric materials are actually dielectric, i.e. an electrical insulator that can be polarized by the action of an applied electric field. Dielectrics are broadly divided into two groups: polar and non-polar. A dielectric having finite and permanent polarization even in the absence of electric field is polar and those having no permanent polarization is non-polar. Ferroelectrics are named only in the case that the spontaneous polarization can be reversed by the application of an electric field. All ferroelectric crystals are pyroelectric (the development of an electrical charge on the surface of a crystal when its temperature is changed) and all pyroelectric crystals are piezoelectric. Piezoelectric materials, hence, come to play important role. For polycrystalline ferroelectric materials, the

introduction of the polarity into the material is necessary and can be done by means of applying a DC electric field to switch the constituent polarizations to align to the polar axes (which is commonly assigned the direction of the field). This process is called poling. The most commercially poled materials such as $BaTiO_3$ and $PbTiO_3$ are the titania-compound based with perovskite crystal structure whose molecular formula is ABO_3 (i.e., a large cation (A) on the corners, a smaller cation (B) in the body center, and oxygen (O) in the centers). Thses materials go through a phase transition from a centrosymmetric non-polar lattice, to a non-centrosymmetry polar lattice at the so-called Curie temperature. This is accompanied by the transition of paraelectric into ferroelectric phase.

2.2 Overview of Electroactive PVDF Polymer

Apart from the ferroelectric oxides whose ions or atoms are repeated in the three-dimensional lattice over large volumes, there are ferroelectric polymers whose macromolecules arranged in a lower symmetry and frequently mixed with amorphous and crystalline regions. The strong piezoelectricity of PVDF, was observed by Kawai and coworker in 1969, and the ferroelectricity in the PVDF was found two years later. The piezoelectric coefficient of poled PVDF is as high as 20 $pC \cdot N^{-1}$ (Davis, 1987).

The PVDF including its copolymer have been reported their numerous applications in, e.g. actuators, vibration control, medical ultrasound and sensors while their utilization in electronics and energy conversion are significantly rare (Lang and Muensit, 2006; Lee and Sung, 1999; Gentry *et al*., 1997; Gerald *et al*., 2000; Guyomar *et al*., 2009). Among the electroactive polymers the PVDF is semi-crystalline and has superior mechanical characteristic but vastly inferior conductivity to those which are fully amorphous. A semi-crystalline polyvinylidene fluoride or PVDF was polymerized for the first time in the 1940s. It has a simple chemical structure $(-CH_2-CF_2-,)_n$, lied between polyethylene (PE) $-(CH_2-CH_2)_n-$ and polytetrafluoroethylene (PTFE) $-(CF_2-CF_2)_n-$. Fluorocarbons are highly appropriate monomers for ferroelectric polymer crystals. The fluorine atom has a Van der Waals radius of 1.35 Å similar to that of hydrogen (1.2 Å). They form highly polar bonds

with carbon, having a dipole moment of 6.4×10^{-30} Cm·monomer^{-1} (Tashiro, 1995). This simplicity in chemical structure gives flexibility which comes from PE side and sterochemical constraint from PTFE to the main-chain structure of PVDF. Due to the strong electronegativity of fluorine, there are two dipole moments for each repeat unit; one for -CH_2- denoted as "head" and one for -CF_2- denoted as "tail" which is usually produced under high temperature (50 to 150°C) and high pressure (10 to 300 atm). Polymer crystallinity is one of the most important parameter affecting the piezoelectric properties of PVDF. Hence, the crystallinity in polymers means that the chains are packed together more efficiently and tightly which increases the density of the polymer, as well as leads to an increase in the mechanical properties of the polymers. Commercial PVDF normally has a crystalline fraction of about 50 to 60% depending on the amount of chain ordering defects (Vinson and Jungnickel, 1998).To improve crystallinity and produce macroscopic polarization, it is necessary to prepare electrically inactive polymorphous samples by using a mechanical stretching and/or poling process. For example, mechanical stretching to about 300% of its original length at a temperature around 100°C and then applying a high electric field (Tim *et al.*, 2005). By these means, the reorientation process involves intermediate steps and is not a simple 180 rotation (Kepler, 1978). Polarization reversal may progress through successive 60 rotations (Figure 2.2) which is consistent with the experimental observations and theoretical investigation at the molecular level (Bur *et al.,*1986; Naegele and Yoon, 1978; Dvey-Aharon *et al.*, 1980). After stretching, the designation is as follows: '1' is the stretching direction and '3' is the net dipole direction (Figure 2.3). If the film is biaxial stretching, the stretching direction at '2' axis will occurred. Unlike biaxial stretching, '2' direction of uniaxial orientation is normal to the machine direction and dipole direction. A net dipole only exists in the direction 3, 1 and 2 have no charge due to the uniaxial deformation. The important points are the polarization decrease depending on the film thickness as tensile stress is considered positive and the positive charge observed in direction 3 due to the positive deformation in 1 or 2 directions which also decrease in film thickness. Moreover, shear stress 4 and 5 lead to rotation on the axis 1 and 2, respectively. Therefore, they give some values, however, all j=6 components are zero because of the unstressed on the 3 axis (Riande and Díaz-Calleja, 2004).
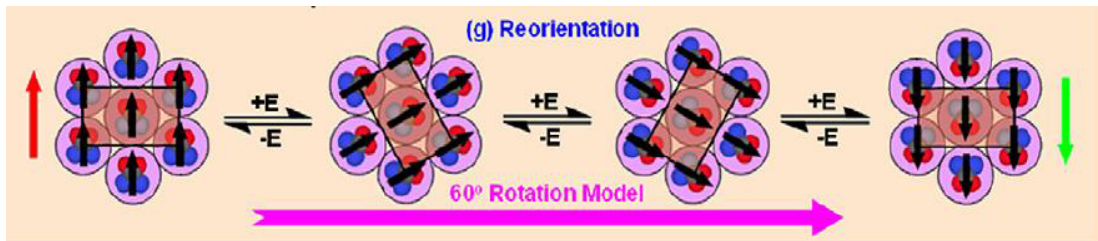
Figure 2.2 Schematic diagram of polarization reorientation (Lovinger, 1983).
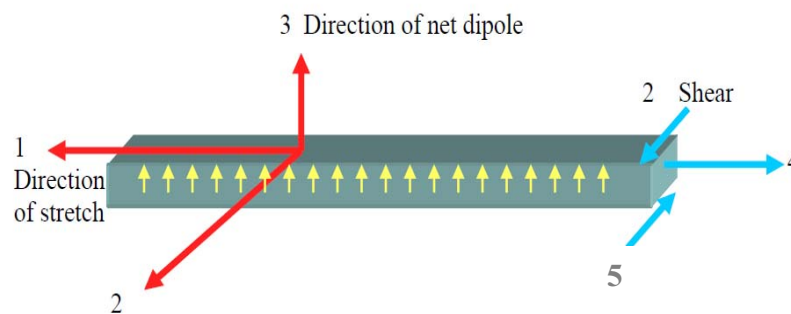
Figure 2.3 Schematic diagram of stretched direction and net dipole moment in polymer specimen (JEE, 2005).

Common phases of PVDF are α-, β-, γ- and δ-phases. The two most common phases are the helical -phase with a transgauche (TGTG) molecular conformation resulting in an antipolar unit cell, and the -phase with an all-trans (TT) conformation resulting in a polar unit cell whose dipole moments (μ) aligned perpendicular to the chain axis (Lovinger, 1983). The β-phase shows the highest piezoelectric effect of the four crystal phases, but in actual PVDF sample there are likely many crystal phases coexisting. The dipole moment of β-PVDF is aligned in the same direction leading to the highest dipole moment (7.0 10^{-30} Cm·monomer^{-1}) (Zhu *et al*., 2008). Unlike β-PVDF, the dipole moment of α crystallites is oriented in opposite directions (Figure 2.4) resulting in a zero net polarization. Polyvinylidene fluoride has a polar bond which is a C-F bond. The bond length and the angle between the bonds of C-C are 153 pm and 112°, respectively. Generally, the conformation of C-C chain as planar zigzag is not commonly observed in other polymers. So, the carbon backbone cannot occur if hydrogen atoms are replaced by atoms with diameters exceeding 254 pm.
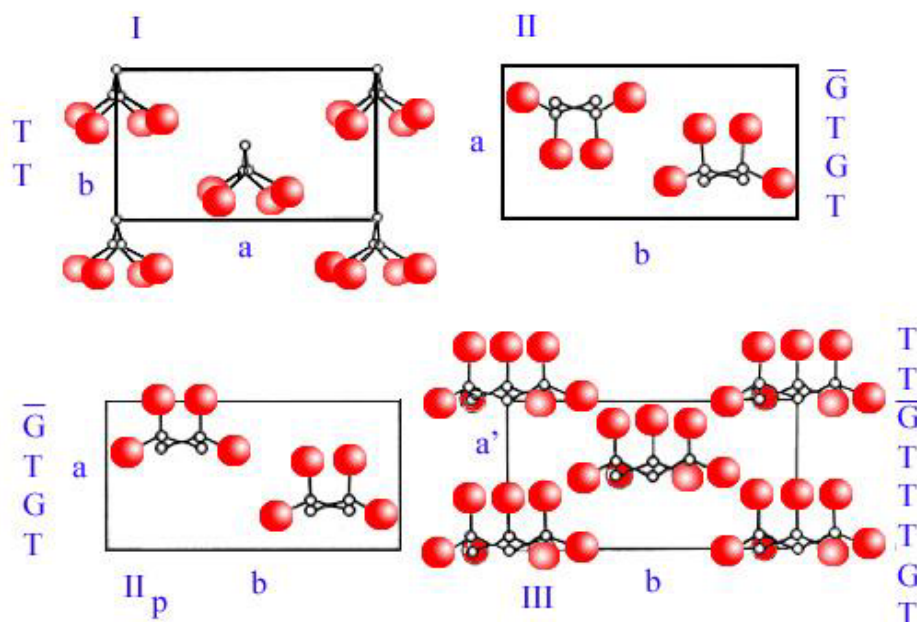
Figure 2.4 Unit cells of PVDF phase when projected on a plan perpendicular to the c axis; (I) -phase, (II) -phase, (II_p) -phase and (III) -phase. White and red spheres represent carbon and fluorine atoms, respectively. (Redrawing from Nalwa, 1995).

The other polymorphic phase, δ-phase can be obtained by applying strong electric field (>130 MV·m^{-1}). Every second chain will rotate around the molecular chain axis resulting in a parallel orientation of all dipoles in the crystallites even if the chain conformation and the unit cell are still the same. The last one, γ-phase can occur from molten sample by the crystallization at high temperature or pressure. These phases have interrelations and can be formed through a specific procedure and preparation conditions. This was depicted in Figure 2.5, an annealing at high temperature or very high pressure, or by drawing at low temperature, and ultra-drawing at high temperature may obtain β-phase from γ-phase. The β-phase might occur by applying high pressure to a gel sample before the temperature is reduced to room temperature, and applying high temperature also produced β-phase directly from a molten state

Similar to polycrystalline piezoceramics, to induce polarization in polymer, the voltage potential is applied to produce the electric field across the sample. In the case of poor contact, the poling can be done without discharges, dielectric breakdown, or in homogeneities in the poling field if the sample is placed in a vacuum or submerged in an insulating fluid such as silicone oil, or alternatively at high electric and thermal field (Figure 2.6). Both constant and varying electric fields can be applied to the sample during electrode poling, however, the constant electric field is held on the sample from 10-30 minutes up to 2 hours at elevated temperature to ensure the dipole moment is reoriented. Even if the poling can be done at room temperature, an elevated temperature improves dipole mobility and consequently increases the material polarizability (Kumart and Perlman, 1993).
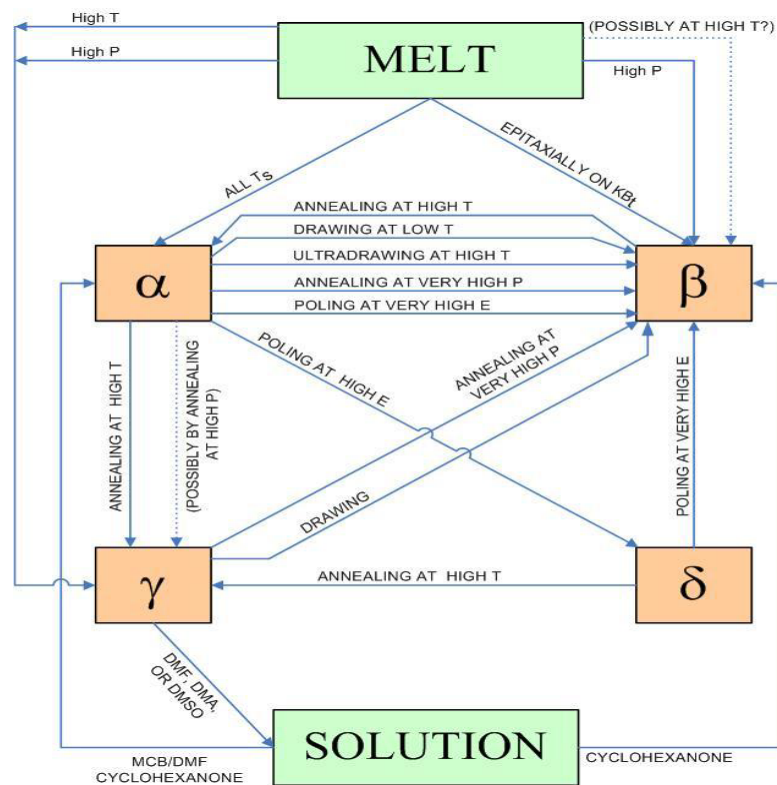
Figure 2.5 Interrelations among the phases of PVDF.
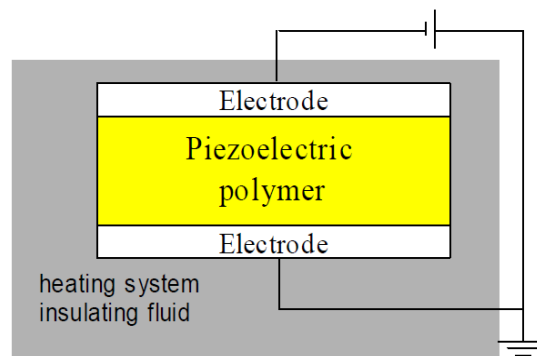
Figure 2.6   Schematic of the electrode poling system (Tim *et al*., 2005).

The crystal of PVDF polymer is extremely small and formed to spherically symmetric poly-crystalline aggregates with zero net polarization when it grows from the melt. These aggregates are called spherulites (Figure 2.7) resulting from the nucleation of primary crystals within the melt, followed by radial growth outward from these nuclei in spherical envelopes (Keith and Padden, 1964).
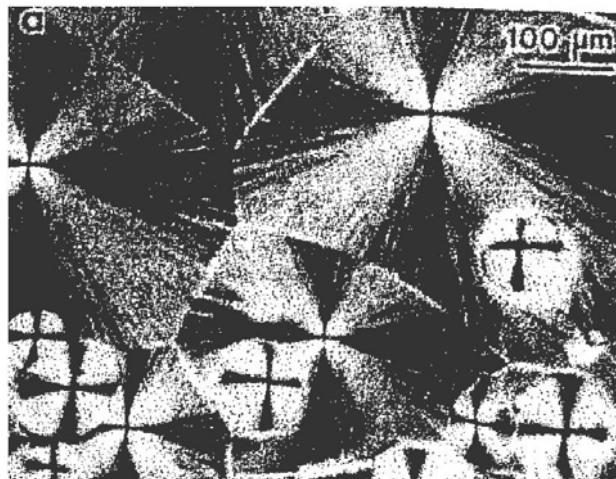
Figure 2.7 Spherulites of PVDF crystallized from crystallized from the melt
at 1600 ํ C. Large spherulites are of the antipolar α-phase; small ones
belong to the polar γ-phase (Lovinger, 1981).

The microstructure of spherulites, is stacks of very thin, platelet-like crystals, called lamellae (about 10 nm thick and several micrometers in lateral dimensions), and usually appears as radial fibers (Figure 2.8). These lamellae consists of macromolecular segments packed as crystallo-graphically about 50% of the total mass; while the other half is the intervening amorphous regions contain chain segments in disordered conformations. This two-phase structure of the solid state is typical of semicrystallizable polymers. (Lovinger, 1981).
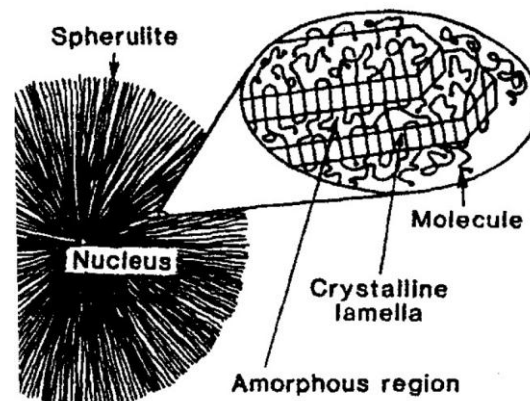
Figure 2.8 Schematic representation of the structure of polymer spherulites (Lovinger, 1981).

2.3 Polymer Composites

An alternative approach to alter the properties of the polymers is the incorporation of the fillers, for example, electrical conducting phases to form the polymer composites (Tawansi *et al*., 1998; Serguei *et al*., 2009; Li *et al*., 2006; Abdelaziz, 2004; Kima *et al*., 2006; Moisala *et al.,* 2006; Wu *et al*., 2006; Maaroufi *et al*., 2004; Dang *et al*., 2004). Properties of polymer composites depend upon on the size, shape, agglomeration and distribution of the filler and its adhesion to the polymer matrix. Sample can be casted from solutions of crystalline or noncrystalline polymers where the sample thickness is controlled by the solution concentration. Cast exhibit a

range of morphologies due to the effect of solvents, substrates and orientation. The following sub-topic, therefore, presents several ways in forming the composites.

2.3.1 Patterns of Composite Connectivity

Composite materials which are made by a combination of a ferroelectric polymer and a filler of suitable properties means not only choosing the right materials processed in a particular way, but also coupling them with the best possible design structure. The mechanical, electrical and thermal properties of multiphase material depend on the interspatial relationships between the phases. Polymers composite composes of two phases, a polymer is called the matrix, which is continuous and surrounds the other phase, which is usually called the dispersed, discrete or passive phase. The properties of composite depend on several parameters such as connectivity of the phases, volume fraction of dispersed phase, and the distribution of the active phase in the composite. The density, dielectric, electrical and piezoelectric properties of composite are strongly dependent on the arrangement of the component phase.

Each phase may be self-connected in either one, two or three dimensions. For diphasic or binary phase system, combinations of phase connectivity which are denoted the connectivity of the filler and that of the matrix can be divided into ten different forms; as 0-0, 0-1, 0-2, 0-3, 1-1, 1-2, 1-3, 2-2, 2-3, and 3-3. Commonly, the dispersion of particles embedded in a matrix indicated as a 0-3 composite, whereas another system which is composed of fibers implanted on a matrix and oriented across, one of the dimensions of the sample is known as a 1-3 composite. The definition in a binary system, of what is the filler and what is the matrix can be confusing as the volume fraction of filler is greater than that of the matrix. Therefore, the connectivity criteria in this case can remark the phase of the highest connectivity in the composite or active part as the matrix. The most commonly studied composites are the 0-3 because the 0-3 connectivity owes its popularity to the easy fabrication procedure which allows for mass production at a relatively low cost (Dias and Das-Gupta, 1996).

2.3.2 Percolation Threshold, Conductive Fillers and Nanoparticles

As the material performance depends on the material morphology, the control of filler morphology becomes a very importance aspect. The development of synthesis scheme in order to control particle size, shape and composition independently from one another is considered. Firstly, the percolation threshold is to be discussed. Percolation theory refers to a class of models that describe the properties of a system given the networking among its component. For conductor-insulator system, the conducting filler has been added in polymer-based composites. An abrupt change in electrical conductivity can be identified in the composite when the filler content reaches a critical volume fraction. Percolation theory predicted that the following universal power law dictates the transportation of conductor-to-insulator related physical properties:

$$\frac{K}{K_f} = \left(\frac{\emptyset - \emptyset_c}{1 - \emptyset_c}\right)^t \qquad \text{When } K_f \gg K_m \qquad (2.16)$$

Where K, K_f, and K_m are the quantities characterizing the physical property of the composite, the filler, and the matrix respectively. The $\emptyset$ and $\emptyset_c$ are the filler volume fraction and the percolation threshold (critical volume fraction), respectively. The critical exponent t is predicted to be a constant in the range of 1.6-2, depending on the eccentricity for spheroid fillers. According to equation 2.16, a slight variation in the volume fraction will lead to large change in the conductivity. To achieve higher piezoresistive coefficient, the particle filler content should be close to the percolation threshold 30% (Lin *et al.*, 2010). The heavy loading will generally lead to both the structural deterioration due to the large amount of interfaces and alteration of the physical properties, such as, the elastic modulus, ductility, and transparency. Therefore, for applications in tissue engineering or tactile sensors for robots, conducting fiber fillers with high aspect ratio (AR) are more desirable for the low percolation threshold 1%.

According to the equation presented by Dias and Das-Gupta (2001), it can be used to prepare the quantities required for mixing of the dopant (i.e. ceramic, metal) and polymers.

$$M^d = M^p \times \frac{\rho^d}{\rho^p} \times \frac{\emptyset}{1-\emptyset} \qquad (2.17)$$

Where M, and are the mass, density and volume fraction respectively, and the subscripts p and d refer to the polymer and dopant, respectively. Density and total volume (V) of composite determine by (2.18) and (2.19).

$$\rho = \emptyset \rho^d + (1+\emptyset)\rho^p \qquad (2.18)$$

$$V = \frac{M^d}{\emptyset \rho^c} \qquad (2.19)$$

If particles have ideal spherical with a mono-dispersed size distribution, the specific surface area can be related to the particle size as showed in equation 2.20

$$S = \frac{6}{\rho l} \qquad (2.20)$$

Where l is the spherical diameter.

Doping is a widely used means to tailor the electrical conductivity, thermal conductivity, piezoelectric properties, and so on. Doping can be accomplished by several methods. The doping is usually quantitative and the carrier concentration is directly proportional to the dopant concentration. Dopant of polymers involves random dispersion or aggregation of structures of composite. Polymer doping leads to the formation of conjugational defects in the polymer matrix.

Polymer composites filled with conductive particles appear to be the most attractive due to an essential role in various industrial applications. The approach to obtain the metal-polymer composite can be divided in two strategies which are known as in-situ and ex-situ approach. The first is to generate the metallic inside a polymer matrix. The latter is to produce the metal particles and then dispersing them into polymer matrix (Nicolais and Carotenuto, 2005) which is one of the most general

methods because there are no limitations on the kinds of nanoparticles and polymers that can be used. The presence of a shell increases the compatibility of the particles in the polymer matrix and makes it easier to disperse them. However, in-situ approaches are currently getting a great deal of attention because of their obvious technological advantages over ex situ methods.

In the case of nanometal-embedded polymer, the definition of nanoparticles differs depending upon the materials, fields and applications concerned. In the narrower sense, they are regarded as the particles smaller than 10-20 nm, where the physical properties of solid materials themselves would drastically change. The particles range of nanometer from 1 nm to 1 μm could be called as nanoparticles. The specific surface area increases generally in reversal proportion to the particle size. For example, if the particle of 1 cm is micronized to 1 μm and 10 nm, the specific area becomes ten thoundsand times and million times, respectively. As the increase in the specific surface area directly influences such properties like the solution and reaction rates of the particles. It is one of major reasons for the unique properties of the nanoparticles different from the bulk material together with the change in the surface properties of the particle itself. The solid particle tends to show different properties from the bulk material and even the physical properties like melting point and dielectric constant themselves which have been specific properties may change, when the particles become in nanometer size. The change in fundamental properties with particle size is called size effect. Nanoparticles have a large specific surface area and hence their properties are dominated by surfaces rather than bulk. The specific surface area is often used as a basic unit for the particle properties of nanoparticles (Hosokawa *et al*., 2007).

Nanoparticles, usually existing as aggregates, are dispersed in a liquid or solid medium. Their high surface energy makes inorganic nanoparticles generally extremely unstable and self-aggregate. The limitation of dispersion of nanoparticles is reaggregation of the individual nanoparticles and the establishment of an equilibrium state under definite conditions, which determines the size distribution of the agglomerate of dispersed nanoparticles. Particles coated by a polymer shell are considerably more stable against aggregation because of a large decrease of their surface energy in comparison with bare particles.

2.3.3 *Porous Polymer and Surfactants*

In order to improve the piezoelectric response in the polymer, the porous polymer composite are more significantly efficient than the dense structure because of the air inside the polymer matrix can be introduced to act as one of the constituent material resulting in an increase of piezoelectric coefficient (d_{33}) as high as 1,000 pC·N^{-1} (Carpi and Smela, 2009).

There are three main types of colloidal forces: Van der Waals interactions, electrical double-layer interactions, and steric interactions. Hydrophobic and solvation forces are also important. The basis of such methods used for production of porous polymer and inorganic nanoparticles is templating procedure. This procedure is used to fabricate organic and inorganic structures, regulating their final form and hence their properties. Incorporation of surfactant and colloidal solution is one of the most used techniques which enable their use for elaborating uniform sample. Due to the fact that they can reduce the surface tension of aqueous solutions, thus, they have been used in order to achieve the high suspension efficiency for colloidal particles. However, significant challenges remain in the fabrication and production of high-performance low-dielectric materials consisting of closed nanopores of 5 nm or less that meet the requirements of the production of advanced ICs in the microelectronics industry. The well-controlled nanopores imprinted in spin-on polymeric dielectric thin films play an important role in lowering the dielectric constant (low-k) of electric materials. Closed nanopores are prone to prevent metals (e.g., copper) from diffusion into the interdielectric layers during the fabrication process of integrated circuits (ICs).

The solid surface is also influenced to the material performance. To better understand the properties of a solid surface, it is necessary to consider the possible structures of solids and their exposed surfaces. Solids and solid surfaces may be roughly divided into two main categories, based on the nature of the arrangement of the constituent units. A solid may be crystalline, having reproducible intrinsic bulk properties such as a sharp melting point and a uniform pattern of packing of its constituent units (atom, ions, or molecules) into a lattice structure, or it may be amorphous. A third class of solid is a heterogeneous mix of crystalline and amorphous

structures. In the case of metal-polymer composite, the dispersion of solid particles in liquid is immensely important. The ability of preparing suspension of the proper particle size, and to maintain the stability of such dispersions for extended periods of time, quit often involves the use of surfactant (Myers, 2006).

Surfactants are the agent for lowering the surface tension of liquid and composts of compound molecules of the opposing character of the hydrophilic (head group) and hydrophobic (tail) (Liang *et al*., 2007). The surfactant makes the better spreading of two components and often used for stabilization of dispersions of nanoparticles. Surfactants can be classified into four types; (1) anionic surfactant, (2) cationic surfactant, (3) nonionic surfactant and (4) amphoteric surfactant. Firstly, anionic surfactant is the surfactant that charge of hydrophilic side is negative. Most of them are carboxylate, sulfate, sulphonate or phosphate group. This surfactant is used in detergent industrial. Anionic surfactant is 49% to total surfactants. Secondly, cationic surfactant is the surfactant that charge of hydrophilic side is positive. Most of them are quaternary ammonium. This surfactant cannot work at high base solution because of the ammonium salt will be oxidized and precipitated. Next, nonionic surfactant is the surfactant that hydrophilic side does not have charge. Polyether or polyhydroxyl are groups that are similarly like ion. Finally, amphoteric (Zwitterionic) is the surfactant that charges of hydrophilic side are either positive or negative. If environment have pH > 7, charge of hydrophilic side will be negative. In the other hand, if environment have pH < 7, charge of hydrophilic side will be positive. In the neutral environment (pH=7), there are no charges on hydrophilic side.

$CH_3(CH_2)_j CH(CH_2)_k CH_3$

(j+k =6-9)

Sodium linear alkylbenzenesulfonate (LAS)

Sodium alkyl sulfate (AS)

$Na^{+-}O_3 S-CH-CO-O-R_1$
$H_2 C-CO-O-R_2$

Sodium sulfosuccinates

$R-OPO_3{}^{2+}2Na^-$

Sodium alkyl phosphate
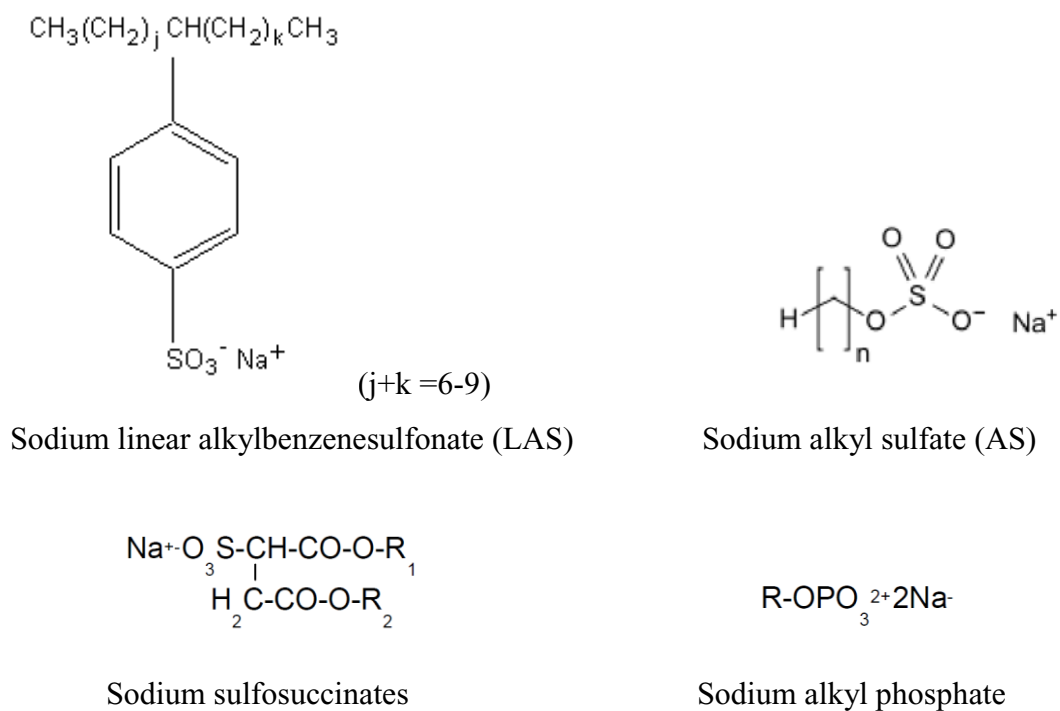
Figure 2.9 Anionic surfactant.

Etherquat (EQ)

DEEDMAC

Diesterquat (DEQ)

Alkyl ester ammonium salt
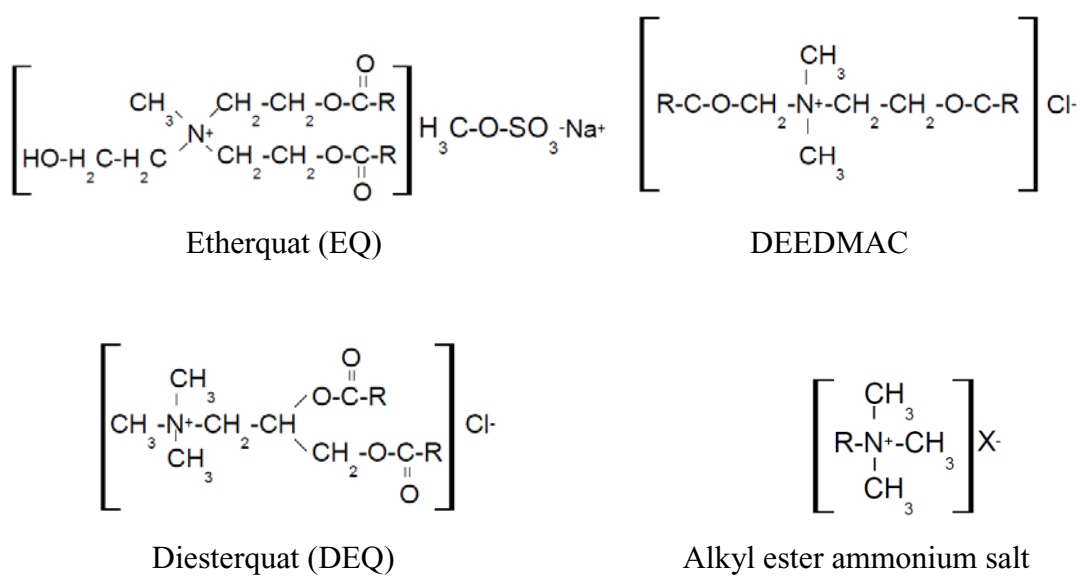
Figure 2.10 Cationic surfactant.

$$H\text{-}(CH_2)_{12}\text{-}O\text{-}(CH_2\text{-}CH_2\text{-}O)_7\text{-}H \qquad\qquad (CH_3\text{-}(CH_2)_{12}\text{-}O\text{-})_{10}\text{-}(CH_2)_4\text{-}OH$$

Alcohol ethoxylates (AE)   Alcohol alkoxylates (AA)

Figure 2.11 Nonionic surfactant.

Alkyl butaine   Alkylamidopropyl betaine
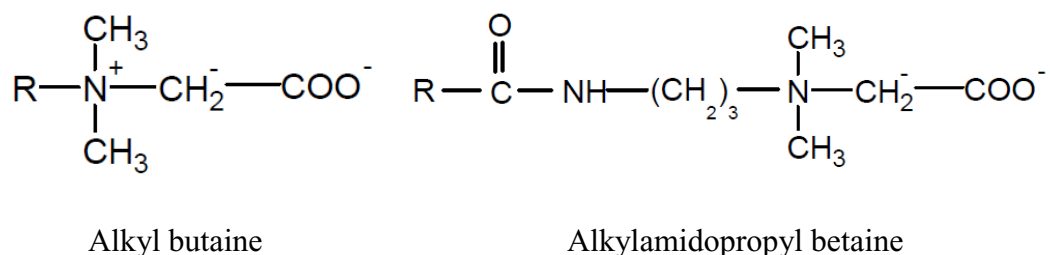
Figure 2.12 Amphoteric surfactant.

Brij-30 or 'Tetraethylene glycol dodecyl ether is a nonionic surfactant. Chemical structure is shown in figure 3.5
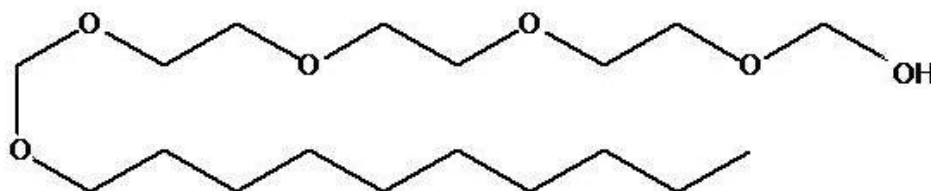
Figure 2.13 Brij-30 (Tetraethylene glycol dodecyl ether) (depicted by this work).

2.4 Preparation Procedure for Fabricating Electroactive Polymer

Nowadays, the electroactive polymer is of great concern due to the rapid increase in its demand and the cost of energy consumption and it is friendly to the environment. One of the most important attributes to the properties of such electroactive polymer as PVDF is the manufacturing approach. Several simple approaches for thick films to more and more sophisticated techniques for thin films such as tape casting, thermal spraying, spin coating, and Langmuir-Blodgett, have been used to evaluate polymer film.

The first, thermal spraying technique, is an effective and low cost coating processes, the melted or heated materials is sprayed on the surface to apply thick coating to change surface properties of the component. The coating precursor is heated by electrical arc discharge (plasma or arc) or chemical means (combustion flame). Coating materials usually are metals, alloys, ceramics, plastics and composites which are heated to a molten state and accelerated towards substrates over a large area in the form of micrometer-size particles. Generally, the coating quality increases with increasing particle velocity resulting coatings are made by the accumulation of numerous sprayed particles. Plasma spraying has the advantage that it can spray very high melting point materials such as refractory metals like tungsten and ceramics like zirconia unlike combustion processes. Plasma gas, usually are argon, nitrogen, hydrogen, helium, flows through the plasma spray gun which are comprised of cathode and anode both of which are water cooled which is shaped as a constricting nozzle. The plasma is initiated by a high voltage discharge which causes localized ionisation and a conductive path for a DC arc to form between cathode and anode. Plasma sprayed coatings are generally much denser, stronger and cleaner than the other thermal spray processes, thus, it probably accounts for the widest range of thermal spray coatings and applications and makes this process the most versatile. However, this process is relative high in cost and has complex process.

Spin coating is a procedure used for the application of thin films to flat substrates for several decades. A typical process involves depositing an excess amount of a solution onto the center of a substrate and then spinning the substrate at high speed (typically around 3000 rpm) in order to spread the fluid by centrifugal force (Figure 2.14). A machine used for spin coating is called a spin coater, or simply spinner. Rotation is continued while the fluid spins off the edges of the substrate, until the desired thickness of the film is achieved. The applied solvent is usually volatile, and simultaneously evaporates, thus, the final film thickness and other properties will depend on the nature of the solution (viscosity, drying rate, percent solids, surface tension, etc.) and the parameters chosen for the spin process. For instance, the thinner the film can occur at the higher the angular speed of spinning and the thickness of the film also depends on the concentration of the solution and the solvent. Spin coating is

widely used in microfabrication, where it can be used to create thin films with thicknesses below 10 nm.
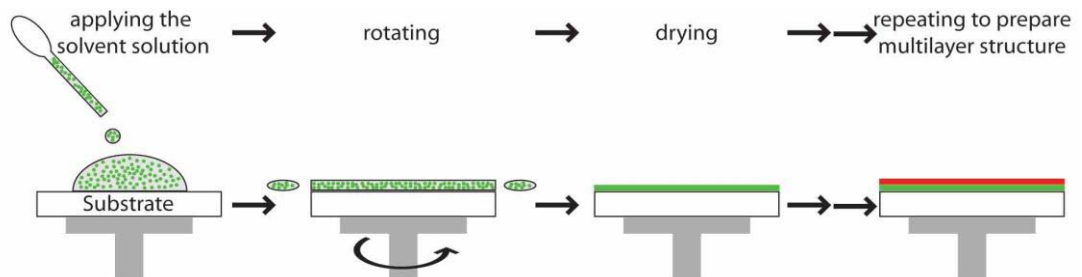
Figure 2.14 Mechanism of spin coating technique**.**

The Langmuir-Blodgett thin film deposition (Figure 2.15) used to create uniform layers of organic molecules from the surface of a liquid onto a solid by immersing (or emersing) the solid substrate into (or from) the liquid contains one or more monolayers of an organic material. In this technique a monolayer is adsorbed homogeneously with each immersion or emersion step resulting in the films with very accurate thickness can be formed because the thickness of each monolayer is known. The monolayers are assembled vertically and are usually composed of amphiphilic molecules with a hydrophilic head and a hydrophobic tail which enables a thin film to lay on a free surface of a subphase compound which is typically water. If the final product needs to be pure, the monolayers made with nanotubes embedded in a surfactant matrix suspended on top of an aqueous subphase and then pulling the substrate through the surface, such deposition methods are not useful. An alternative technique of creating single monolayer on surfaces is that of self-assembled monolayers.
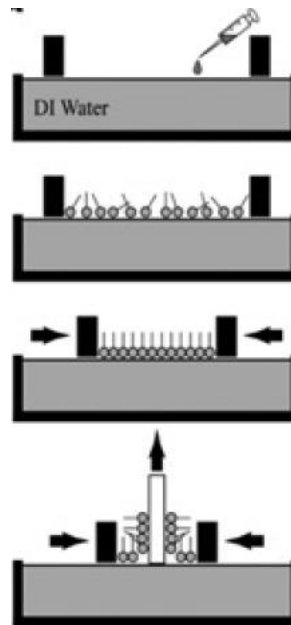
Figure 2.15 Mechanism of LB film deposition (Shin *et al*., 2008)

Among these techniques, "tape casting" is applied to this work due to its advantage over the other techniques. Tape casting technique (Figure 2.16) is a simple technique which polymer is dissolved in a solvent and the resulting mother liquor is usually poured into a mold, which contains a hollow cavity of the desired shape, and then allows solidifying, this is the so-called tape casting technique. The solidified part is the process of the releasing of solvent from the open mold form leaves the residue of the particle in polymer composite, in the form of a film. Casting is most often used for making metals or various materials that cure after mixing two or more components together to form complex shapes which would be complicated or unprofitable to make by other methods. The tape casting method has been attractive for preparing particle/polymer composites (Dasaesamoh, 2008; Hajeesaeh and Muensit, 2006) due to the lower temperatures involved and because of the perceived better mixing that is possible. To overcome the natural tendency for the metal particles to accumulate or associate, this is achieved by mixing metal powder into the same solvent used to dissolve the polymer this enhances their mixing. The solvent casting process necessarily results in thin films (fractions of a millimeter thickness),

because thick films bring about high dielectric loss owing to a highly porous or wrinkled film with bubble blisters in the result.
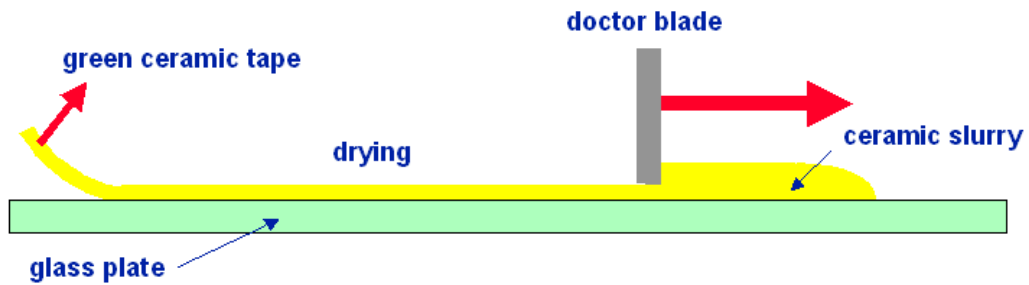
Figure 2.16 Schematic diagram of tape casting process.

2.5 Structure and Surface Analysis

Polymers are used in a wide range of applications due to their advantages over other types of materials, such as metals and ceramics, because of their low processing cost, light weight and properties. The study of structure and properties of materials aim for conceiving the relation between the manufacturing process, the structure produced and the resulting physical and chemical properties. This section aims to discuss the several techniques used to analyze the polymer structure and morphology, which must be clearly understood in order to develop the relations between the structure and properties of material.

2.5.1 X-ray Diffraction Method

In this non-destructive analytical, the crystallographic structure, chemical composition, and physical properties of materials and thin films can reveal. The single crystal diffractometer is used mainly to clarify the molecular structure of novel compounds, either natural products or synthetic molecules. Powder diffraction is mainly used for "finger print identification" of various solid materials. In powder or polycrystalline diffraction, it is important to have a sample with a smooth plane

surface. These techniques are based on observing the scattered intensity of an X-ray beam hitting a sample as a function of incident and scattered angle, polarization, and wavelength or energy.

The atoms are arranged in a random way similar to the disorder which is found in a liquid and is known as amorphous. On the other hand, the crystalline is the regular pattern of atom arrangement. Moreover, the crystal structure has a unit cell. The dimensions of the unit cell are described by three axes: a, b, c and the angles between them alpha, beta, and gamma. Only crystallites having reflecting planes (h, k, l) parallel to the specimen surface will contribute to the reflected intensities. If we have a truly random sample, each possible reflection from a given set of h, k, l planes will have an equal number of crystallites contributing to it. Typically, about 95% of solids can be described as crystalline.

The two parallel incident rays make an angle ( ) with these planes. A reflected beam of maximum intensity will result if two waves are in phase. The difference in each path length must then be an integral number of wavelengths, ( ) which express in Bragg's law.

$$n = 2d_{hkl} \sin\theta \qquad\qquad (2.21)$$

The process of reflection is described in terms of incident and reflected (or diffracted) rays, each making an angle   with a fixed crystal plane. Reflections occur from planes set at angle   with respect to the incident beam and generates a reflected beam at an angle 2   from the incident beam. The possible d-spacing defined by the indices h, k, l are determined by the shape of the unit cell.

2.5.2 *Fourier Transform Infrared (FT-IR) Method*

Spectroscopy refers to the absorption of light (visible radiation) by organic and inorganic compounds to generate an absorption spectrum. Infrared Radiation (IR) Analysis is a spectroscopy method, specific to IR chemical reactions. FT-IR stands for Fourier Transform Infrared, is a measurement technique whereby spectra are collected based on measurements of the coherence of a radiative source,

using time-domain or space-domain measurements of the electromagnetic radiation or other types of radiation. Typically, the continuous wave *Michelson* or *Fourier transform* spectrometer is the conventional method for measuring the temporal coherence of the light. The interferometer consists of a beam splitter, a fixed mirror, and a mirror that translates back and forth, very precisely. The beam splitter transmits half of the radiation striking it and reflects the other half. Radiation from the source strikes the beam splitter and separates into two beams. One beam is transmitted through the beam splitter to the fixed mirror and the second is reflected off the beam splitter to the moving mirror. The fixed and moving mirrors reflect the radiation back to the beam splitter. Again, half of this reflected radiation is transmitted and half is reflected at the beam splitter, resulting in one beam passing to the detector and the second back to the source.

The principle of FT-IR spectroscopy is to promote the excitation of molecular vibrations by submitting a sample to an infrared beam. The vibrational energy (usually expressed as wave numbers) is directly sensitive to the molecular composition: atoms involved in the bound, nature of the bound, surrounding atoms (hydrogen bounding), structure. The technique is extensively used to characterize both organic and mineral samples.

In infrared spectroscopy, IR radiation is passed through a sample. Some of the infrared radiation is absorbed by the sample and some of it is passed through (transmitted). The resulting spectrum represents the molecular absorption and transmission, creating a molecular fingerprint of the sample. Like a fingerprint no two unique molecular structures produce the same infrared spectrum. This makes infrared spectroscopy useful for several types of analysis. Furthermore, FTIR spectrometers are fast, easy to use and provide accurate results compared to other types of spectrometers.

Figure 2.17 Schematic diagram of Fourier Transform Infrared (FT-IR) method
(http://mmrc.caltech.edu/FTIR/FTIRintro.pdf).

2.5.3 Scanning Electron Microscope (SEM) Method

The Scanning Electron Microscope (SEM) is a microscope that uses a focused beam of high-energy electrons to generate a variety of signals at the surface of solid specimens to form an image. The signals that derive from electron-sample interactions do not reveal only external morphology (texture) but also the information about the sample including chemical composition, crystalline structure and orientation of materials making up the sample. The image is obtained using conventional SEM

techniques in a scanning mode (20X-30,00X magnification, spatial resolution of 50 to 100 nm). The SEM is also capable of performing analyses of selected point locations on the sample; this approach is especially useful in qualitatively or semi-quantitatively determining chemical compositions (using <u>EDS</u>), crystalline structure, and crystal orientations (using <u>EBSD</u>). Several advantages of using the SEM instead of a light microscope is because of its high resolution, which means that closely spaced features can be examined at a high magnification. In addition sample preparation is relatively easy because it only requires the sample to be conductive. The combination of higher magnification, larger depth of focus, greater resolution, and ease of sample observation makes the SEM one of the most heavily used instruments in research areas today.

Electron beam produced by using an electron gun is emitted from a conducting cathode material (i.e. tungsten filament). The energy required for a material to give up electrons is related to its work function. For Tungsten this energy is around 4.5 eV. The electron beam follows a vertical path through the microscope, which is held within a vacuum. The beam travels through electromagnetic fields and electromagnetic lenses, which focus the beam down toward the sample. When the incident electrons are decelerated in the solid sample, secondary electrons, backscattered electrons, diffracted backscattered electrons, photons (x-ray) are ejected from the sample. Secondary electrons are most valuable for showing morphology and topography on samples and backscattered electrons are most valuable for illustrating contrasts in composition in multiphase samples (i.e. for rapid phase discrimination). X-ray generation is produced by inelastic collisions of the incident electrons with electrons in discrete orbital (shell) of atoms in the sample. As the excited electrons return to lower energy states, they yield X-rays that are of a fixed wavelength (that is related to the difference in energy levels of electrons in different shells for a given element). Thus, characteristic X-rays are produced for each element in a mineral that is "excited" by the electron beam. SEM analysis is considered to be "non-destructive"; that is, x-rays generated by electron interactions do not lead to volume loss of the sample, so it is possible to analyze the same materials repeatedly. Detectors collect these X-rays, backscattered electrons, and secondary electrons and convert them into a

signal that is sent to a screen similar to a television screen. This produces the final image.
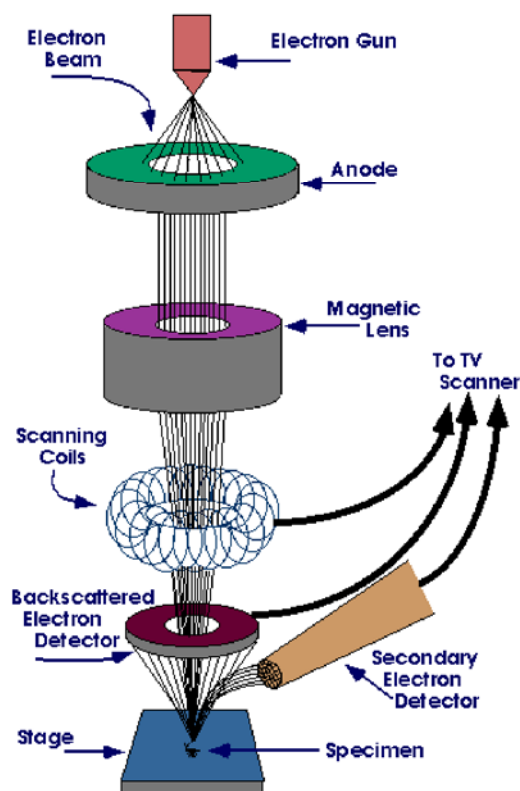
Figure 2.18 Illustration of SEM method

(http://bahadorimehr.blogspot.com/).

2.5.4 Differential Scanning Calorimetry (DSC) Method

Differential scanning calorimetry or DSC is a thermo-analytical technique in which the difference in energy inputs into a substance (and/or its reaction products) and a reference material is measured as a function of temperature whilst the substance and reference material are subjected to a controlled temperature program. Both the sample and reference are maintained at nearly the same temperature throughout the experiment. Generally, the temperature program for a DSC analysis is designed such that the sample holder temperature increases linearly as a function of time. The reference sample should have a well-defined heat capacity over the range of

temperatures to be scanned. In simplified terms, heat capacity is the amount of heat necessary to generate a specific temperature increase in a material.

$$\text{Heat capacity } (C_p) = \frac{\text{Heat flow}}{\text{Heat rate}} \qquad (2.22)$$

with
$$\text{Heat flow} = \frac{\text{Heat}}{\text{time}} = \frac{q}{t} \qquad (2.23)$$

and
$$\text{Heat rate} = \frac{\text{temperature increase}}{\text{time}} = \frac{\Delta T}{t} \qquad (2.24)$$

Heat flow to the sample depends on either process exothermic or endothermic. As a solid sample melts to a liquid, more heat flowing is required to increase its temperature because of the absorption of heat by the sample as it undergoes the endothermic phase transition from solid to liquid. Likewise, as the sample undergoes exothermic processes (crystallization) less heat is required to raise the sample temperature. DSC also used to observe glass transitions which are widely used in industrial settings as a quality control instrument due to its applicability in evaluating sample purity and for studying polymer curing. As seen in the diagram (Figure 2.19), the sudden upward slope at the glass transition (T_g) indicates the equipment was required to supply more heat to the sample head to maintain a constant heating rate.
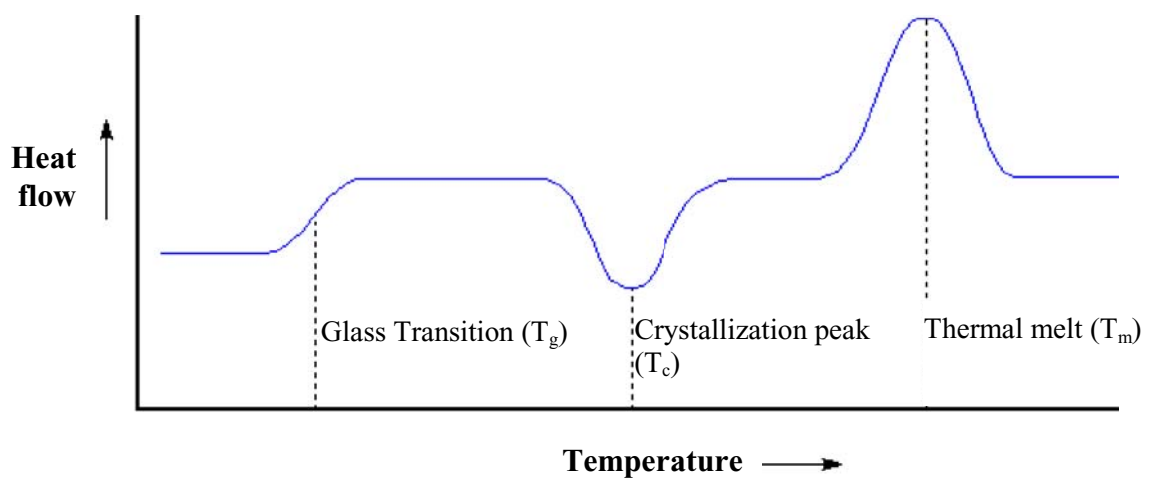
Figure 2.19 Thermogram observed form DSC.

2.6 Incorporation of the Polymer Components into IC Technology

For the 21st century, the development of smart materials emphasize on enabling technology to decrease in both size and power consumption of complex digital systems. This decrease in size and power gives rise to the concept of wearable devices in which digital systems are integrated in everyday personal belongings, like clothes, watch, glasses, etc. Recently, the interest in the developing of a wireless sensor and actuator network is rising. The networks could potentially be used for a wide variety of applications such as monitoring temperature, light, and the location of persons in commercial buildings to control the environment in a more energy efficient manner, sensing harmful chemical agents in high traffic areas, monitoring fatigue crack formation on aircraft, monitoring acceleration and pressure in automobile tires, etc.

The manufacturing of integrated circuit (IC), power circuit design and networking techniques highlight in reducing the total power requirements of a wireless sensor node as low as microwatts (Chandrakasan *et al.*, 1998; Davis *et al.*, 2001; Rabaey *et al.,* 2002). Unfortunately, powering a large number of nodes in a dense network became a critical problem because of the restrictive cost of wiring power to them or replacing batteries. Therefore, the system must be small enough to conveniently place and use nodes which place severe limits on their lifetime if powered by a battery that is meant to last the entire life of the device.

Advances in low power design bring about to the possibility of harvested energy from the environment to power electronic circuits. In these situations, power for use to motivate small electrical systems can be generated from converting sunlight, mechanical vibrations, or heat energy into electrical energy. Among these ambient sources, solar power is the most familiar ambient energy, power output of an energy harvested can range from 15 mW·cm^{-3} in outdoors to 6 μW·cm^{-3} in an office setting. However, mechanical energy which usually vibrates with the use of piezoelectric material, a form transducer can be enclosed to protect it from a harsh environment, and it functions in a constant temperature field. Piezoelectric materials are able to interchange the electrical energy and mechanical strain or force as high as 200 μW greater than that of thermal power (15 μW)

(Erick *et al*., 2005), these power densities are reasonable when compared to rechargeable lithium battery which is only 7 µW·cm^{-3} for a one year lifetime. The reduction of peak power is compensated for the harvester being able to produce the same power output throughout its life while the battery's power tapers off with time.
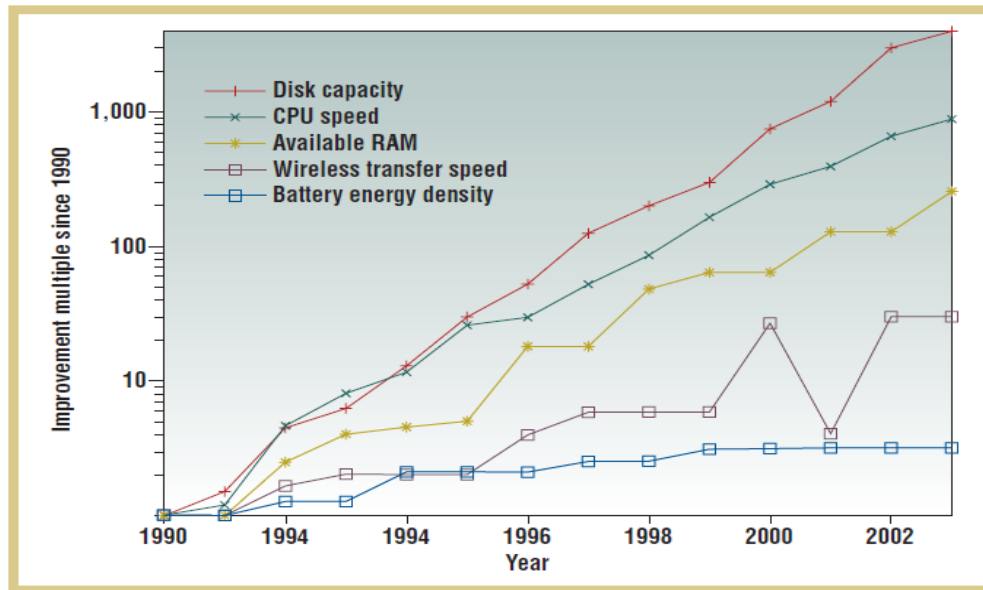
Figure 2.20 Improvements in laptop technology from 1990 to 2001 of available
energy in terms of weight and volume (Paradiso and Starner, 2005).

Although the trends in technology stress is in the decrease in size, weight and power consumption of complex digital systems. However, batteries mass are still a significant percentage of digital systems. Wireless sensor nodes can harvest the energy from the environment while wearable peripherals can generate power from human actions or from the phenomena they sense. They are both areas where harvested energy is an interesting alternative to batteries. From Figure 2.21 the power density available from solar cells, mechanical vibrations, depends on the environmental conditions and no limited lifetime. On the other hand, batteries technology provides enough energy for wireless sensors only in 1 year or less leading to they are not recommended as the power source of the sensor due to the limited lifetime (Roundy, 2003).
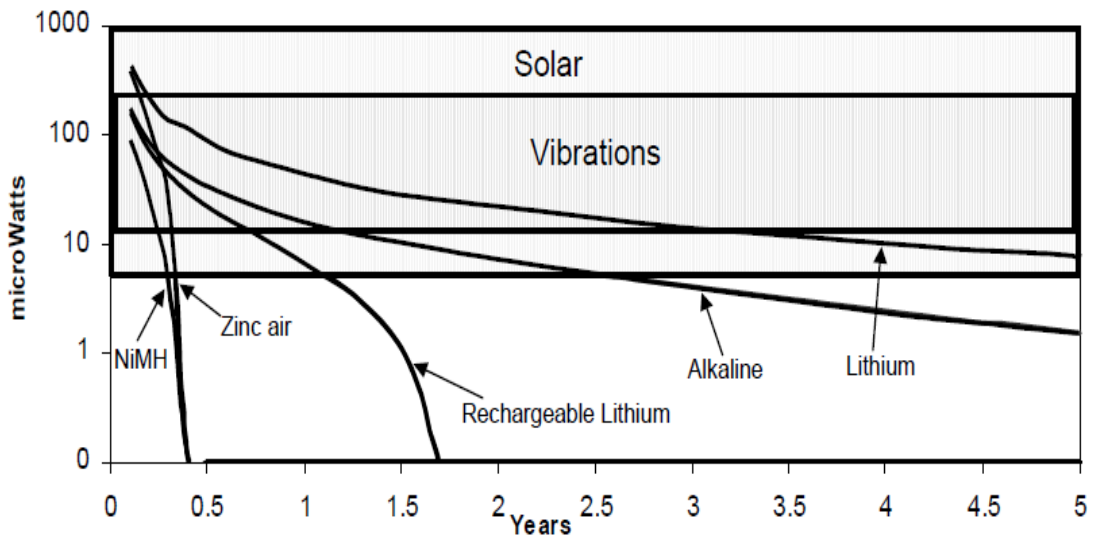
Figure 2.21 Power density (μW·cm^{-3}) as function of lifetime for batteries, solar cell, and vibration based power (Roundy, 2003).

Designing circuits for minimizing the energy wasted requires a thorough understanding of the behavior of the energy harvester as well as new ideas and methods of approaching circuit design in a low power yet highly flexible way. The requirements for the system to be presented are that it be incorporated into one possible division which is to distinguish between active and passive harvesting energy method. The active powering of electronic devices takes place when the user of the electronic product has to do a specific work in order to power the product that otherwise the user would not have done. Unlike active powering, the passive powering of electronic devices does not require external sources. Not only common form of powering desired but hybrids are also being utilized; the semi-passive and semi-active methods. The former method does not require operative energy and computing power necessarily low so that the systems can be self-sustained. The latter method refers to a simple battery which loads power drawn is not necessarily low even if it requires low energy operative. The basic categories are shown in Table 2.1.

Table 2.1 Energy Harvesting Circuitry (Green, 2005)

Approach	Attributes	Configuration
(1) Passive Rectifier Circuit	Low power generation	Piezo → Diode Bridge → Voltage Regulator → Storage
(2) Resonant Rectifier Circuit	Higher power generation, narrow frequency range	Piezo → Diode-Inductor → Voltage Regulator → Storage
(3) Active Switching Circuit	Higher power generation, wide frequency range	Piezo → Switching Amplifier → Voltage Regulator → Storage
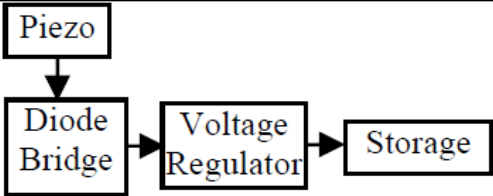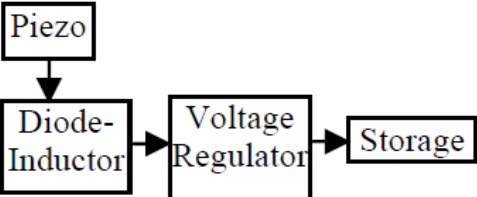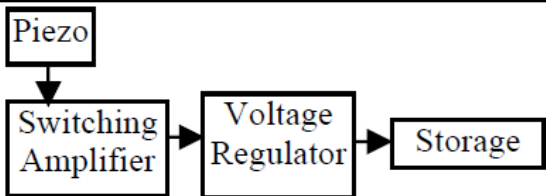
Among these techniques, this work focuses merely on the passive technique which there is two different methods. The principal of technique used in both methods consider the structural damping and losses. The first method is simply placed a piezoelectric material on the structure which degrade mechanical energy into viscous losses as heat so that this phenomenon refers to a damping effect (Johnson, 1995, Sun *et al*., 1995). Not only test mass but also additional mass is also widely used for vibration damping (Gandhi and Chapuis, 2002) The physical principle of this technique consists of the inductance and resistance properties. The inductance and resistance have to ensure the maximization of energy conversion and the dissipation energy which lead to a degrading of mechanical energy in the structure. The optimal inductance and resistance present as the relation of the coupling coefficient (k), blocked the capacity (C_0) and the resonance frequency (f_r). Commonly, the solution of the system identify simply as a use of a resistance which can be presented by (2.25) (Law *et al*., 1996; Badel, 2005), while the damping performance are then enormously decreased induced by (2.26).

$$R = \frac{1}{C_0 2\pi f_0} \tag{2.25}$$

$$A_R = \frac{1}{1 + \dfrac{k^2 Q_M}{2}} \tag{2.26}$$

The active technique has been proposed to overcome the limitations of purely passive technique. The active processing consist of sensor, controller, amplifier and actuator, thus, the possible control laws are unlimited, allowing effective control (lead to a large damping), strong and multimodal. It is possible to control the mass, stiffness or the damping coefficient. The general principle of active control is to generate a wave interacts with waves from the excitation to minimize them. Despite their performance and robustness, active control techniques vibration suffer from major drawbacks; require a source of external energy which is generally high, and therefore the active techniques can be fed by micro-generators schedules. Therefore, this technique control is very important and often complicated. Moreover, their complexity makes the design and implementation quite difficult; especially if control includes estimator or observer, thus requiring a thorough knowledge of structure such as resonant frequency, quality factors and mechanical coupling.

As previously mentioned, hybrid methods combining techniques purely passive active and have also been proposed to limit this power demand. To obtain an interesting compromise between the performance of active control and simplicity and low power consumption of passive system, it was, more recently, proposed the systems that lie halfway between active control techniques and purely passive. These techniques, strongly nonlinear, require very low power controller, and low operating energy. The technique requires no external energy in the power section; called semi-passive and another require energy limited operation namely semi-active. The semi-passive technique is close to passive while the semi-active derivative technique is rather active. The semi-passive techniques have been proposed to control the stiffness of the open circuit system by switching on a network of capacity and changing the coefficient coupling and hence the resonant frequency (Davis and Lesieutre, 2000). This approach selects the resonant frequency of the system in a discrete ranging from the resonant frequency of short-circuit (all capacities are

connected) to the resonant frequency of open circuit (no capacity is connected). Using this approach, it is possible to place off resonance and limit the vibration of the structure. The transition from one state to another is considered the state variables this means that on a single system with one degree of freedom, the velocity and displacement have opposite signs if the system is in a state of stiffness it refers to piezoelectric open circuit, and becomes the a same sign as stiffness in "low" (short circuit).

Piezoelectric vibration-to-electricity converters have received a great deal attention over electromagnetic and capacitive transducer because it has high electro mechanical coupling and doesn't require external voltage source. Moreover, it is particularly attractive for use in MEMS (Choi *et al*., 2006, Fang *et al*., 2006, Horowitz *et al*., 2006, Jeon *et al.,* 2005, Lu *et al*., 2004).

2.7 Summary

This chapter introduces the background on piezoelectricity, crystalline phases of the PVDF and how to enhance the material properties by stretching and poling. The polymer composites and the chemistry relating to the fillers and dispersing agents were included. Fabrication methods, ex-situ and in-situ were described; including the processes existed in industries. These are useful for both material science and engineering viewpoint.

CHAPTER 3

PIEZOELECTRIC PVDF AND THEIR COMPOSITES

This chapter studies the PVDF composite prepared by adding a non-ionic Brij-30 surfactant to create the inner-pores in the matrix in which a metal of high conduction electron density of copper has been homogeneously mixed. The physical and electrical properties of all the samples with and without additives have been discussed, including a range of applications of the material. In this work all the PVDF samples were prepared in bulk form, i.e. cast PVDF with thicknesses of several tens of micron.

3.1 Review of Previous Work

The basic idea in a composite is to integrate several component materials and their properties in a single material. Fillers are used in polymers for a variety of reasons: cost reduction, improved processing, density control, optical effect, thermal conductivity, control of thermal expansion, electrical properties, magnetic properties, flame retardancy and hardness, and tear resistance (Rothon, 2002). Particles that have been used for these purposes were, e.g., fumed silica (SiO_2), nanocrystalline titania (TiO_2; anatase and rutile, alumina (Al_2O_3), and so on (Kima *et al.*, 2006).

Conductive-polymer composites that have been elaborated to improve the physical and electrical properties are ubiquitously used in various applications due to their good electrical conductivity, enhanced mechanical properties, and corrosion resistance. The electrical characteristics of these composites are close to the properties of filler (Park *et al*., 2008; Zhai *et al*., 2008). A critical factor controlling the tribology of polymers is their crystalline morphology. It is evident that the ionic conductivity of metal composite in amorphous phase is two/tree orders of magnitude higher than in crystalline phase (Wang and Dang, 2005). Furthermore, the tribological behavior of composite is expected to change due to the change of morphology after adding fillers into polymer matrix. The improved friction and wear properties were attributed to

changes in crystallinity and reinforcement content (Petrovicova *et al*., 2003). The achievement of conductive properties, therefore, in such heterogeneous polymer-filler system depends on many factors such as particles sizes, surface structures, concentration of filler, interface between filler and polymer (Kobayashi *et al*.,2008). Especially, different concentrations of the fillers need to be well defined for modifying the physical properties of the polymer and to obtain the desired filled polymer for definite potential applications (Camposa *et al*., 2007)

For thermally and electrically conductive polymer composites, carbon black or copper wire are typically used as fillers (Moisala *et al*., 2006). Also, Cu and Ni particle have been used to improve thermal and electrical properties of electroactive polymer film. According to the conductivity which is the product of two important factors: the number of carriers-electrons or holes and carrier mobility, copper is one of the most investigated metals due to its high conduction electron density (8.47 10^{22} cm^{-3}). In a previous report from Dasaesamoh and Muensit (2009), the volume conductivity of the composite increased with electrical conductivity of filler. Measured values of the thermal conductivity were also reported to be 0.255 and 0.810 W·m^{-1} $^\circ$C^{-1} for PVDF/Ni and PVDF/Cu, respectively.

3.2 Materials and Methods

3.2.1 Preparation of the Neat PVDF and Its Composites

The PVDF body can be formed by dissolving the PVDF powder (Aldrich Co.) into *N*-methyl-2-pyrrolidone (NMP) (Aldrich Co.) at 60 $^\circ$C and stirred for 3 h to obtain a PVDF solution (Moisala, 2006). A ratio of PVDF:NMP was selected to be 10:90, 15:85 and 20:80 in order to check the thermal stability and crystallinity. When the solution was cast onto a glass plate, a neat polymer sheet was obtained and it was then dried at 120 $^\circ$C for 6 h to completely evaporate the solvent, and consequently to form semicrystalline structure. When the PVDF solution was added with a non-ionic surfactant which is glycol dodecyl ether (hereafter Brij-30) (Aldrich Co.), the physical properties of the matrix was studied as functions of the concentration of the Brij-30. The necessity of using the Brij-30 as a surfactant is to

reduce the surface tension of aqueous solution and facilitate the metal filler to be able to homogeneously mix with the matrix and also made the hole inside polymer matrix to enhance the piezoelectric properties. Further sample preparation was made by mixing the copper powder (Aldrich Co.) into the modified PVDF matrix to obtain the composites of different concentration of copper. In addition, further adding the copper filler of different ranges of particle sizes, i.e., 1-5 μm and < 50 nm has also been made.

3.2.2 Sample Characterization

Polymer morphology includes the size and shape of fillers and dispersing agent, and the size, distribution and association of the structural units within the macrostructure. X-ray, electron and optical scattering techniques and a range of other analytical tools such as infrared spectroscopy and thermal analysis are commonly applied to determine the structure of polymers.

X-ray diffractometer (Philips X'pert X-ray diffraction system) with Ni filtered CuKa radiation was used to distinguish the phases of the PVDF sample The patterns were recorded at a scan rate of 0.2^o per min from $10°$ to $60°$ for phase and texture analyses. The monomers and phases that exists in the samples can be precisely determined by a Fourier Transform Infra-Red (FTIR) spectra recorded in the range of 4000 - 500 cm^{-1} (Perkin-Elmer, EQUINOX 55, Bruker, with KBr as blank). Thermal analyses were carried out by using a Differential Scanning Calorimetry (DSC) (Perkin Elmer) apparatus at a heating rate of 10 ^{o}C·min^{-1}. All the samples were heated from room temperature (25 ^{o}C) to 200 ^{o}C. Melting temperatures and enthalpies were determined at the onset of the peaks and from the peak areas, respectively. The crystallinity can be calculated from the heat of fusion of the sample to that of a completely crystalline PVDF polymer. In the conventional optical microscope an object was illuminated which revealed in fine detail the specimen at the magnification of about 2000X. Bright field, normal mode of the operation of an optical microscope, was used in this work. The SEM was used to study the surface and bulk structures of samples. Samples were prepared by attaching them to the specimen stub and applying a conductive surface coating. Often polymers such as PVDF do not fracture at room

temperature, or the fracture is ductile, and both impact testing and specimen preparation must be conducted below room temperature. In addition, etching may be required in order to bring out the dispersed phase morphology. For SEM study specimens were immersed in liquid nitrogen for 2-5 min and then fractured. Manual method of freeze fracture is often useful in providing specimens for study in the SEM. Polymer immersed in liquid nitrogen for prefreezing and then fracture the specimen for properties and structural evaluation. For the electrical measurement, dielectric response and electrical conductivity of the sample was measured by HP-4263B LCR Meter and computer controlled HP-4285A LCR Meter in the frequency range of 100 Hz-30 MHz without electrode sputtered.

3.3 Results and Discussion

3.3.1 Crystallographic and Structural Analysis of Neat PVDF and Composites

X-ray diffraction permits the determination of interatomic ordering and chain packing. The morphology of polymers is determined by a wide range of optical and electron microscopy techniques. Polymers are considered to be semicrystalline because they are may not be completely crystalline or amorphous.

Micropatterns of neat PVDF and PVDF with Brij-30 prepared from NMP solution shows peaks at about 18.5º, 26.8º and 39º corresponding to (020), (021) and (100) reflection were clearly revealed in the presence of -phase PVDF (Figure 3.1). While the peak corresponded to (110) at 20° refer to orthorhombic -phase The characteristic peak intensity of the Brij-30 added PVDF shifted to some higher 2 angles due to the polymer-surfactant complex form (Figure 3.1). In the case of PVDF/Cu (Figures 3.2-3.3), two strong peaks were found at 43.5^o and 50.6^o associated with the reflection of Cu. Owing to the high conduction electron density of the copper, the electronic structure and electrical conductivity of the material change with a concentration of the copper filler. The characteristic peak of -PVDF decrease upon on content and surface area of Cu, thereby resulting in the higher electrical conductivity.
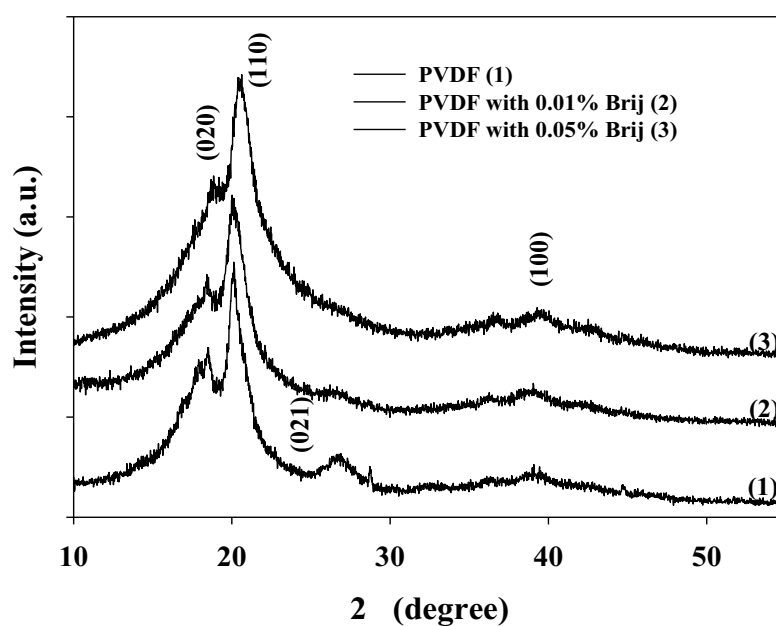
Figure 3.1 XRD patterns of the neat PVDF and the Brij – PVDF sample.
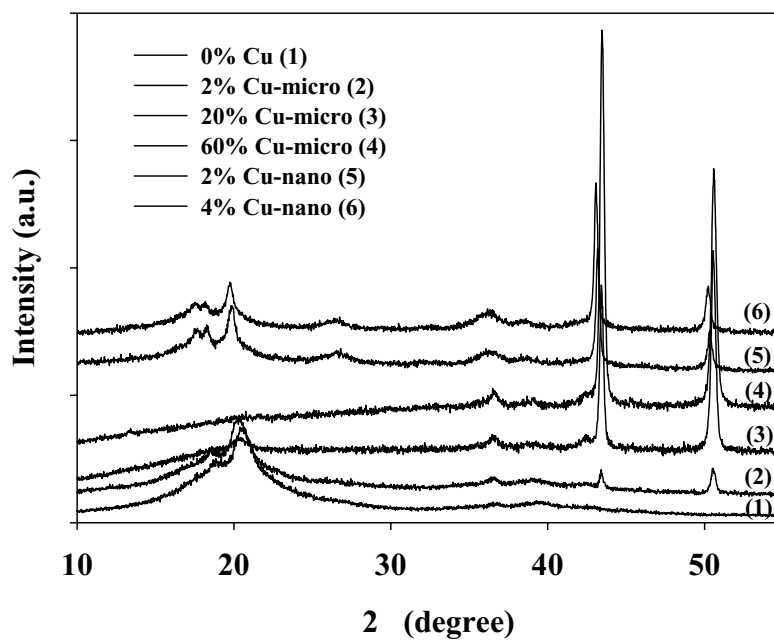
Figure 3.2 XRD patterns of the PVDF/Cu with 0.05% Brij.
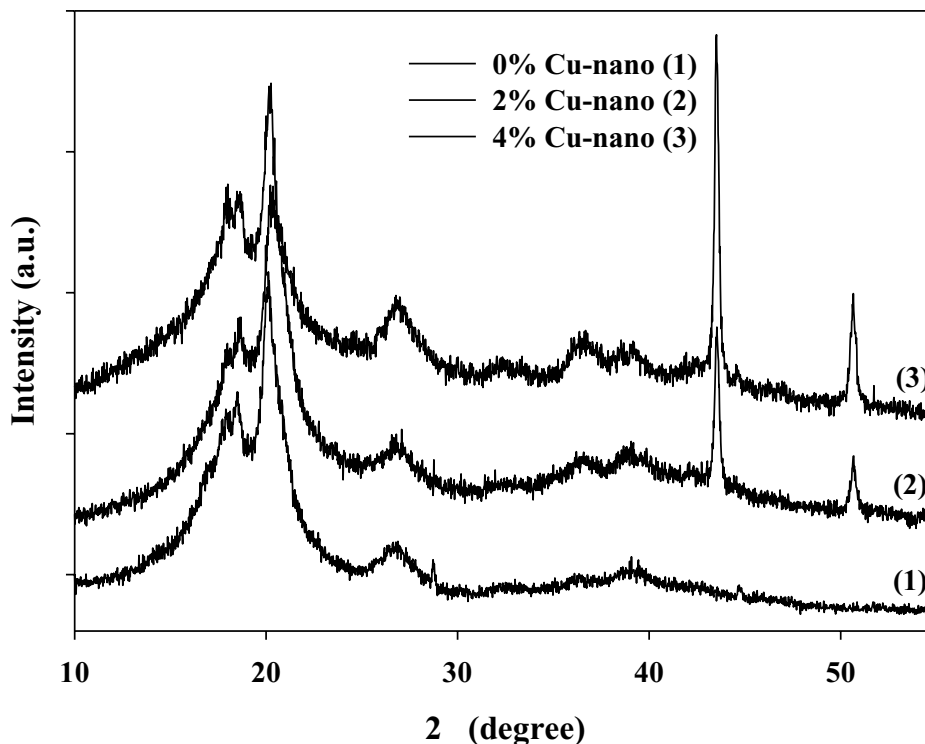
Figure 3.3 XRD patterns of the PVDF/Cu sample.

The infrared spectrometry technique was used to monitor the changes in universal and specific intermolecular interaction, and the conformational composition by the ratio of optical density. Figure 3.4 presents the FT-IR spectrum confirming porous nature of the PVDF with some surfactant. The FT-IR spectrum in the figure ascribed the C=C (874, 1683 cm^{-1}), C-H (835, 1400 cm^{-1}), and C-F (762, 1167, 1230 cm^{-1}) stretching vibrations. The transmittance band in the wave number of about 762, 798, 874 and 1230 cm^{-1} was clearly characteristic for the non polar TGTG conformation as so call the -phase of PVDF. In the case of PVDF/Brij-30 and PVDF/Cu (Figures 3.4-3.6), the peaks of C=C, C-H and C-F was shifted to some higher wave number values and, the percentage of transmittance of fine structure, located at about 1700-700 cm^{-1}. The reduction of transmittance depending on the concentration of Cu associated with the reduction of the crystallinity of the PVDF polymer.
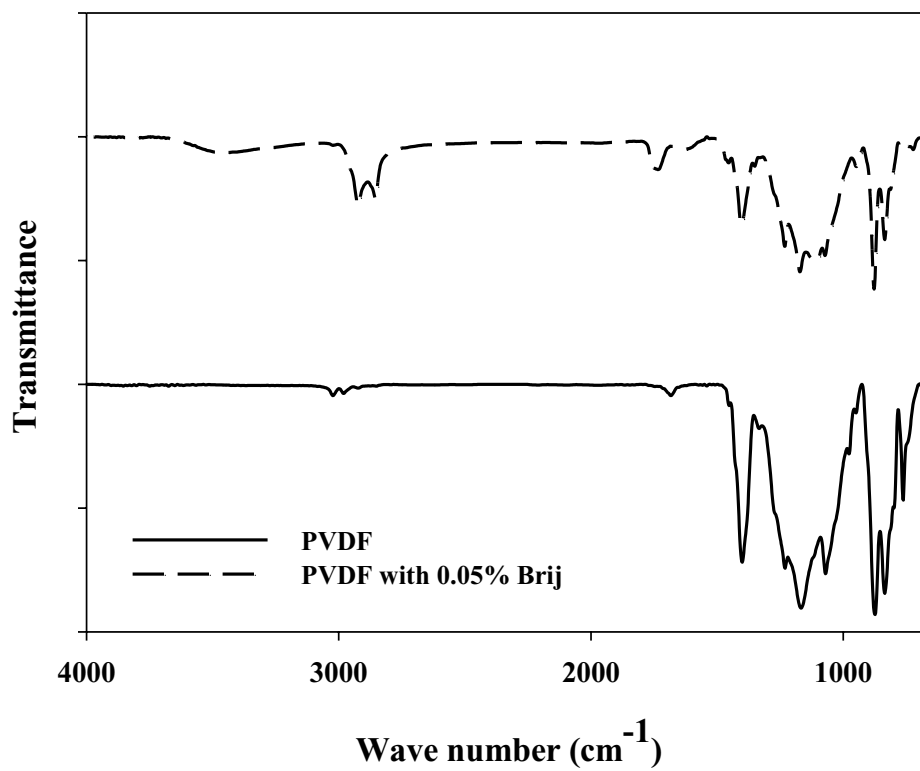
Figure 3.4 FT-IR spectra (not to scale) for the neat PVDF and
PVDF with 0.05%Brij.
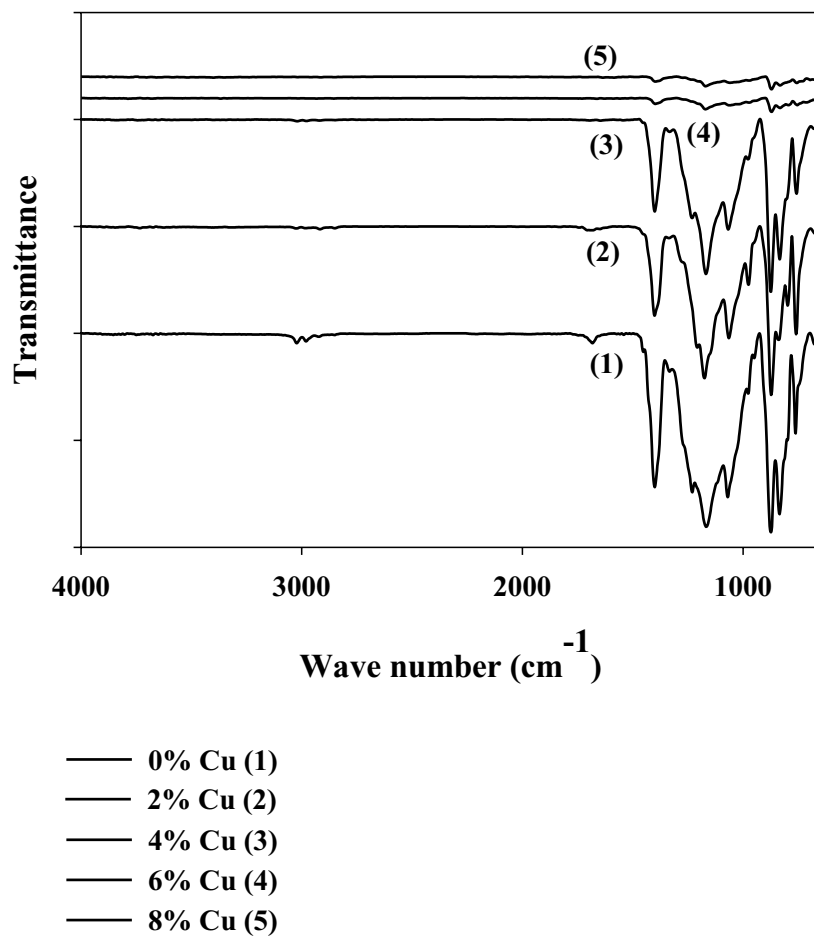
Figure 3.5 FT-IR spectra (not to scale) for the PVDF/nano-Cu.
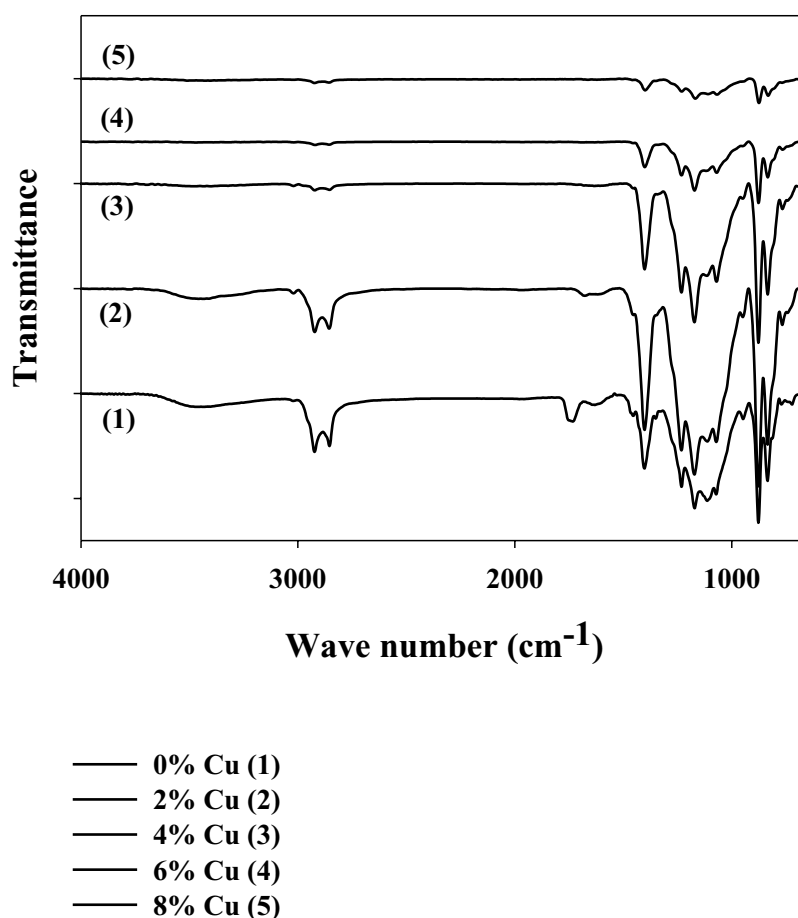
Figure 3.6 FT-IR spectra (not to scale) for the PVDF/nano-Cu with 0.05% Brij.

DSC is one of the most informative ways of studying polymer caused by irradiation. The volume of information naturally increases when DSC is combined with X-ray diffraction analysis and IR spectroscopy. As discussed above, IR was used to identify the branching content and functional groups present in the transmittance band at 4000 - 500 cm^{-1}. Carlorimetry was used to determine the changes in enthalpy H (in the energy of intermolecular interaction). Melting as a phase transition is characterized by a stepwise increment of the basic thermodynamic parameter such as the enthalpy (H), entropy (S), and the volume (V). The equilibrium melting point of polymer crystals is determined by their enthalpy and entropy of melting in equation 3.1

$$T_m = \frac{\Delta H_m}{\Delta S_m} \qquad (3.1)$$

It is well known that T_m for polymer is higher when the intermolecular interaction is greater (ΔH_m is greater) and the chains are more rigid (ΔS_m is lower). Additionally, the entropy increases with increasing chain flexibility and is low for rigid macromolecule (Bersthtein and Egorov, 1994).

One of the important applications of DSC in practice is determination of the degree of the crystallinity of polymers from the value of enthalpy of sample. The relative percentage of crystalline as showed in Figures 3.7-3.8 was calculated based on the equation (3.2)

$$\text{Crystallinity (\%)} = \frac{\Delta H_m}{\Delta H_m^0} \times 100\% \qquad (3.2)$$

Where ΔH_m^0 is the enthalpy of the melting of 100% crystalline PVDF, 104.7 J·g^{-1} (Hongbing et al., 1998), and ΔH_m is related to the sample.

Figure 3.7 displays the thermogram of the neat PVDF sheets of 3 different PVDF:NMP ratios. Using the automated tolerance test calculation, the incoming material's melting temperature of the 20wt% PVDF represented two endothermic peaks. One can often observe the presence of two or more endothermic peaks on DSC curves for partly crystalline polymers. This multiplicity has several causes; reorganization of metastable crystals from folded chains, recrystallization of folded chain crystal, phase transitions in solid polymers preceding melting, the presence of crystals varying in structure in a polymer, melting and isotropization of liquid-crystalline polymer, the presence of crystals of two or more sizes, the formation of new (secondary) crystals because of low-temperature annealing, termed 'cold crytallization', the melting of the initial and defective crystals in irradiated polymer and the appearance of inter- and intramolecular melting steps in a highly oriented polymer. Recrystallinzation here implies a cycle of partial or complete melting of the initial lamellae (a low-temperature endothermic peak), subsequent recrystallization with the formation of new, larger lamellae and their melting at a higher temperature. Additionally, it was obvious that the 20:80 PVDF sample had superior crystallity

while its melting temperature (159 ºC) was roughly the same as the others. However, the flow of the 20:80 PVDF solution is relatively hard because of its relatively high viscosity (68,000 cp). So we have chosen the 10:90 PVDF solution (2,480 cp) as the matrix hereafter (Thimonta, 2006).

The information from Table 3.1, accordingly, and the relationship between melting temperature, enthalpy and entropy describe by Bersthtein and Egorov (1994). It can be noted that the additive reagent and copper filler nano-size lead to the increase in melting temperature of PVDF composite because of the higher melting temperature of additive reagent and filler. Whereas, the lowering of melting temperature in the case of copper micro-size as a result of low intermolecular interaction which corresponds to the decline of enthalpy. Further, additive reagent and copper fillers; both of micro- and nano-size, resulted in the reduction of entropy and crystallinity (Figures 3.10-3.11) of samples which influence to the diminution of sample flexibility. It can be noted that the crystallinity of composite increased as the low load of Cu filler (2%) was added in the PVDF matrix. This result was probably because of the electronegative of Cu which infiltrated in the amorphous region induced the rearrangement of PVDF chain to form a crystalline region. The crystallinity reduced, however, as Brij-30 was added due to the reaction between Cu and head/tail group of Brij-30. Furthermore, the reorganization of folded chain crystals during slow heating (10 $^{o}C \cdot min^{-1}$) in a calorimeter, causes its melting point to increase in the case of composite film adding with additive reagent. The structural reorganization of non-equilibrium crystals, with the thickening of thinner lamellae, occurs in the solid phase prior to melting and increases when approaching T_m (Bersthtein and Egorov, 1994).
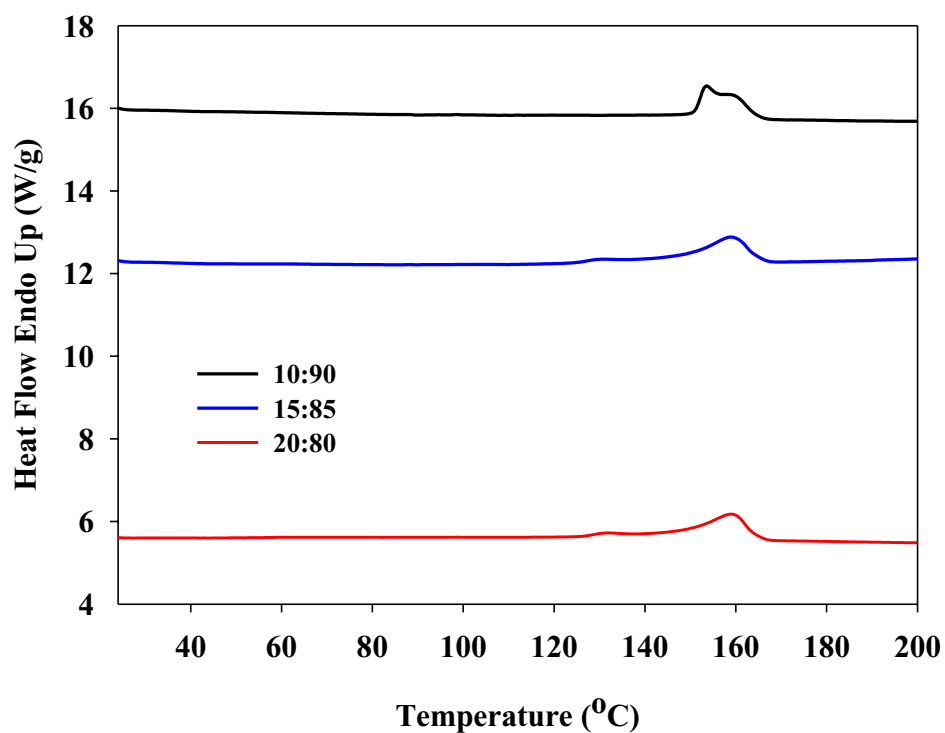
Figure 3.7 DSC thermograms of the neat PVDF with different PVDF:NMP ratios.

Table 3.1 The melting temperature, enthalpy, and entropy of neat PVDF (10:90 for PVDF:NMP), PVDF with Brij-30 and their composite with about 1-5 µm and <50 nm copper at various contents.

Sample	Surfactant (%)	Cu (%)	T_m (^{o}C)	H (J/g)	S
PVDF	0.00	-	159.5	41.6	0.26
	0.05		161.5	23.4	0.14
PVDF/Cu-micro	0.05	2	160.5	30.0	0.19
		30	163.2	13.4	0.08
		50	162.0	6.4	0.04
		60	162.0	3.7	0.02
		70	159.5	2.76	0.02
PVDF/Cu-nano	-	2	157.2	49.4	0.31
		4	157.7	42.6	0.27
		6	158.3	35.0	0.22
		8	158.1	27.0	0.17
	0.05	2	162.8	18.3	0.11
		4	163.3	36.6	0.22
		6	163.4	29.2	0.18
		8	163.3	19.5	0.12
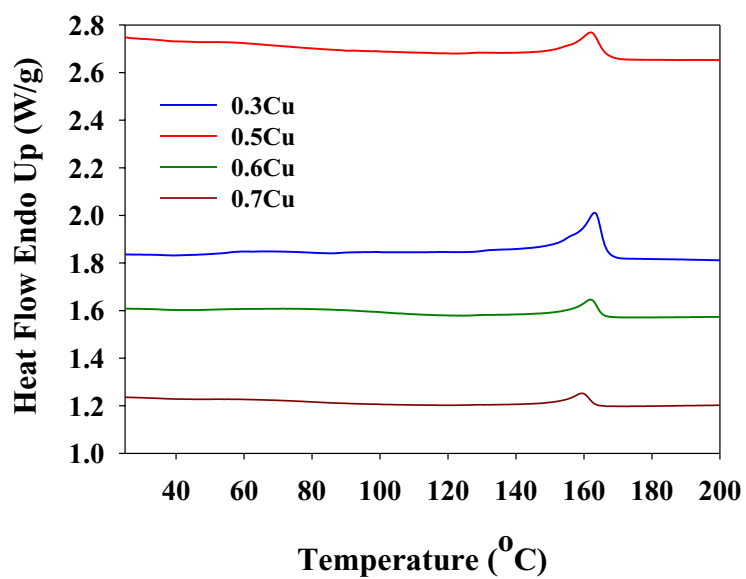
Figure 3.8 DSC thermograms of the PVDF/ micro-Cu with 0.05%Brij.
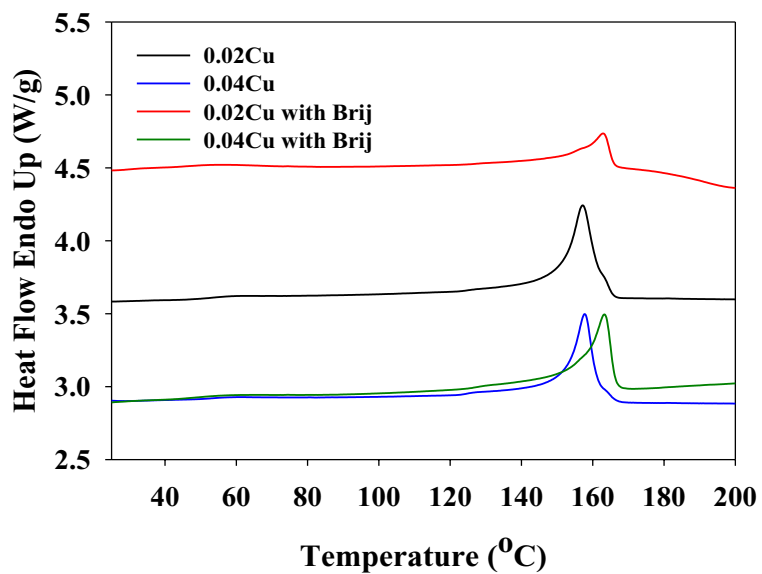
Figure 3.9 DSC thermograms of the PVDF/nano-Cu.
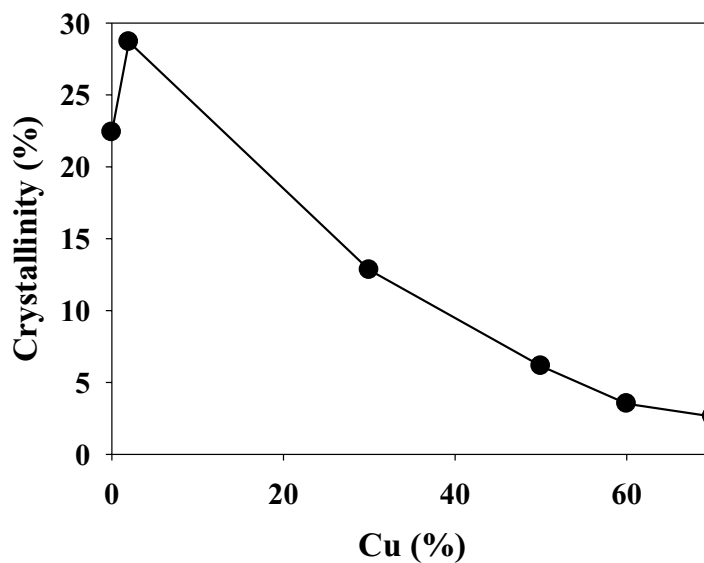
Figure 3.10 Effect of Cu concentration on the crystallinity (%) of PVDF/ micro-Cu with 0.05% Brij.
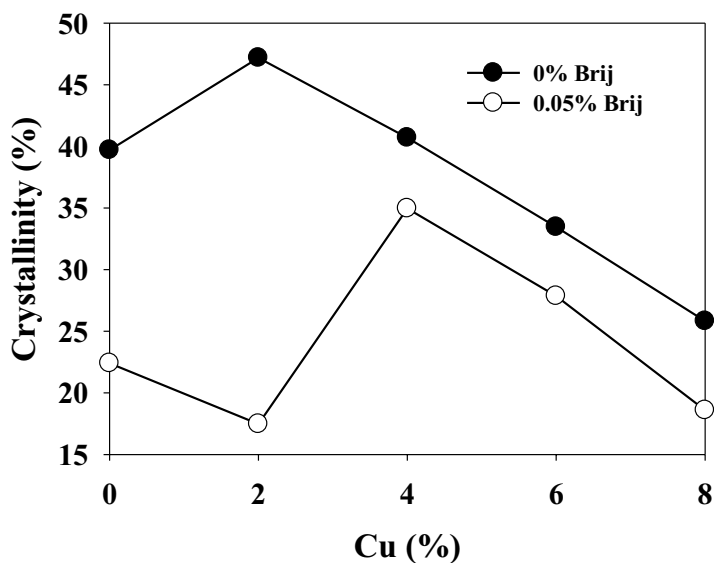
Figure 3.11 Effect of Cu concentration on the crystallinity (%) of PVDF/ nano-Cu with and without Brij.

Direct observation of morphology using a digital camera and an optical microscope provides information relating to the size and distribution of the fillers. A

planar view of the neat PVDF reveals the rough surface as shown in Figure 3.12(a). Even though, this bright field micrograph cannot display the spherulitic texture which is indicated in the crystal structure. However, this micrograph should indicate the spherulitic texture when compare to micrograph of nylon pellet Figure 3.12(b). The distribution of the copper particles can be seen in Figures 3.13-3.19. The color of the films, the copper cluster size and their relationship within the polymer are clear at this magnification. The morphology tone and the cluster size depended extremely on the concentration of copper and the surfactant. The cluster became larger in the samples without using additive reagent to reduce the surface tension of copper particles (Figures 3.13-3.16).

The configuration (Figure 3.20) consisting of spherical inclusions of copper embedded in a surfactant-polymer matrix that is covered with a homogeneous medium whose properties average approximately the average composite properties were studied in Section 3.4.2.

(a)

(b)
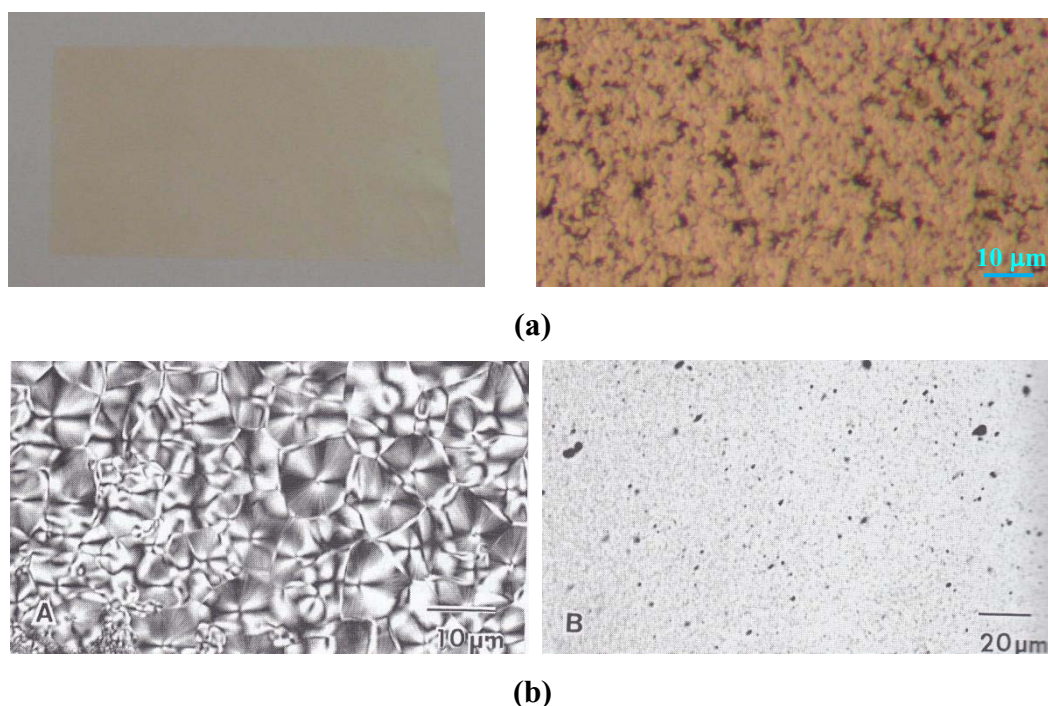
Figure 3.12 Morphology of (a) the neat PVDF characterized by (left) digital camera, (right) optical microscopy and (b) the nylon pellet characterized by optical microscope (left) in polarized light, (right) in a bright field (Sawyer and Grubb. 1996).
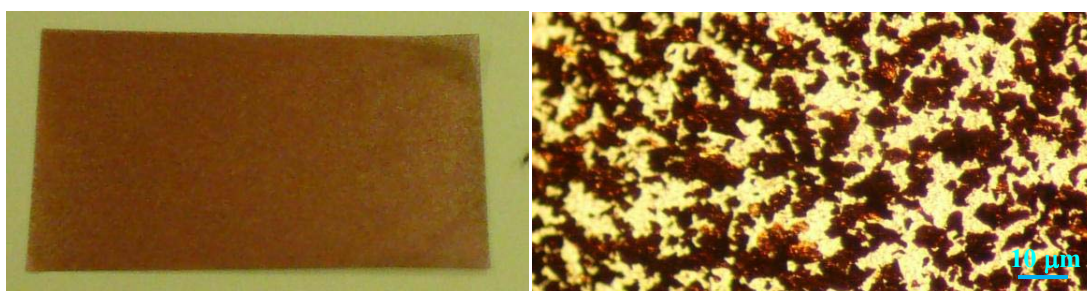
(a)   (b)

Figure 3.13 Morphology of PVDF/0.02 micro-Cu by

(a) digital camera and (b) optical image
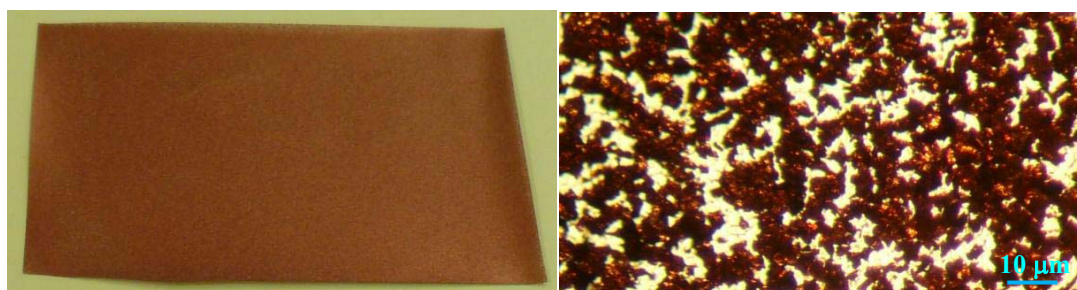
(a)   (b)

Figure 3.14 Morphology of PVDF/0.04 micro-Cu by

(a) digital camera and (b) optical image
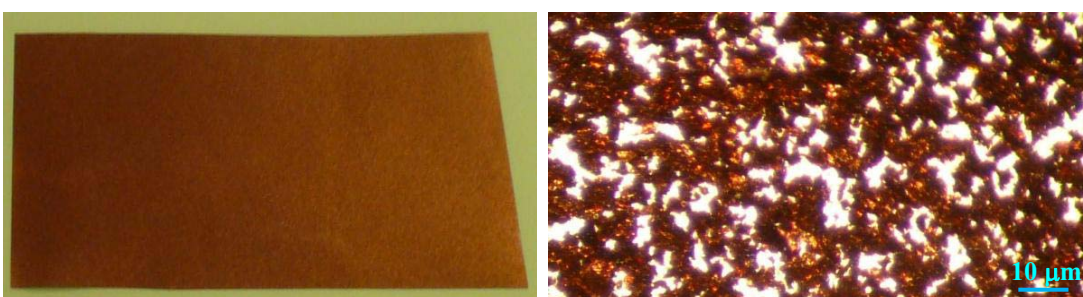
(a)   (b)

Figure 3.15 Morphology of PVDF/0.06 micro-Cu by

(a) digital camera and (b) optical image.
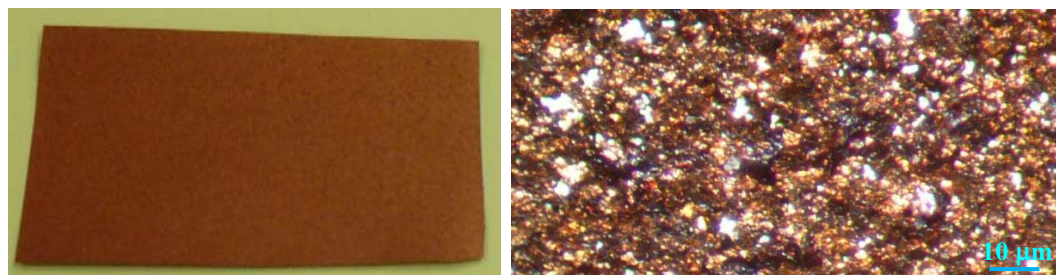
(a) **(b)**

Figure 3.16 Morphology of PVDF/0.08 micro-Cu by

(a) digital camera and (b) optical image.
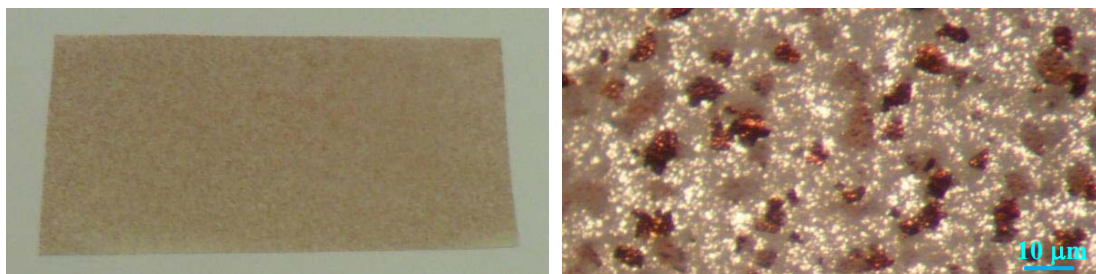
(a) **(b)**

Figure 3.17 Morphology of PVDF/0.01 micro-Cu with 0.05%Brij by

(a) digital camera and (b) optical image.
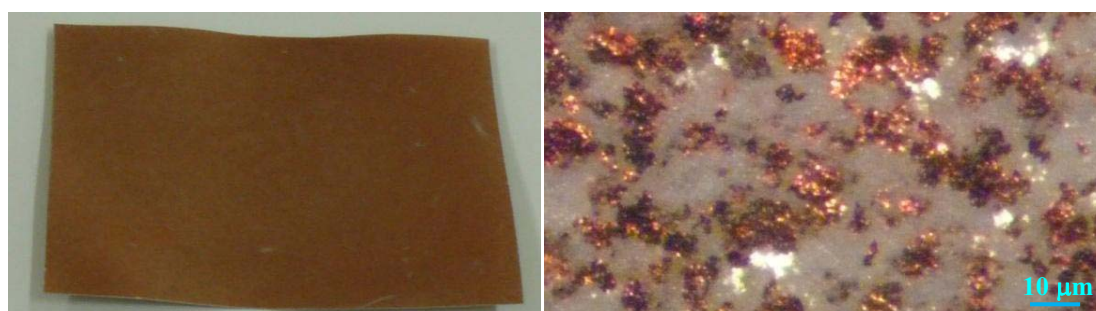
(a) **(b)**

Figure 3.18 Morphology of PVDF/0.03 micro-Cu with 0.05%Brij by

(a) digital camera and (b) optical image.

(a)   (b)
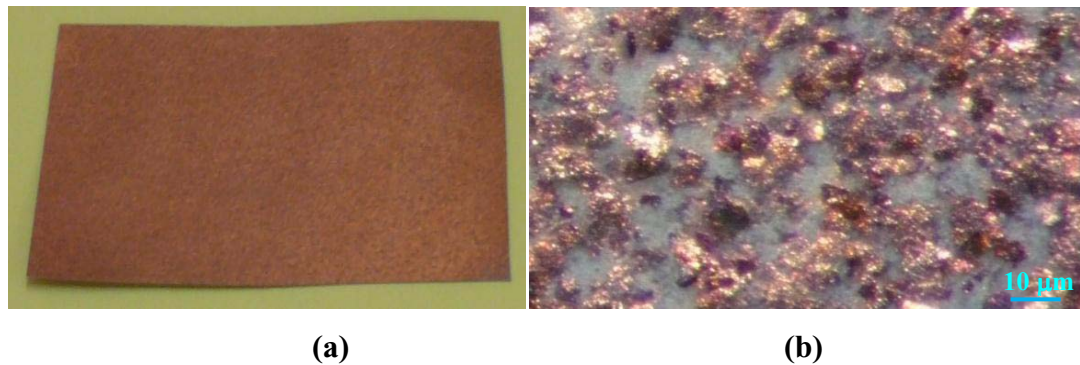
Figure 3.19 Morphology of PVDF/0.1 macro-Cu with 0.05%Brij by (a) digital camera and (b) optical image.
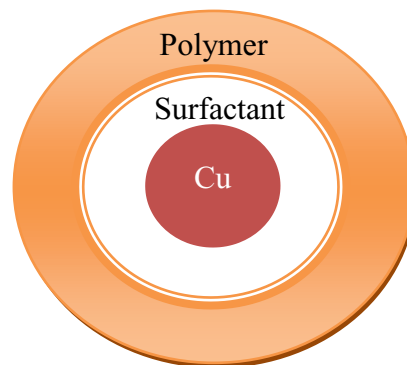
Figure 3.20 Schematic picture for a copper inclusion embedded in an additive reagent and polymer which, in turn, is surrounded by a homogeneous medium whose properties can approximately be the average properties of the composite.

Although, a light microscope is cheaper than a scanning electron microscope and there are almost no problems of adverse interactions between the specimen and the radiation used. However, the scanning electron microscope provides substantially higher resolution in several modes of operation and, through accessories, element analysis of very small volume.

Studies of the relation of structure to the mechanical behavior of filler reinforced composited are commonly encountered as these materials find application in both structural and nonstructural application. The fracture behavior of composite was affected by many variables, including the nature of the filler and matrix, film orientation. SEM examination of the failure zone may reveal all of failure mode with

no clear evidence of the initiation site. Additionally, this method did not reveal the spherulitic texture in both planar and cross section view. Therefore, the study of microstructure by using the SEM method which provides some insight into the nature of the surface was required. Figure 3.21(a) and (b) exhibited the different morphology between top and bottom surface of neat PVDF. It was shown that the bottom surface was much smoother than that of the top surface because the annealing process started at the top surface when solvent molecules diffuse from the gap between the boundaries of the particles in the film or in gel areas of the film, and then infiltrate from the gel surface to the bottom of the film and then dried in the upper surface (Dobler and Holl, 1996). Creation of pores/holes may be due to the incompletion of polymer chain packing during evaporation. The fracture morphology in Figure 3.21(c) indicated the dense structure without pore of the neat PVDF and also showed the typical fatigue failure initiated at the bottom surface. Moreover, the view of top surface displayed an oriented crystalline PVDF film surface with radial form.
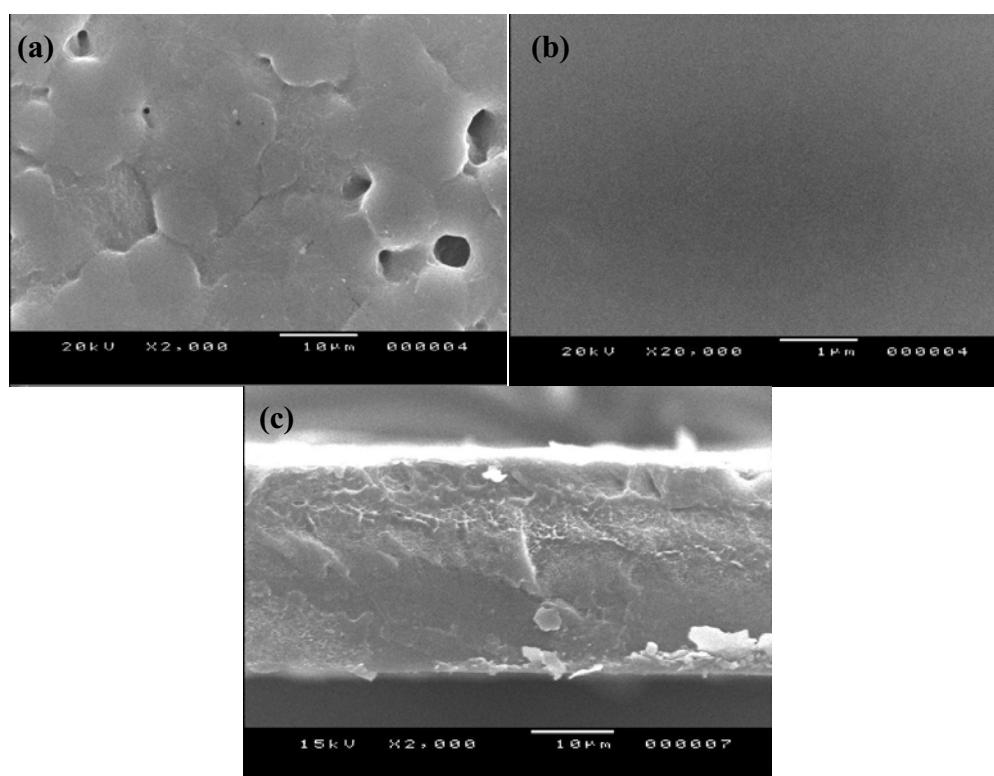
Figure 3.21 SEM images of the (a) top surface, (b) bottom surface and
(c) cross-section of the neat PVDF.

SEM images of copper-embedded PVDF film represented dense structure in both planar and cross section views (Figures 3.22-3.25). The dispersed phase polymer specimens had significant distinguishable particles; at least 2% copper was presented. Semi-crystalline polymer films with particles but without order and macro-void (10 μm) were observed in planar view whereas the cross section view exhibited fine dispersion of filler with low adhesive force. Moreover, the agglomeration of copper filler depended strongly on its concentration and is much larger than that of the composite film adding with the surfactant which will be discussed below.
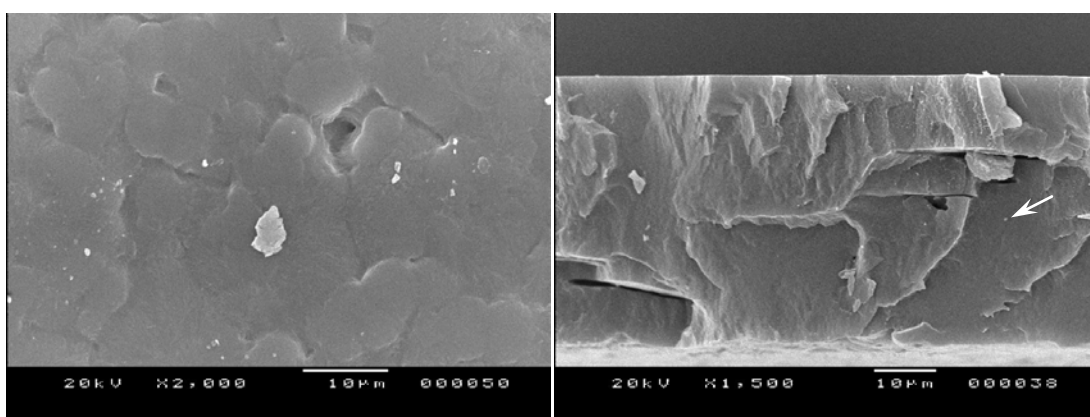
Figure 3.22 SEM images of the planar (left) and cross-section (right) of the PVDF/0.02 micro-Cu that revealed the fine particle inserted in the texture with low adhesive (arrow).
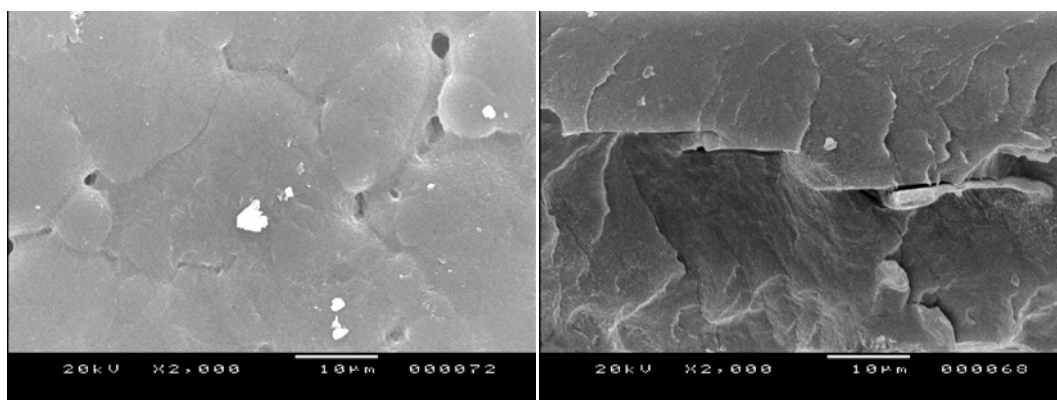
Figure 3.23 SEM images of the planar (left) and cross-section (right) of the PVDF/0.04 micro-Cu.
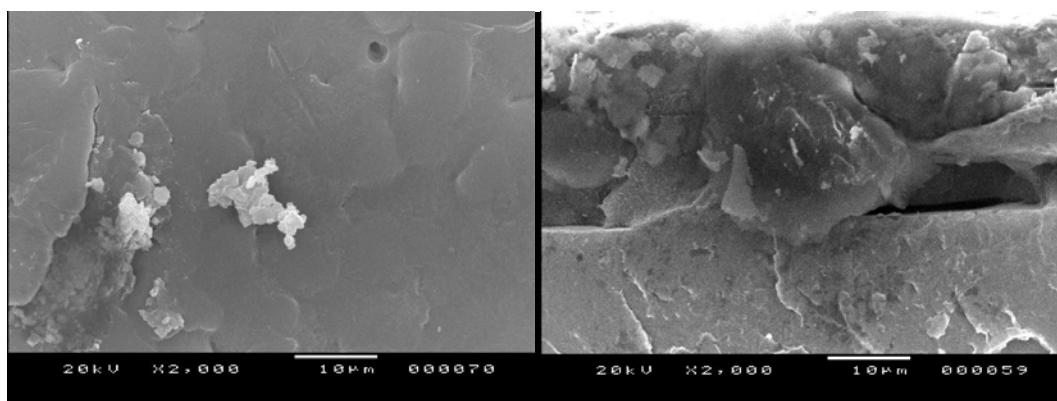
Figure 3.24 SEM images of the planar (left) and cross-section (right) view of the PVDF/0.06 micro-Cu.
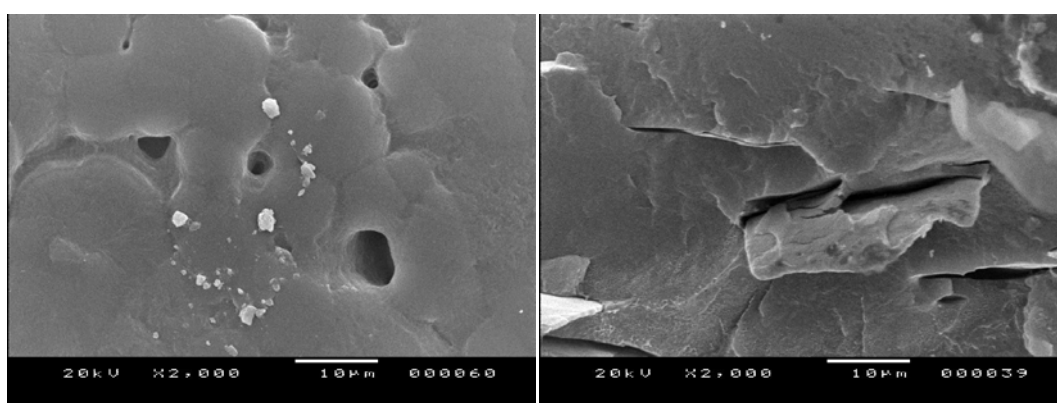
Figure 3.25 SEM images of the planar (left) and cross-section (right) view of the PVDF/0.08 micro-Cu.

Surfactant reagent showed network morphology which displayed that both the matrix and the dispersed phase particles were more complicated by chemical reaction. This is probably because polyelectrolyte gel-surfactant complex was formed when a polyelectrolyte gel was placed in the solution of oppositely charge surfactants which could generate hydrophobic-hydrophilic phase separation. The porous structure seen in Figures 3.26-3.29 had pores throughout the area with the dimension of pores in the range of 2-5 μm which were mainly found underneath the surface. The porosity increased from 70% for 0.01%Brij-30 to 80% for 0.05% Brij-30. Moreover, the coarse and irregular shaped pore with macrofibrils were observed (arrow in Figure 3.27).
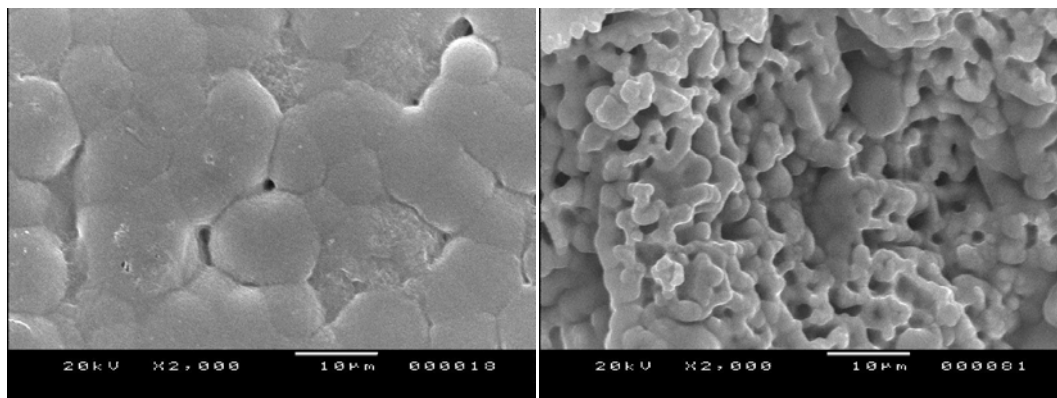
Figure 3.26 SEM images of the planar (left) and cross-section (right) of the PVDF with 0.01%Brij.
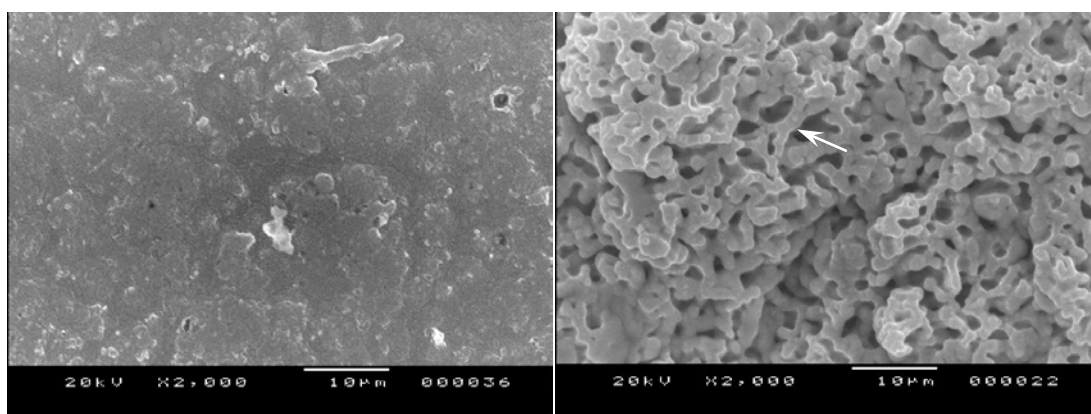
Figure 3.27 SEM images of the planar (left) and cross-section (right) of the PVDF with 0.05%Brij.
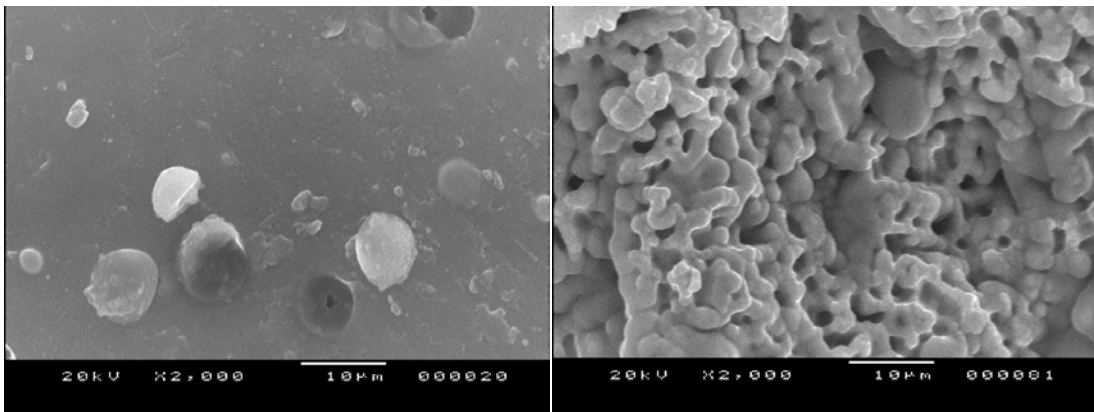
Figure 3.28 SEM images of the planar (left) and cross-section (right) of the PVDF/0.01 micro-Cu with 0.05%Brij.
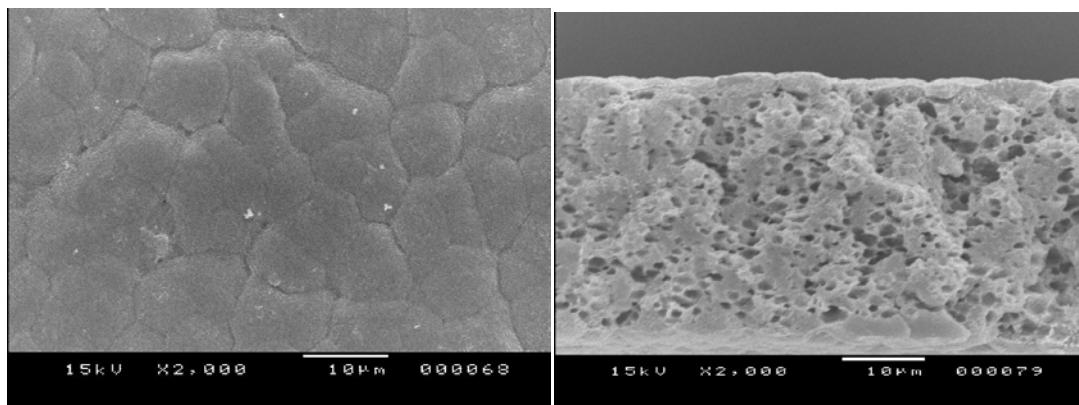
Figure 3.29 SEM images of the planar (left) and cross-section (right) view of the PVDF/0.01 micro-Cu with 0.05%Brij.

As discussed above, the surface of the composite film were generally dense (Figures 3.22-3.25), but it became a porous texture when adding the surfactant (Figure 3.26-3.29). The structure of composite adding with surfactant, however, had not the porous texture (porosity 40-60 %) as much as the neat PVDF adding with surfactant (porosity 80%) probably caused by the reaction of surfactant to copper filler as displayed in the Figure 3.30-3.33. There is an open porous structure with a pore gradient, with smaller pores nearer the dense top and bottom surface (Figure 3.30). Moreover, it can be noted that a nucleopore film had more define pore structure with rounded pores that were not bored through from one side to the other. As the

concentration of copper filler was raise up to 10% the particles were clearly presented on the top surface of the film (Figure 3.32). When the copper concentration was raised as high as 60%, it indicated that the active phase of this composite is copper and the passive phase (discrete phase) is PVDF, an amorphous structure was extremely observed.
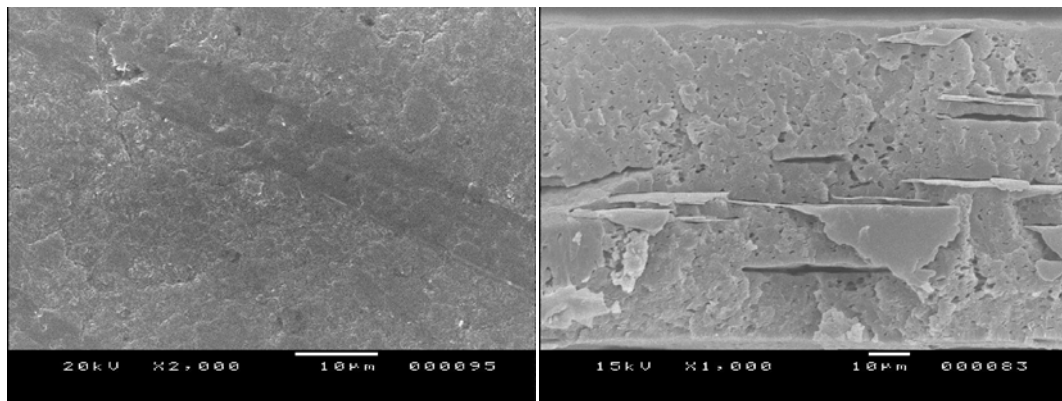
Figure 3.30 SEM images of the planar (left) and cross-section (right) of the PVDF/0.02 micro-Cu with 0.05%Brij.
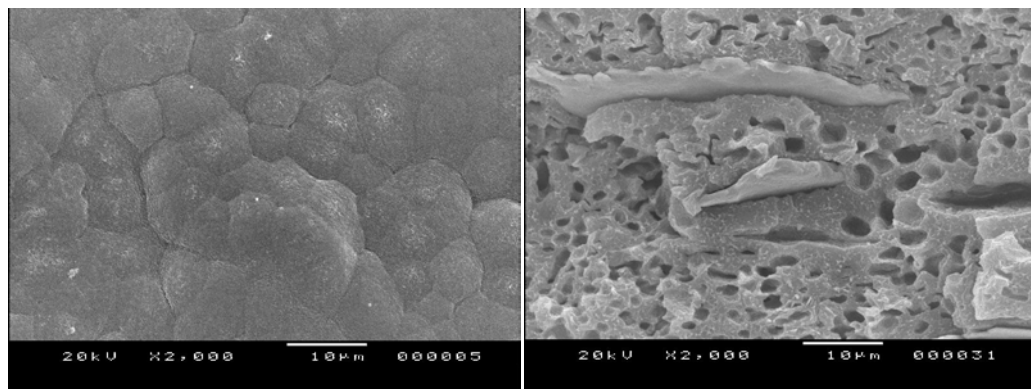
Figure 3.31 SEM images of the planar (left) and cross-section (right) of the PVDF/0.08 micro-Cu with 0.05%Brij**.**
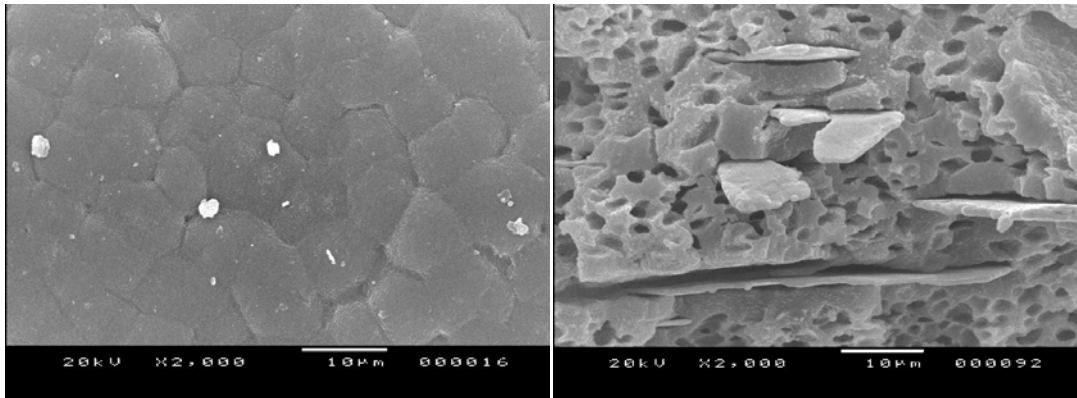
Figure 3.32 SEM images of the planar (left) and cross-section (right) view of the PVDF/0.1 micro-Cu with 0.05%Brij.
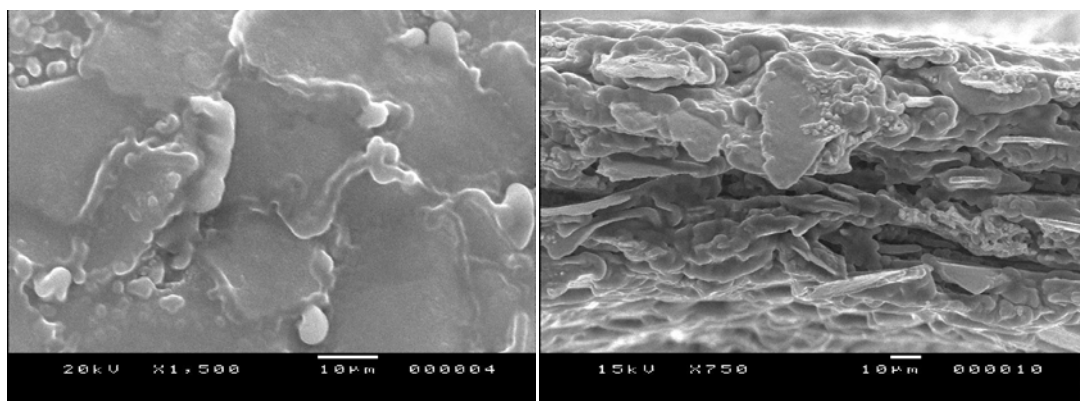
Figure 3.33 SEM images of the planar (left) and cross-section (right) view of the PVDF/0.6 micro-Cu with 0.05%Brij.

The effect of copper filler size to morphology of composite film can be observed in Figures 3.34-3.35. The result in Figure 3.34 shows large dispersed phase particles and submicrometer sized particles and holes. An interesting comparison of porous structure of composite using the micro- and nano-copper particles as filler was shown in Figure 3.36. It shows that the properties of composites composing of micro-size particles, as well as those compose of nano-size particles depend strongly on the surface area.
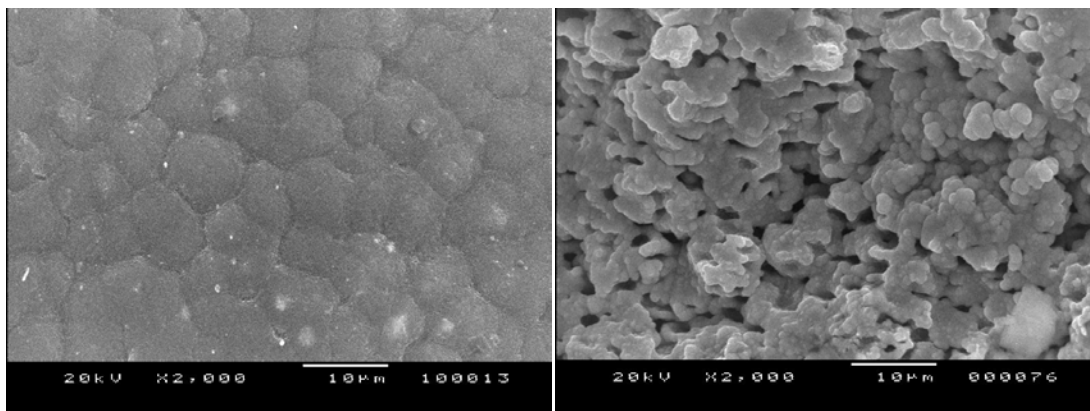
Figure 3.34 SEM images of the planar (left) and cross-section (right) view of the
PVDF/0.02 nano-Cu with 0.05%Brij.
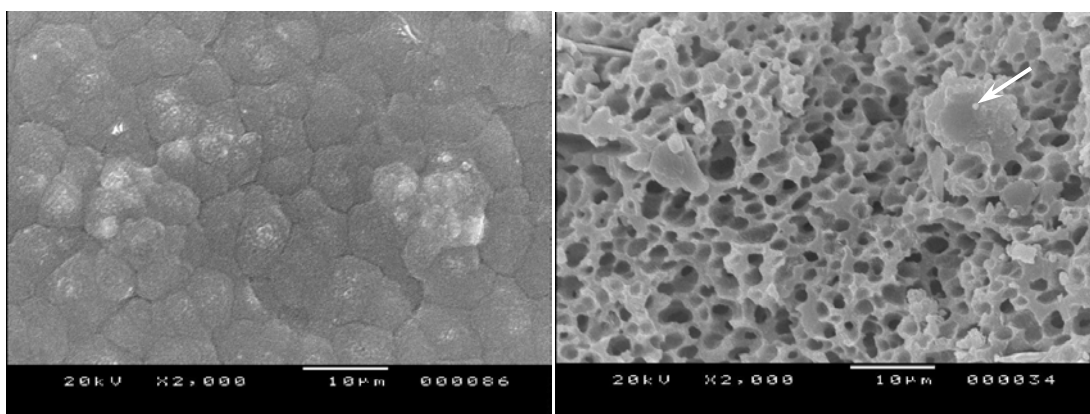
Figure 3.35 SEM images of the planar (left) and cross-section (right) of the
PVDF/0.08 nano-Cu with 0.05%Brij displaying a fine particle (arrow).
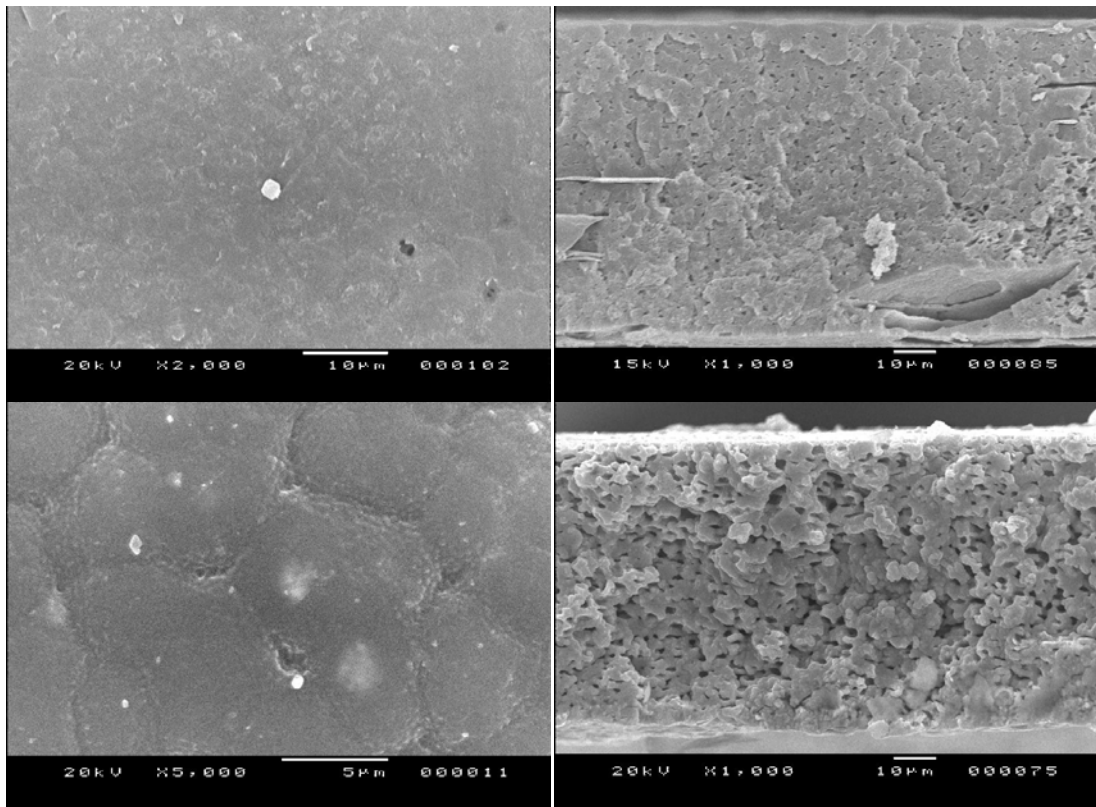
Figure 3.36 Comparison of SEM images of the planar (left) and cross-section (right) of the PVDF/0.05%Brij/0.02 Cu of (a) 3 μm and (b) < 50 nm particle size.

3.3.2 Electrical Properties of the Neat PVDF and Composites

For the two-phase composites, their properties related to the numbers of the phases, the volume fraction and the properties of an individual phase and by the way in which different phase are interconnected. An amount of formulas for the determination of the permittivity such as Maxwell Garnett (MG), Maxwell-Wagner (MW), Bruggeman (BG), Hanai-Bruggeman (HBG) are a formula for such a fundamental two phase composite. The model for describing the three phase system has been proposed by Pearce *et al*., in 1973. However, Hanai found that the result for complex permittivities (ε_c) was the same as that for real permittivities (ε_c') or conductivities (σ), specifically for a two-phase mixture as described by equation (3.3) :

$$\frac{\varepsilon_c\text{-}\varepsilon_m}{\varepsilon_p\text{-}\varepsilon_m}\left(\frac{\varepsilon_p'}{\varepsilon_c}\right)^{1/3}=1\text{-}\emptyset \qquad (3.3)$$

where $\emptyset$ is the volume fraction of the metal phase, ε_m and ε_p are the complex permittivity of the metal and polymer in which dispersed, respectively, and ε_c is the complex permittivity of composite.

The studies were made on the copper filler of 3 µm and 50 nm in diameter. The volume conductivity equation:

$$\gamma=\frac{t}{A}G \qquad (3.4)$$

Where t is the film thickness (m), A is the effective film area (m^2) and G is the electrical conductivity (S) was used and the values were listed as showed in Table 1. The permittivity of the material derived from the fact that the PVDF is electroactive material. This means that the polymer can be polarized in an electric field and functioned controllably by means of applying appropriate voltage. The equation relating to the permittivity of the polymer is the equation (3.5)

$$\varepsilon_r = \frac{tC}{\varepsilon_0 A} \qquad (3.5)$$

While ε_r is the relative permittivity, C is the electric capacitance (F), ε_0 is the permittivity of free space (8.854×10^{-12} F·m^{-1}).

From Table 3.2, the polymer permittivity increased with the surfactant concentration and decreased with frequency. Because the pores were filled with air and acted as the air bubbles connected through the polymer content. It is considered that the PVDF with 0.05%Brij is the most attractive for it has relatively high permittivity and the copper filler was thoroughly solvable.

Table 3.2 The degree of crystallinity, permittivity, dissipation factor and volume conductivity of the neat PVDF and PVDF with Brij at various contents.

Surfactant (%)	Crystallinity (%)	Relative Permittivity		Dissipation Factor		Volume Conductivity (µS/m)	
		1 kHz	1MHz	1 kHz	1MHz	1 kHz	1MHz
0.00 Brij	39.70	4.94	2.88	0.01	0.05	0.004	79.63
0.01 Brij	39.65	6.65	4.35	0.01	0.07	0.043	17.70
0.05 Brij	22.40	18.70	2.03	1.07	0.19	1.150	22.00
0.10 Brij	-	20.10	1.88	1.32	0.25	1.480	25.70

Figure 3.37 shows the dielectric constant of samples decrease substantially as the frequency was increased whereas the dielectric loss increase following to the frequency. This result may be because the effect of polarization is to reduce the field inside the medium. Moreover, it was clearly shown that the low viscosity sample (10:90PVDF) had higher dielectric constant than that of the high viscosity sample (20:80PVDF). Thus, this work is interested in properties of the low viscosity PVDF sample which would denote as neat PVDF.
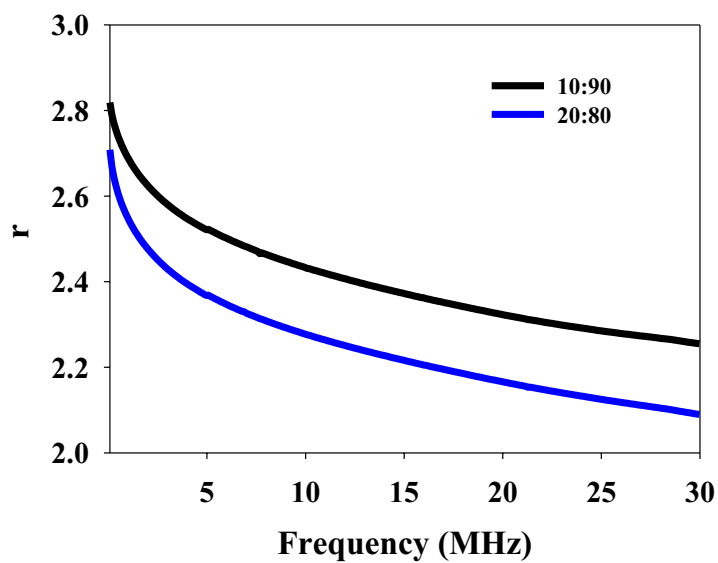
(a)
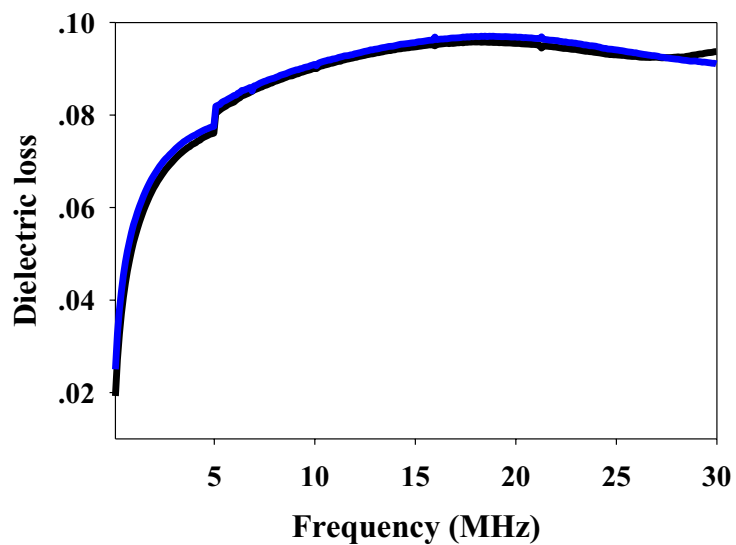
(b)

Figure 3.37 Dependence of dielectric constant and dielectric loss as function of frequency of PVDF film at 2 different PVDF:NMP ratios.

3.3.2.1 Effect of Copper Particle Micro-size

The variation of dielectric constant, dielectric loss and volume conductivity with frequency for investigating composition displayed in Figure 3.38. It was clearly shown that the dielectric constant depend strong on the content of copper filler and trend to decrease upon on the frequency while the dielectric loss of PVDF/0.2Cu trended to decrease at low frequency (< 1 Hz) refer to the behavior of copper (Figure 3.38(b)) and increased following the frequency at about 1 MHz referring to the behavior of PVDF medium (Figure 3.38(c)). The result from Figure 3.44 could be explained in that a maximum in dielectric loss at a certain frequency can be observed when dielectric constant has a minimum value i.e. a minimum stored energy at that frequency. Another explanation of the occurrence of peaks in the variation of dielectric loss with frequency can be observed when the hopping frequency is approximately equal to that of the externally applied electric field; i.e. it means resonance phenomena. As painted out by Iwavchi (1960) and Mazen (2003). The condition for observing a maximum in dielectric loss of a dielectric material is given by the relaxation (Reddy and Reddy, 1991). The dielectric constant and the dielectric loss decrease with increasing frequency for almost all PVDF composite samples. This behavior of a dielectric is explained qualitatively in terms of the supposition that the mechanism of the polarization process electronic polarization.

Referring to the conductivity figure (σ vs f) it can be seen that for the applied frequency $f > f_{max}$ the conductivity seems to be not affected by the applied external field. This means that the applied frequency is higher than the jump frequency (f_{max}) and thus it does not affected the hopping conduction mechanism i.e. for $f > f_{max}$ the applied field obstruct the hopping mechanism and consequently the conductivity decreases with increasing frequency. It can be concluded that for $f > f_{max}$ the applied field accelerates the charge carriers and the conductivity increases (Figure 3.38 (d)).
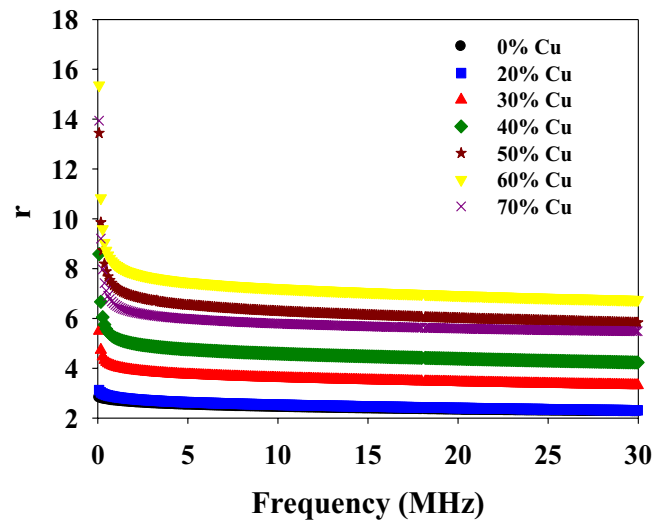
(a)
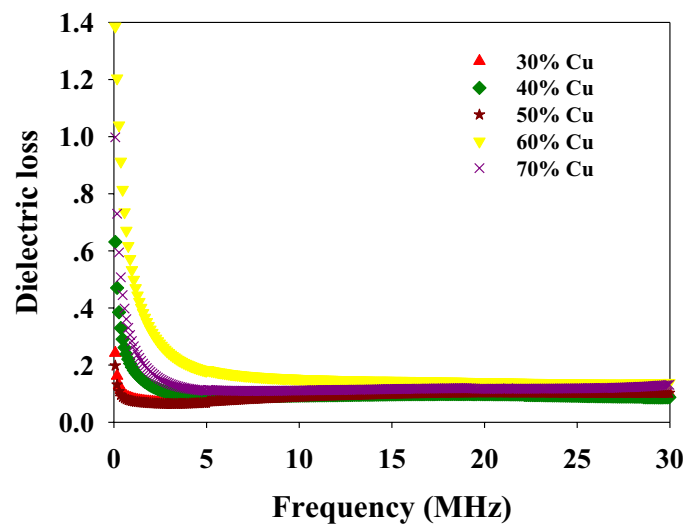
(b)

Figure 3.38 Dependence of (a) dielectric constant of neat PVDF and their composites, dielectric loss of (b) neat PVDF and PVDF/0.2Cu (c) PVDF composites, and (d) volume conductivity of neat PVDF and PVDF/0.6 micro Cu as function of frequency.
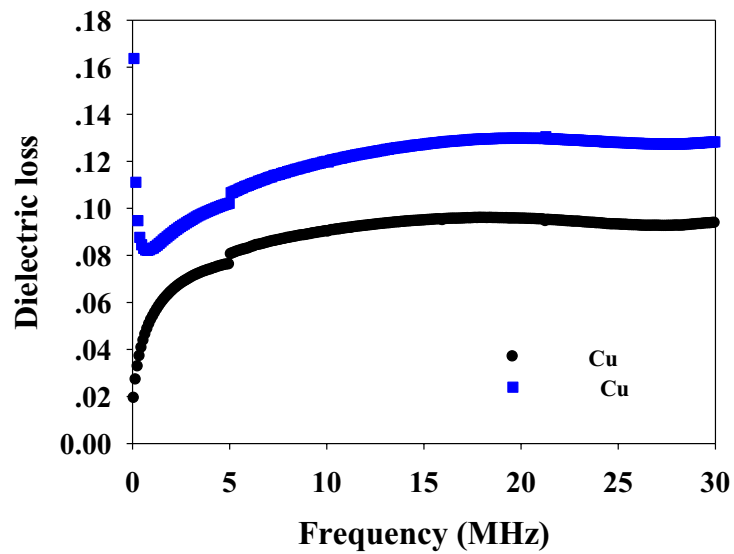
(c)
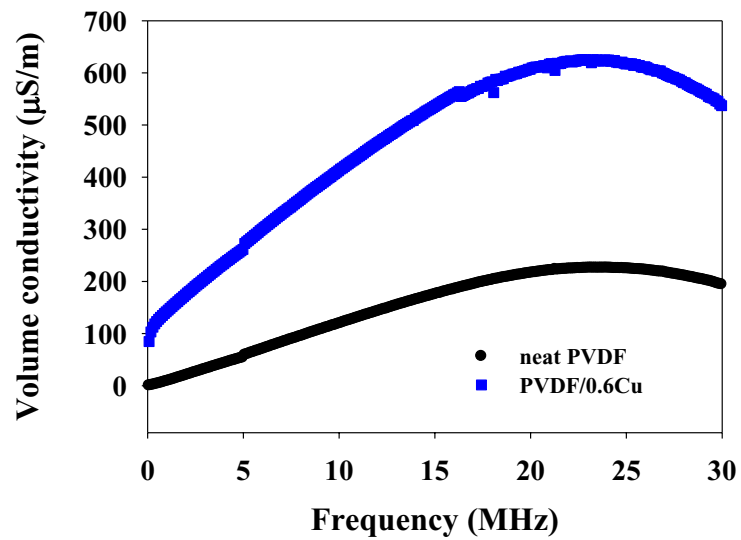
(d)

Figure 3.38 (continued) Dependence of (a) dielectric constant of neat PVDF and their composites, dielectric loss of (b) neat PVDF and PVDF/0.2Cu (c) PVDF composites, and (d) volume conductivity of neat PVDF and PVDF/0.6 micro Cu as function of frequency.

Figures 3.39 shows the effect of the volume fraction of the copper filler inclusion on the dielectric constant of composites. Dependence of the dielectric constant on the concentration of copper can be divided in to three stage; I, II, and III. First, the dielectric constant rises gradually with the increasing copper contents in the composites, because the microcapacitance structure was formed. The percolation threshold was visible, at a volume concentration of about 0.6, where the dielectric constant abruptly increased. The reason for the significant dielectric constant was ascribed to a whole conductive network form eventually in the composite when the volume fraction of the copper filler increased to the threshold. Additionally, the dielectric constant of a material was a function of its capacitor, which was also proportional to the quantity of charge stored on either surface of the sample under an applied electric field. At this stage, the conduction behavior of composites was also controlled by the concentration of conducting phase. At the final stage, the dielectric constant decreased due to significant conductive network formation, as seen in Figure 3.33 (SEM). The conductive network makes the composite become the conducting material and this leads to a high leakage current in the composite, so the dielectric constant decrease (Xu *et al*., 2007; Dang *et al*., 2007; Yao *et al*., 2007; Wang and Dang, 2005). The conductivity measured clearly demonstrates a conductor-insulator translation at   0.2-0.6. When volume fraction of copper was larger than the percolation, more and more cluster connect to the infinite one and the size of the isolated cluster decreases.
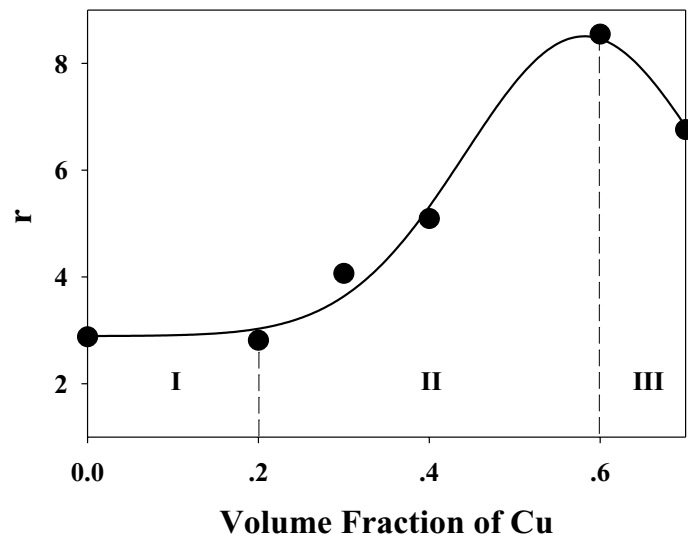
(a)
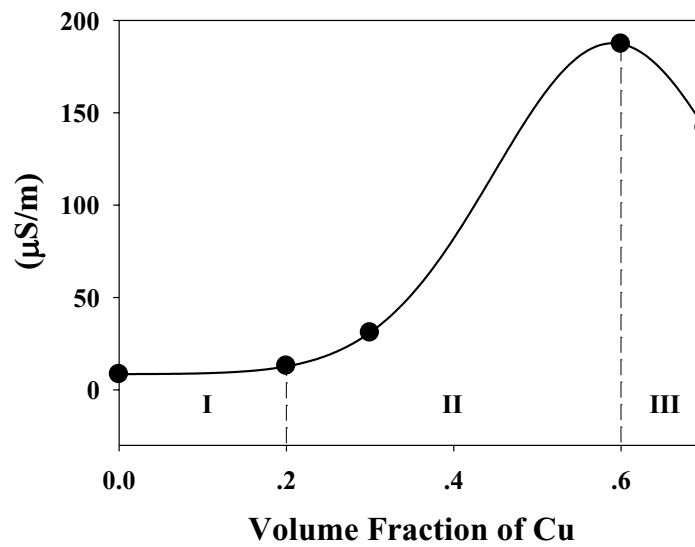
(b)

Figure 3.39 Variations of the (a) relative permittivity and (b) volume conductivity of the PVDF/0.05%Brij-30 filled with micro-Cu with various volume fraction measured at 1 kHz.

3.3.2.2 Effect of Copper Particle Nano-size

Figure 3.40 shows that relative permittivity and volume conductivity of PVDF composite were greatly enhanced by adding Cu nano-particles into the polymer matrix which correspond to the report of Kobayashi (2008). At high copper filler loading and adding surfactant, however, copper-particle-filled polymers lose their flexibility and low quality composites were obtained. Therefore, the study of temperature effects on electrical properties of neat PVDF and its composite will evaluate the copper nano-size at low filler content.

Temperature dependence of the dielectric constant for the neat PVDF and its composite which were coated with gold electrode was shown in Figures 3.41-3.43. The composites demonstrated a good thermal stability at high frequency above 100 kHz. However, the dielectric constant increased with temperature at 100Hz, 1 kHz and 10 kHz. Particularly, at 100 Hz, the dielectric constant increase from 5 to 7 for neat PVDF and 30 to 75 for PVDF/0.06Cu-nao when the temperature changes from 25 to 120 $^{\circ}$C. These results are due to the fact that the PVDF and its composite becomes a flexible state as a result in the movement of molecules was improved when the temperature was increased. Therefore, the molecules had enough time for polarization at low frequency. At high frequency, however, the polarization of molecules did not have enough time to catch up with the change in electrical field frequency, which leads to the weak dependence of dielectric constant on temperature.

Not only electrical properties were characterized via the determination of dielectric and dielectric loss but the relaxation behavior of neat PVDF and its composite also evaluated. It is well known that the relaxation behavior of PVDF was greatly dependent on its crystalline morphology. The PVDF film exhibits three main dielectric relaxations designated as $_c,$ $_a$ and in order of decreasing temperature at a constant frequency. The   and $_a$ relaxations were considered to occur in the amorphous regions and the molecular motions involved are local mode molecular motion and micro- Brownian motion of main chain segments, respectively. The $_c$ relaxation is considered to arise from molecular motions in the crystalline regions of PVDF.

Figure 3.47(a) shows the temperature dependence of the dielectric constant measured and Figure 3.47(b) shows the temperature dependence of the dielectric loss for the neat PVDF. The dielectric constant ($_r$) was observed to increase with temperature and this increase is more appreciable at lower frequencies. The dielectric loss increases slowly with temperature for lower frequencies and increase sharply in the frequency at high frequencies. The increase of dielectric with temperature is due to an increase of the total polarization, and is in agreement with the temperature dependence of polar dielectrics in general. The loss maximum would occur at still lower temperatures. This dielectric absorption is, broadly, in the region of $_a$ relaxation of -phase PVDF samples. Nakagawa and Ishida (1973) found that the crystal structure of -phase holds locally even in the amorphous regions. It appears that the $_a$ relaxation of PVDF may depend on its crystal structure. However, due to the limitations of our experimental range of temperature and frequency, complete $_a$ relaxation has not been observed, prohibiting any further analysis. The small loss peak in Figure 3.41(b) could be due to a relaxation process. Considering the relative position of this peak on the temperature scale among other relaxations of PVDF (Lovinger, 1982), it could be the relaxation arising from molecular motions in the folds on the surface of the crystallites. This relaxation was first observed by Kakutani (1970) in the dynamic mechanical relaxation spectra of -phase and -phase samples, but not in the dielectric relaxation spectra. The low-frequency dispersion of $_c$ could now be attributed to trapped charge carriers. Ionic impurities have been observed to get deposited near the electrodes (at very high temperatures) or trapped at the crystalline-amorphous interfaces, leading to large losses at low frequencies in PVDF composite samples as showed in Figures 3.42-3.43 (Osaki *et al*., 1971; Jonscher, 1983; Gross *et al*., 1985; Dasgupta *et al*., 1980.)
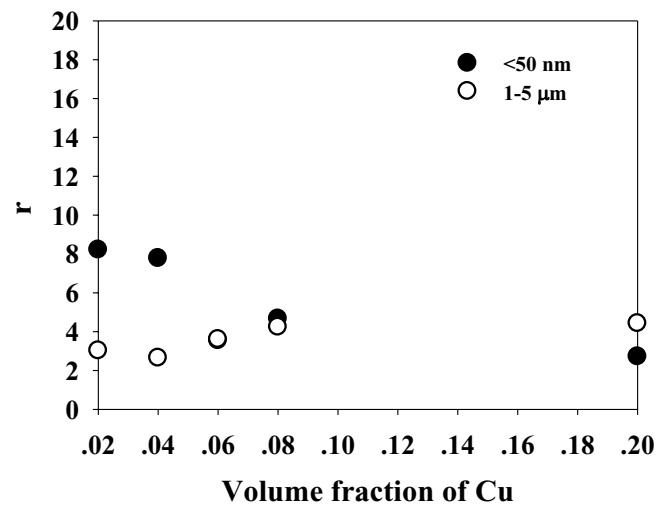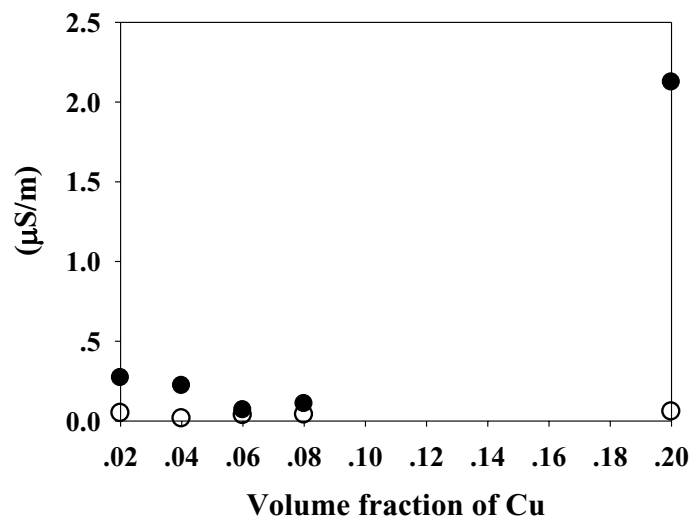
Figure 3.40 Variations of the (a) relative permittivity and (b) volume conductivity
with volume fraction of micro or nano-Cu dispersed in the PVDF/0.05Brij-30
measured at 1 kHz.
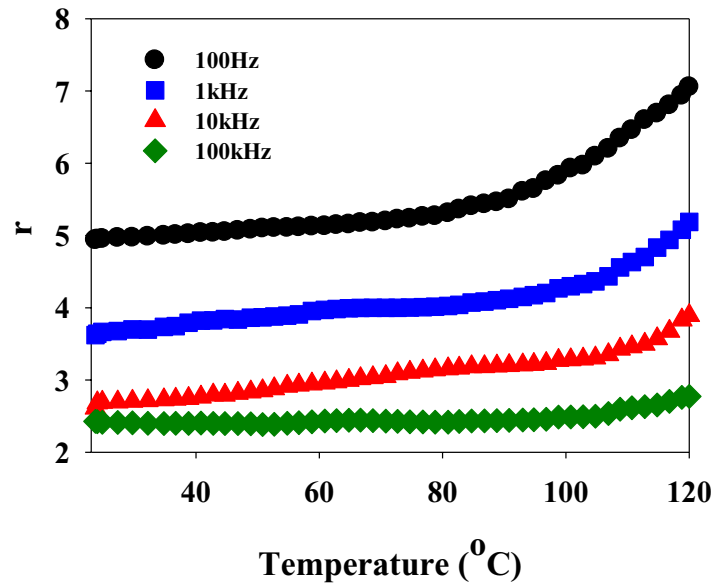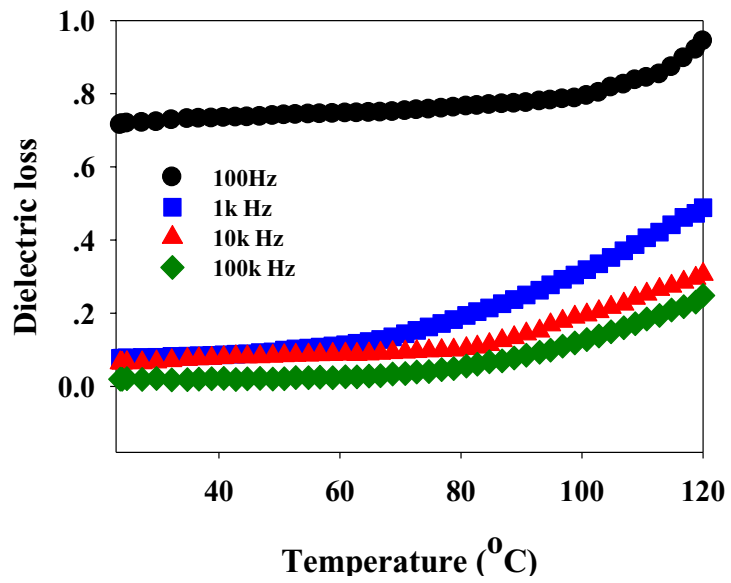
Figure 3.41 Temperature dependence of the dielectric parameters
(a) dielectric constant and (b) dielectric loss measured for the neat PVDF.
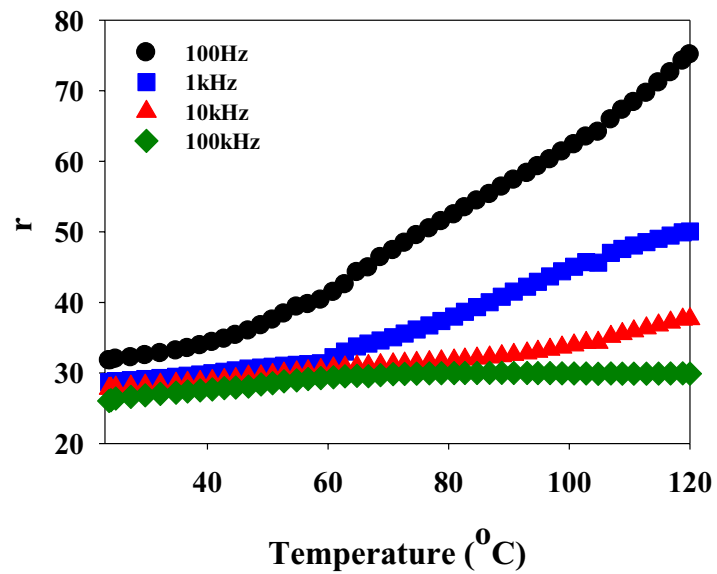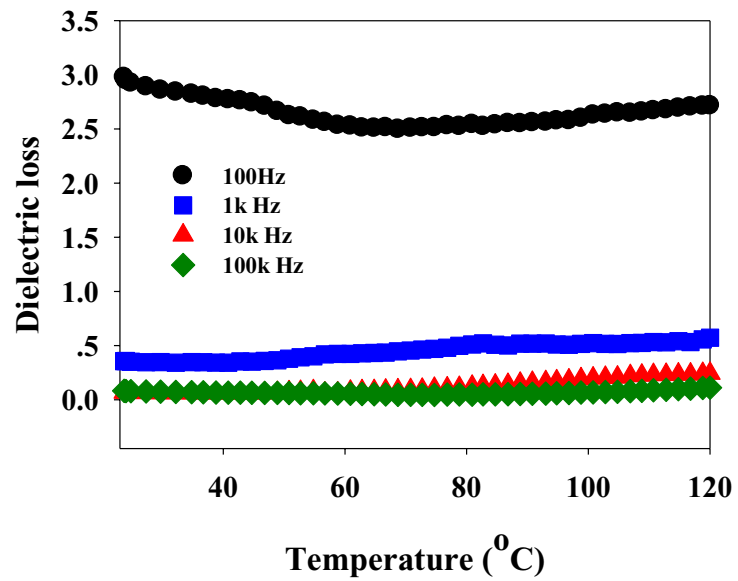
Figure 3.42 Temperature dependence of the dielectric parameters
(a) dielectric constant and (b) dielectric loss measured PVDF 0.02 nano-Cu.
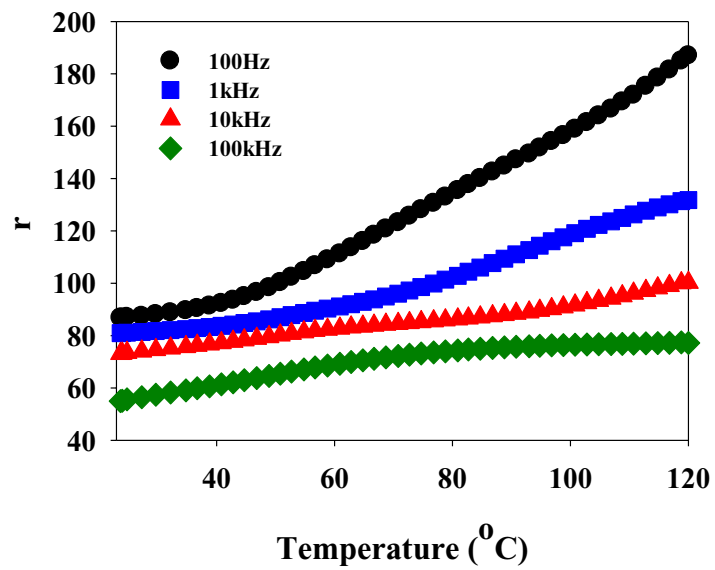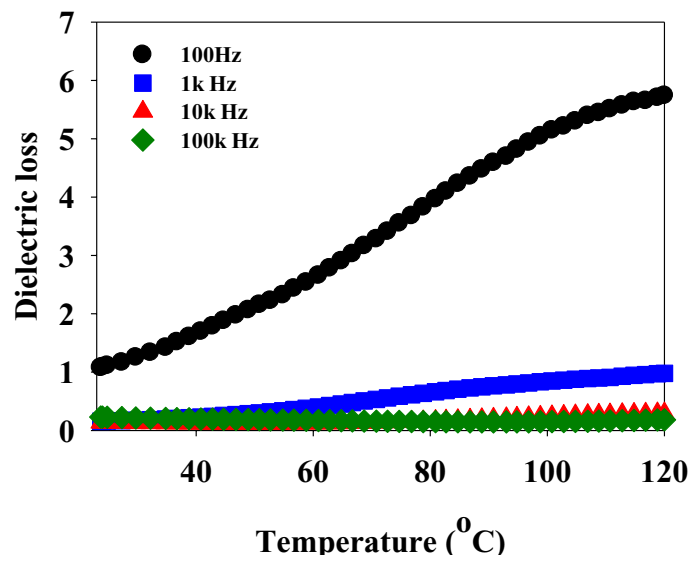
Figure 3.43 Temperature dependence of the dielectric parameters
(a) dielectric constant and (b) dielectric loss measured PVDF 0.08 nano-Cu.

Figures 3.44-3.46 demonstrates the variation of copper composition on capacitance dielectric constant and dielectric loss as function of temperature. The PVDF adding with nano-copper filler as high as 4% exhibited the capacitance more than 0.5 nF which can be used in energy harvesting application (Figure 3.44). The dielectric constant can be raised to 4-10 times for PVDF composites. Unfortunately, high loss of PVDF composite for the content of copper more than 4% lead to high leakage resistance of piezoelectric energy harvester (PVDF composites) which was not appropriate for using in an energy harvesting system.
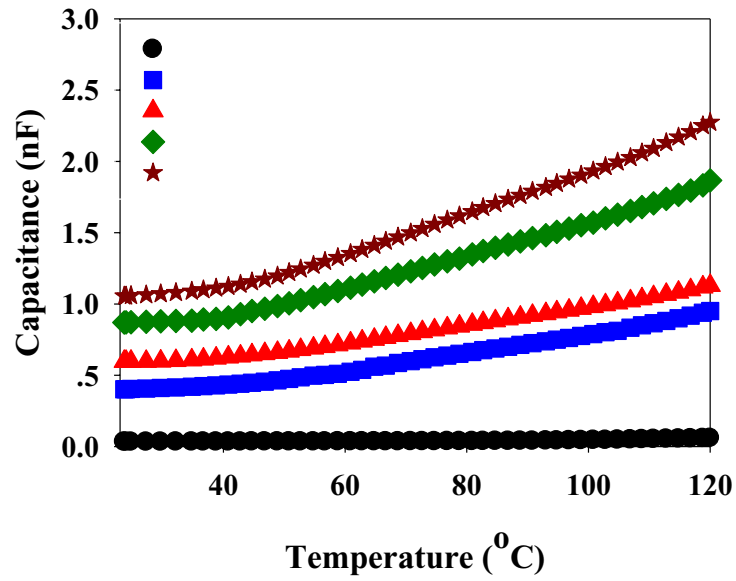
(a)
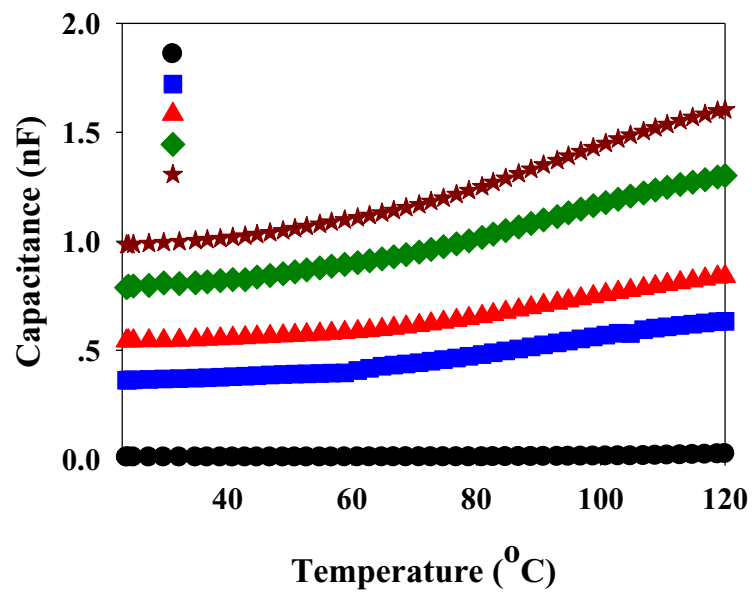
(b)

Figure 3.44 Capacitance of neat PVDF and their composites measured at
(a) 100 Hz and (b) 1 kHz.
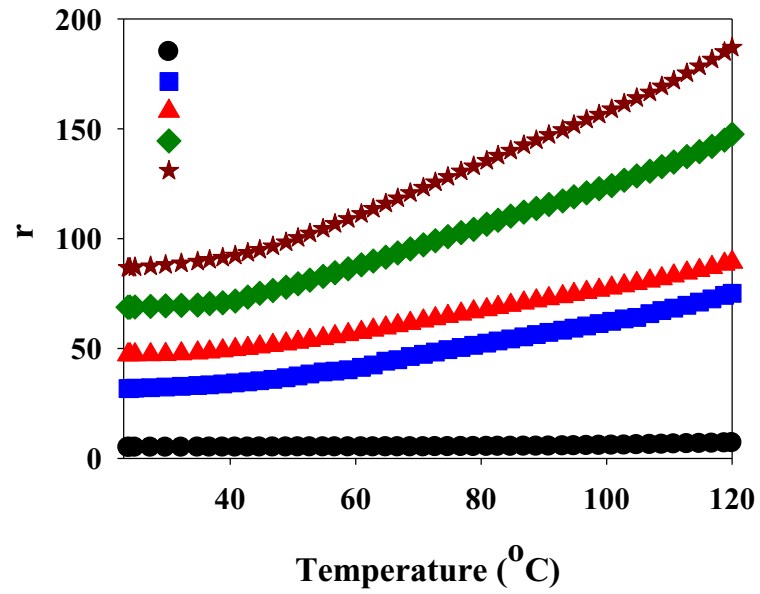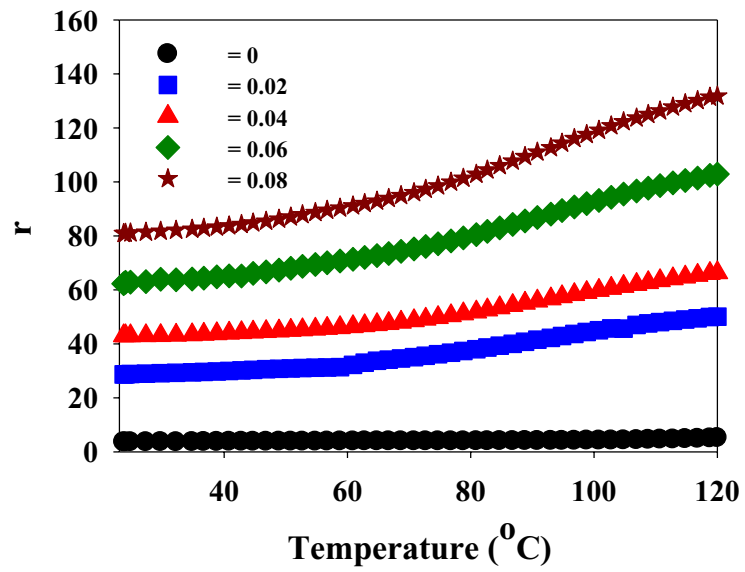
Figure 3.45 Dielectric constant of neat PVDF and their composites measured at
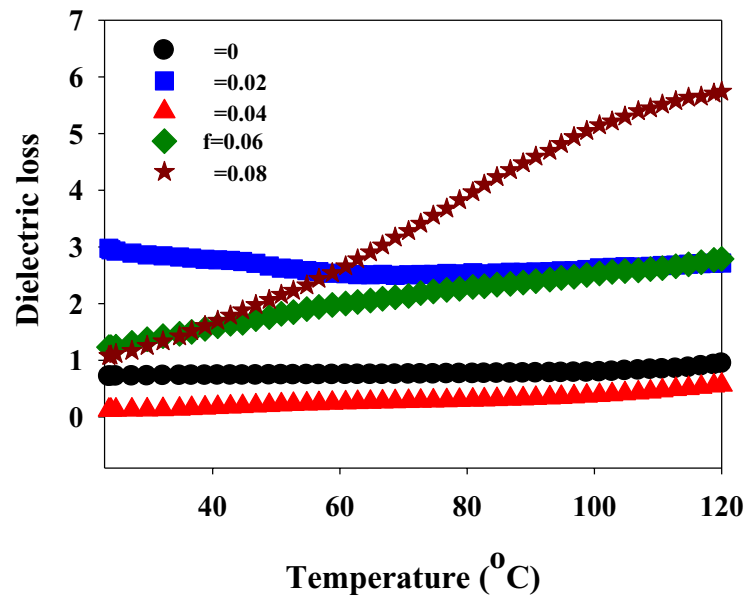
(a) 100 Hz and (b) 1 kHz.

(a)
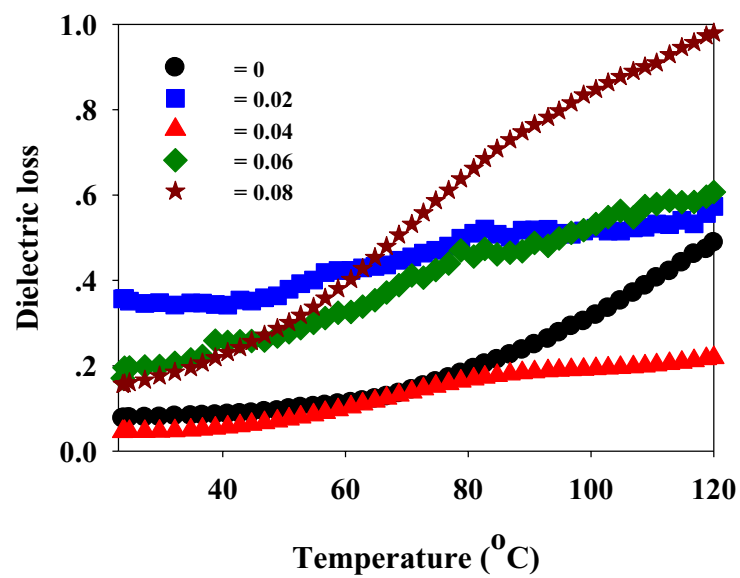
(b)

Figure 3.46 Dielectric loss of neat PVDF and their composites measured at

(a) 100 Hz and (b) 1 kHz.

3.4 Conclusions

This work shows that the electroactive PVDF can be synthesized for a wide range of micro- and nano-loadings. The content of the filler can be largely varied due to the surfactant. In turn, the properties of the composites are strongly depended on the filler content. The PVDF composites prepared in this work are suitable for MEM applications where some problems related to the piezoceramic deposited on silicon would no longer exist. From the investigations, it implies that the composites with high content of the fillers which are highly conductive are suitable for applications in transducers and sensors while the low-loaded ones are promising for certain applications such as energy harvesting which will be described in details in Chapter 5.

CHAPTER 4

BACKGROUND ON VIBRATION ENERGY HARVESTING AND VALIDATIONS ON PIEZOCERAMICS

This chapter has a twofold purpose. First, the background on energy harvesting, converting an ambient vibration into an electrical energy is presented. Hence, two well-known approaches, i.e., standard and nonlinear are mainly described. Second, the first investigation of ability in energy harvesting of two piezoceramics, PZT+1mol%Mn and PMN-25PT, is reported in comparison when using different approaches mentioned above. The benefit obtained from this chapter is devoted to the first study on piezoelectric PVDF energy harvester separately reported in Chapter 5.

4.1 Introduction

The research in vibration-based energy harvesting has highly gained great attention in the past decade. It brings the possibility in powering portable electronic devices including wireless sensors by using the vibration energy available in the ambient environment. Accompanying the ultra-low power requirement is the reduction in size of electronic components and their host structure. The lifetime of the functional devices can also be extended as long as mechanical inputs exist. It is now possible to replace the batteries in factories, buildings and unarm vechicles or weapons.

The basic of vibration-to-electric energy conversion mechanisms can be divided into three type; electromagnetic, electrostatic, and piezoelectric transductions (Arnold, 2007; Glynne-Jones *et al*., 2004; Jeon *et al*., 2005; Mitcheson, 2004; Roundy *et al*., 2002; Roundy *et al*., 2003; Sodano *et al*., 2005; Williams and Yates, 1996). The fundamental concepts presented in this chapter involve mainly the mechanics of piezoelectric vibrating structures, the constitutive behavior of piezoelectric materials and the electrical circuit theory.

4.2 Lamp Model and Governing Equations for a Vibrating System

In the application, the piezoelectric element is coupled to a host structure. A simple representative model (near resonances) of such a system is a simple second-order mass-spring-damper electromechanically coupled as shown in Figure 4.1. The behaviour of the system can be described by the following equations:

$$M\ddot{u}+C\dot{u}+K_E u=F-\alpha V \tag{4.1}$$

$$I =\alpha\dot{u}-C_o\dot{V} \tag{4.2}$$

$$K_D=K_E+\frac{\alpha^2}{C_o} \tag{4.3}$$

$$k^2=1-\frac{K_E}{K_D}=\frac{\alpha^2}{C_o K_D}=\frac{\alpha^2}{C_0 K_E+\alpha^2} \tag{4.4}$$

Where u, F, V and I respectively represent the beam displacement, the force applied, the voltage and the outward current of the active element. The other parameters; M, C and K_E are defined as the dynamics mass, structural damping and stiffness short circuit, respectively.   and C_0 are the force factor and the blocking capacitance of the piezoelectric. It also defines the open circuit stiffness K_D, whose expression is given in equation (4.3). From these equations, the expression of the coupling coefficient of the overall structure is given by the relationship (4.4), from the expression of coupling value as the function of mechanical resonance frequency of both open and short circuit, it is

$$k^2\approx \frac{f_D^2-f_E^2}{f_D^2} \tag{4.5}$$
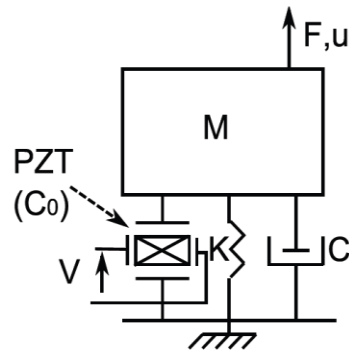
Figure 4.1 Modelling the mass-spring-damper an electromechanical system
(Guyomar *et al.*, 2009).

This model is sufficient for both vibration control development (force leads to significant displacement) and energy harvesting development. According to the model in Figure 4.1 and equation (4.6), the energy balance equation is:

$$\frac{1}{2}M[\dot{u}^2]_{t_0}^{t_0+\tau}+ C\int_{t_0}^{t_0+\tau}\dot{u}^2dt+ \frac{1}{2}K_E[u^2]_{t_0}^{t_0+\tau}= \int_{t_0}^{t_0+\tau}F\dot{u}dt - \alpha\int_{t_0}^{t_0+\tau}V\dot{u}dt \qquad (4.6)$$

The first term and other two terms on the left are kinetic energy, the mechanical losses and the transferred energy, respectively. The right term comprises of the mechanical energy and the transferred energy. The transferred energy is the sum of the electrostatic energy stored on the piezoelectric element and the absorbed (harvested) energy in the connected circuit and is expressed by:

$$\alpha\int_{t_0}^{t_0+\tau}V\dot{u}dt= \frac{1}{2}C_0[V^2]_{t_0}^{t_0+\tau}+ \int_{t_0}^{t_0+\tau}VIdt \qquad (4.7)$$

The first term on the right side is the electrostatic energy stored in the piezoelement. The second one on the same side is the energy exchanged with the circuit. It can be seen in the expression that the V value plays important role in the energy conversion.

The vibration control earlier mentioned is focused within the resonance frequency bands. In general, vibration theory is concerned with the oscillation motion

of the system which may be harmonic, periodic or general (amplitude vary with time). Vibration can be classified as free or forced vibration. The system without external force act on the system refers to the free vibration while the force vibration is the system which is acted by external excitation. Both cases of vibration system have to capable of producing restoring forces which tend to maintain the oscillatory motion. These restoring forces can be produce by discrete element such as linear spring or by continuous structural elements such as beam. The restoring force produced by the elastic element is proportional to the deflection or elastic deformation. If the vibration is small, it is customary to assume that the force-deflection relationship is linear, that is, the force is equal to the deflection multiplied by proportionality constant. In this case the linear theory of vibration can be applied. If the assumption of the linear theory of vibration are not valid such the displacement-force relationship cannot be described using linear equation, the nonlinear theory of vibration have to apply (Shabana, 1996).

The level of vibration is significantly influenced by the amount of energy dissipation as a result of structural damping of the material, however, vibration may occur without damping. Additionally, vibration is the result of the combined effects of the inertia and elastic forces. Inertia of moving part can be expressed in terms of the mass, moment of inertia, and the time derivative of the displacements. Elastic restoring forces can be expressed in term of displacement and stiffness of the elastic members.

Not only vibration parameters but also the mechanical parameters affect to the output electric power. Mechanical energy will be converted into electrical energy through the direct piezoelectric effect. Voltage induced in the piezoelement can be specified into one of these modes: d_{31} and d_{33} (Jeon $et\ al.$, 2005). The first is explained by equation 4.8 while the latter is by equation 4.9.

$$V_{31} = g_{31}t \tag{4.8}$$

$$V_{33} = Lg_{33} \tag{4.9}$$

with
$$g \quad \frac{d}{_{0\ \ r}} \tag{4.10}$$

Where   is the applied stress, g is piezoelectric voltage constant which is related to the piezoelectric charge constant d, dielectric constant in vacuum ε_0 and relative dielectric constant ε_r.

The output electric power P of the harvesting structure can be evaluated by the so-called Figure of merit or FOM :

$$P \propto g \cdot d \tag{4.11}$$

The product in equation 4.11 is often referred to energy density.

4.3 Nonlinear Vibration of a Cantilever Beam

There are four main types of piezoelectric vibration structure: stack, plate, flag and fiber, and cantilever beam. Cantilever beam is, however, the fundamental feature of a piezoelectric energy conversion system. For a very restrictive domain such as the trivial vibration amplitude, a linear model is used. In most cases, the nonlinear vibration is required in order to accurately identify the dynamic behavior and is presented in this section. In structural mechanics, nonlinear vibration can be divided into 6 categories; (1) damping is essentially a nonlinear phenomenon, (2) Geometric nonlinearity exists in system undergo, a large deformation or deflection, (3) Inertia nonlinearity derives from nonlinear terms containing velocity and acceleration in the equation of motion, (4) material nonlinearity refers to the nonlinear of stress and strain, (5) nonlinear appear in the boundary condition is called as nonlinear boundary and (6) other types of nonlinearity such as nonlinear in system with impact, backlash or play in their joins (Malatkar, 2008).

The most popular structure due to its simplicity is a vibrating beam with a piezoelectric element bonded close to clamped end (minimum radius bending) as depicted in Figure 4.2. The poling direction is perpendicular to the beam, a driving force, F, is applied to the free end of the beam while the electrical circuit is connected to the piezoelectric element. The simple model of structure acts as a pure Euler-Bernoulli beam and strain along the z-axis is zero (2D plane strain). Additionally, this

work focus on the fist flexural mode of deformed shape because its deformed shape approximately equal to its shape when a static force is applied at the free end of the beam. The important parameter on vibration of the beam is the dynamic mass (M) which can be calculated from equation (4.12) (Badel *et al.*, 2007).

$$M= \frac{\int_0^L m_x u_y^2}{u_{yl}^2} dx \tag{4.12}$$

with

$$m_x = b e_B \quad \text{for } x \quad [0, x_P[U]x_P + L_P, L]$$

$$m_x = b(e_B + 2e_P) \quad \text{for } x \quad [x_P, x_P + L_P] \tag{4.13}$$

where m_x, u_y, and u_{yl} are the linear density of the structure along the x-axis, displacement of each piece along the y-axis and displacement of the beam's free end, respectively. The mechanical losses are represented by the internal (strain rate) and external (viscous air) damping mechanisms. The piezoelectric material and substructure layers are assumed to be perfectly bonded to each other. The electrodes covering the opposite faces of the piezoelectric material layers are assumed to be very thin so that their contribution to the thickness dimension is negligible (Erturk and Inman, 2009).
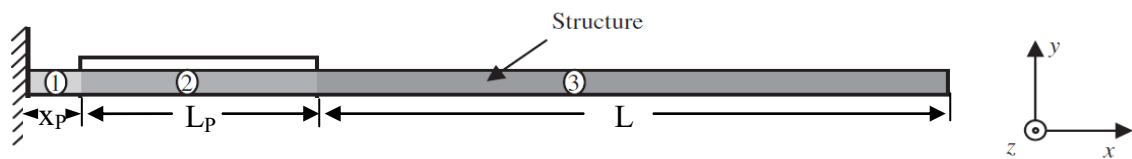
Figure 4.2 The cantilever beam with bonded piezoelement, revealing the length from its fixed end to the piezoelement (x_P), length of the piezoelement (L_P) and the length from the piezoelement to the free end of the beam (Badel *et al.*, 2007).

Figure 4.3 shows the optimization of the coupling coefficient depends on the mechanical energy transfer between the host structure and piezoelectric insert. Therefore, the mechanical energy transfer depends on the dimension (area and thickness) of both cantilever beam and piezoelectric material.
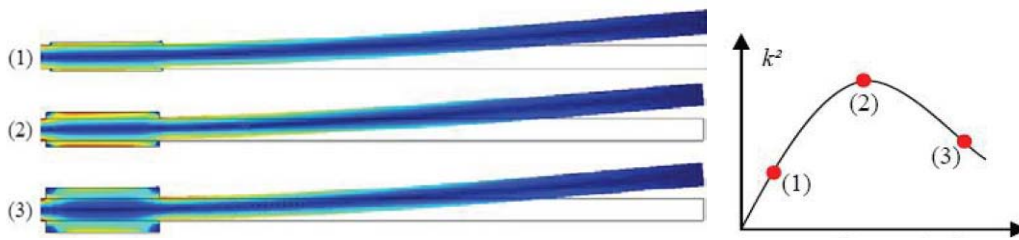
Figure 4.3 Global electromechanical coupling coefficient for different thicknesses of a piezoelectric element. (Badel *et al*., 2005).

Figure 4.4 shows the energy response as function of the bending of the cantilever beam. For example, when the voltage across the piezoelectric element reached a maximum (resp. minimum), energy is recovered by a closing switch. At the end of the recovery process, voltage cell is zero, and the energy injection phase can start. When the previous recovery phase was initiated on a positive voltage (resp. negative) must therefore provide an initial voltage negative (resp. positive), which is made by closing another switch. The piezoelectric element is then left as an open circuit until the next stage.
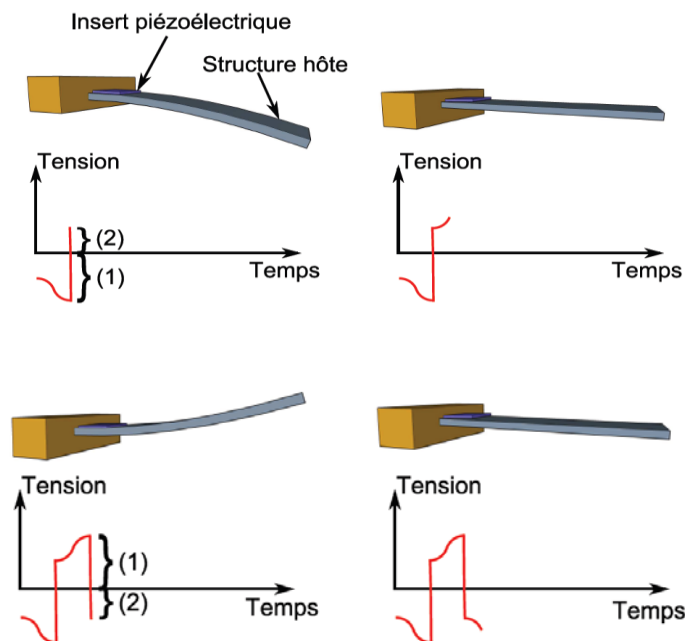
Figure 4.4 Transactions of the recovery by re-injection of energy (Lallart, 2008).

4.4 Approaches for Energy Conversion

4.4.1 Standard Technique

The simplest way for extracting energy from a piezoelectric material consists of directly connecting the electrodes of the active element to a smoothing capacitor and a load through a rectifier bridge (Figure 4.5(a)). In this case the energy harvesting process occurs when the absolute value of the piezovoltage equals the rectified voltage V_{DC} (Figure 4.5(b)). The remaining of the time, the piezoelectric insert is left in open circuit. Assuming that the storage/smoothing capacitor C_e is relatively large ($C_e \gg C_0$ and $R_L C_e \gg T/2$, with T the vibration period) so that the rectified voltage V_{DC} may be considered as constant, the harvested energy E_{stand} per harvesting cycle is then given by integrating the product of the current by the rectified voltage:

$$E_{stand} = \int_{t_1}^{t_2} V_{DC} I dt \tag{4.14}$$

with t_1 and t_2 the time instants when the conduction starts and stops respectively (the end of the conduction corresponds to the cancellation of the current, which actually occurs when the displacement is maximal). In this case, it can be shown that the expression of the power yields (Lefeuvre *et al.*, 2006):

$$P_{stand} = 4f_0 V_{DC}(\propto u_M - C_0 V_{DC}) \tag{4.15}$$

with f_0 the vibration frequency and u_M the displacement magnitude. However harvesting energy from an electromechanical structure leads to a decrease of the mechanical energy, and therefore induces damping effect, leading to the expression of the harvested power as a function of the input force (Lefeuvre *et al.*, 2006):

$$P_{stand} = \frac{16f_0^2 \propto^2 R_L}{(1+4f_0 R_L C_0)^2} \left[\frac{F_M}{2\pi C f_0 + \frac{16f_0 \alpha^2 R_L}{\pi(1+4f_0 R_L C_0)^2}} \right]^2 \tag{4.16}$$

whose maximum value as a function of the figure of merit given by the product of the squared coupling coefficient k^2 by the mechanical quality factor Q_M whose expression is given by:

$$k^2 Q_M = \frac{\alpha^2}{C_0 C} \sqrt{\frac{M}{K_E + \frac{\alpha^2}{C_0}}} \tag{4.17}$$

$$P_{stand}|_{max} = \begin{cases} \dfrac{k^2 Q_M}{\left(\pi + k^2 Q_M\right)^2} \dfrac{\pi}{2} \dfrac{F_M^2}{C} & \text{for } k^2 Q_M \leq \pi \\[4mm] \dfrac{F_M^2}{8C} & \text{for } k^2 Q_M \geq \pi \end{cases} \tag{4.18}$$

(a)

(b)
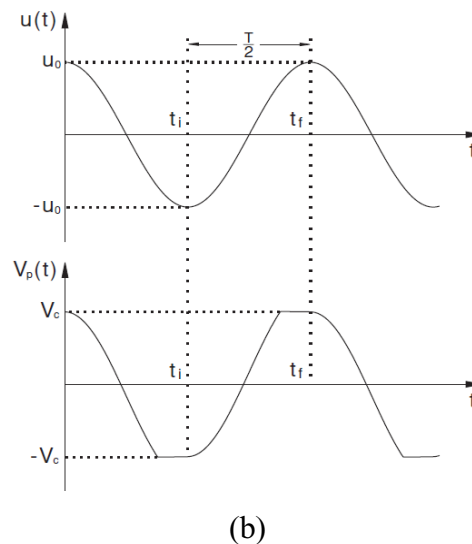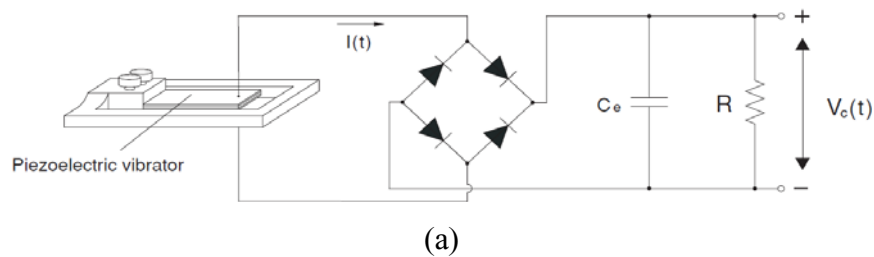
Figure 4.5 Standard energy harvesting interface: (a) schematics; (b) waveforms: (1) open circuit and (2) harvesting process (Shu and Lien, 2006).

4.4.2 *Synchronized Switch Harvesting on Inductor (SSHI) Technique*

The general principle for vibration control is known as the "Synchronized Switch Damping" (SSD) depicted in Figure 4.6 and can be divided into three categories; (1) control of structural damping coefficient, (2) control of the stiffness and (3) control of the dynamic mass. The former method is the most commonly used which does not change resonance, but strongly attenuates peaks. The latter two methods shift the resonance and also slightly change the factor mechanical quality.
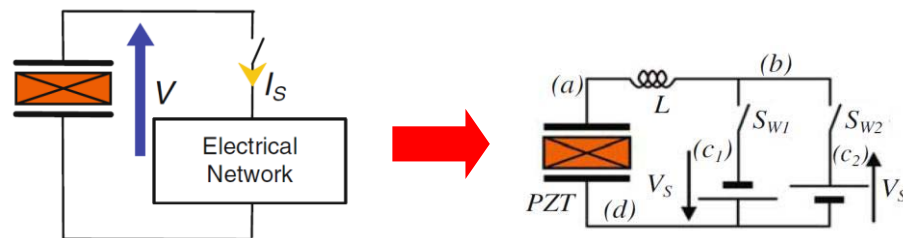
Figure 4.6 Schematic diagram of SSD technique **(**Guyomar *et al*., 2009)**.**

The basic technique of SSD is the piezoelectric element structure which converts vibration energy to an electrical circuit for a very short period of time. The switching time is synchronized with electrostatic energy available on the piezoelectric inserts. Specifically, piezoelectric element is almost always in open-circuit condition (as switching time is very concise) and charges available on the piezoelectric element are matched with the voltage and displacement, which happens when the voltage or displacement reaches an extremum (minimum or maximum). This means that S_{W1} is closed when the voltage or the displacement reaches a maximum and S_{W2} is closed when the voltage or the displacement reaches a minimum. The current flows trough (a) $\rightarrow$ (b) $\rightarrow$ (c_1) $\rightarrow$ (d) when S_{W1} is closed, and through (d) $\rightarrow$ (c_2) $\rightarrow$ (b) $\rightarrow$ (a) when S_{W2} is closed. If without the use of voltage source in the system, only one switch is needed for both minima and maxima.

The performance of SSD technique when compared to other technologies has a lot of advantages such as adaptable, robustness (except technical

SSDV), low energy cost (SSDI and SSDS techniques can even be self-powered), simplicity, integrability (no electronics impressive), no sensor needed (except for the method SSDVa), effectiveness of nonlinear structures. This is a reason behind why this SSD method further developed to use in energy harvesting which is presented as follows.

Even though the piezoelectric harvester is efficient to convert mechanical energy into electrical energy, however, the power output in many cases is too small (from a few microwatts to several hundred milliwatts) to power electric devices directly. Thereby, the accumulating and storing energy approach is also considered to develop self-powered systems such as the utilizing of a capacitor or rechargeable battery to accumulate energy. Moreover, the development of linear electric circuit technique and non-linear technique can increase the power output as high as 400% and 900%, respectively (Guyomar *et al.,* 2005; Lefeuvre *et al*., 2006a,b; and Badel *et al*., 2006a,b). The former technique developed electric circuits to store the generated charge or present it to the load circuit whereas the latter technique developed a new power flow optimization principle based on the technique so-called synchronized switch harvesting on inductor (SSHI).

The principles of the SSHI interface consists of adding in parallel with the piezoelectric element an inductor L (with an internal resistor r) in series with a digital switch S (Figure 4.7(a)) (Guyomar *et al*., 2005). The operation of the switching branch consists of connecting the piezoelement to the inductor when the displacement is either minimum or maximum. Due to the capacitive behavior of the piezoelectric element, this shapes an oscillating electrical network, and the voltage starts oscillating. In particular, if the switching time period is chosen such that the electrical oscillation lasts half a pseudo-period, this leads to an imperfect voltage inversion, characterized by the inversion coefficient defined as:

$$\gamma = e^{-\frac{\pi}{2Q_i}} \tag{4.19}$$

With Q_i the electrical quality factor of the inversion circuit $\left(Q_i = \sqrt{L}/\left(R\sqrt{C_0}\right)\right)$

Because of the cumulative effect of the voltage inversion, the switching process leads to a great increase of the voltage, as well as a reduction of the delay

between the voltage and the velocity (Figure 4.7(b)), denoting the magnification of the energy conversion abilities. The derivation of the power generated by the SSHI approach is very similar to the one performed for the standard interface. However, because of the voltage inversion, the initial conditions are changed, leading to the expression of the harvested power as a function of the driving force (Lefeuvre *et al.*, 2006):

$$P_{SSHI} = \frac{16\alpha^2 f_0^2 R_L}{(1+2(1-\gamma)f_0 R_L C_0)^2} \left(\frac{F_M}{2\pi C f_0 + \dfrac{16 f_0 \alpha^2 R_L (f_0 R_L C_0 (1-\gamma^2)+1)}{\pi\left(1+2 f_0 R_L C_0 (1-\gamma)\right)^2}} \right)^2 \tag{4.20}$$

whose maximal value can be approximated as a function of $k^2 Q_M$ by (Guyomar *et al.*, 2009):

$$P_{SSHI|_{max}} \approx \frac{k^2 Q_M}{\pi(1-\gamma)+8k^2 Q_M} \frac{F_M^2}{8C} \tag{4.21}$$

It can be shown from Equations (4.18) and (4.21) that the expression of this power limit is given by:

$$P_{lim} = \frac{F_M^2}{8C} \tag{4.22}$$
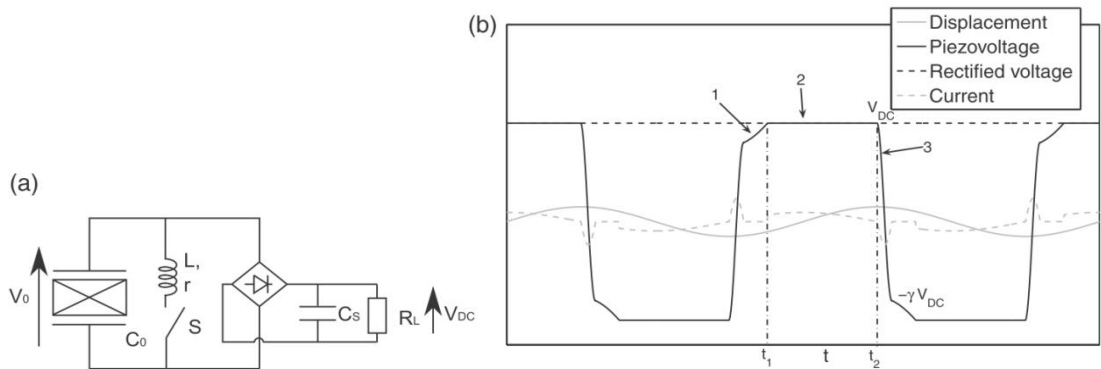
Figure 4.7 Parallel SSHI energy harvesting interface: (a) schematics; (b) waveforms: (1) open circuit ; (2) harvesting process ; (3) voltage inversion.

4.5 Energy Harvesting Validation on Piezoceramics

This section aims to illustrate and compare the output power generated from piezoelectric material between the nonlinear and standard techniques. Two compositions (PZT+1mol%Mn and PMN-25PT) obtained by sintering piezoelectric powders were chosen and highlighted the advantages and drawbacks of each of these.

The lead zirconate titanate or PZT ceramic which is most well known for various applications, including energy harvesting devices (Priya and Inman, 2005). A small amount of various acceptor dopants such as Mn are sometimes added during the fabrication process in order to enhance its piezoelectric properties. In this domain, it has been reported that the reduction of oxygen vacancy concentration and improvements in PZT fatigue and retention characteristics are obtained when small amount of Mn (< 1mol%) are doped into PZT, making the PZT+1mol%Mn a good trade-off for piezoelectric conversion (Zhang, 2004; Yadav and Sharma, 2008). Another composition of interest is the PT-doped PMN, as such a ceramic is a relaxor-based ferroelectric with excellent electromechanical coupling. Compared to PZT, the piezoelectric coefficient of such materials can be increased by a factor up to 3 in lateral mode and exceed 2000 pC·N^{-1} (Park *et al*., 1997; Suh *et al*., 2002). PT is interesting for use as dopant of PMN to adjust the Curie temperature (T_C) of the sample due to the fact that the polarization is disappearing over T_C. While it has been reported in previous works that the PMN-35PT ceramic exhibits the highest piezoelectric activity (Kelly *et al*., 1997), the presence of two phases in this composition (rhombohedral and tetragonal) may induce some instabilities in terms of temperature or stress (because of a possible phase transition), as well as a hysteretic behavior. Contrarily, PMN-25PT is purely rhombohedral, and, although having lower piezoelectric coefficients, is a good trade-off for realistic applications. The sintering of this composition is easier as well.

4.5.1 Material Aspects

4.5.1.1 Synthesis Procedure

For the investigation of vibration energy harvesting, the two common compositions discussed above were chosen: PZT with a Zr/Ti ratio of 52/48 with and without an introduction of 1mol %Mn and 1mol %F, and $0.75Pb(Mg_{1/3}Nb_{2/3})O_3$ with 10% and 25%PT (abbreviated PMN-10PT and PMN-25PT). The samples were fabricated using solid-state route as describe in (Boucher *et al*., 2004; Sebald *et al*., 2006). Mn-doped PZT ceramic was prepared by coprecipitation of oxalates and hydroxides and dried at 100°C for 10 h, whereas the PMN-10PT and PMN-25PT were prepared with stoichiometric proportions using a two stage synthesis process under air. The sintering temperature for both compositions is 1230°C during 120 min. After the sintering process, the average thickness and diameter of all the samples were about 1 mm and 14 mm, respectively.

4.5.1.2 Characterization Procedure

For the analysis of phase content the sintered bodies were checked by X-ray powder diffraction (XRD, Philips X′PertMPD, Ni-filtered CuK radiation) to identify the desired perovskite phase without pyrochlore. Prior to measurements, each disk-like sample was poled under the same condition regardless to the different thicknesses and compositions. The poling procedure used a DC electric field of 2.5 kV·mm^{-1} in silicone oil for 2 min at a temperature of 120°C and 50°C for PZT + 1mol%Mn and PMN-25PT, respectively. The poling field was chosen to be close to the coercive field, ensuring a maximal remnant polarization (it has been demonstrated in (Sebald, 2006) that for higher electric fields, the remnant polarization does not increase any longer), and the temperature has been determined to increase the mobility of the dipoles without compromising the poling procedure by ensuring a temperature much less than the Curie point. From the poling temperature, the poling time has been chosen to ensure a good alignment of the dipoles. The microstructures of the as-sintered surfaces of the samples were imaged using scanning electron microscopy (SEM, JeolJSM-5800LV). Electrical measurement was made on ceramics with density that was about 1.8 g·cm^{-3}. To investigate electrical properties, a silver

was pasted on both sides of the surfaces of the disc samples. The capacitance and dissipation factor (D) of the samples were measured using a high precision LCR meter (Hewlett Packard 4284A) at 1 kHz from which the dielectric constant was calculated. The piezoelectric strain coefficient was determined using a Berlincourt meter. An impedance analyzer (Hewlett Packard 4194A) with a frequency range of 100 Hz - 4 MHz was used to determine the resonant frequency of all the samples. All measurements were performed in room condition.

4.5.1.3 Results and Discussion

As the first investigation, the XRD patterns of the two piezoceramics could be well identified to be a standard perovskite structure (see Figure 4.8). In particular, the peak at $2\theta = 31°$ corresponds to the (110) plane, that exhibited a tetragonal symmetry of a perovskite crystal. In the XRD pattern of the PZT-1mol%Mn, no pyroclore phase was found while the pattern of the PMN-25PT showed a small amount of pyroclore. A volume percentage of the perovskite phase for each composition was calculated from equation (4.23) and it was found to be higher than 90% for all of samples.

$$\text{perovskite (\%)} = \frac{I_{perovskite} + I_{pyroclore}}{I_{perovskite}} \times 100\% \qquad (4.23)$$

Figure 4.8 shows the microstructure of the fracture surfaces of the piezoceramics sintered at the same temperatures. Variation in the average grain size estimated from the SEM graphs of the piezoceramics related to the type of doping. The change of bulk density and the pore morphology with introducing doping into PZT texture can be observed with grain size range from 1-3 μm. Once can notice that the more porous structure of the neat PZT due to its low relative densities (6.629 g·cm^{-3}).
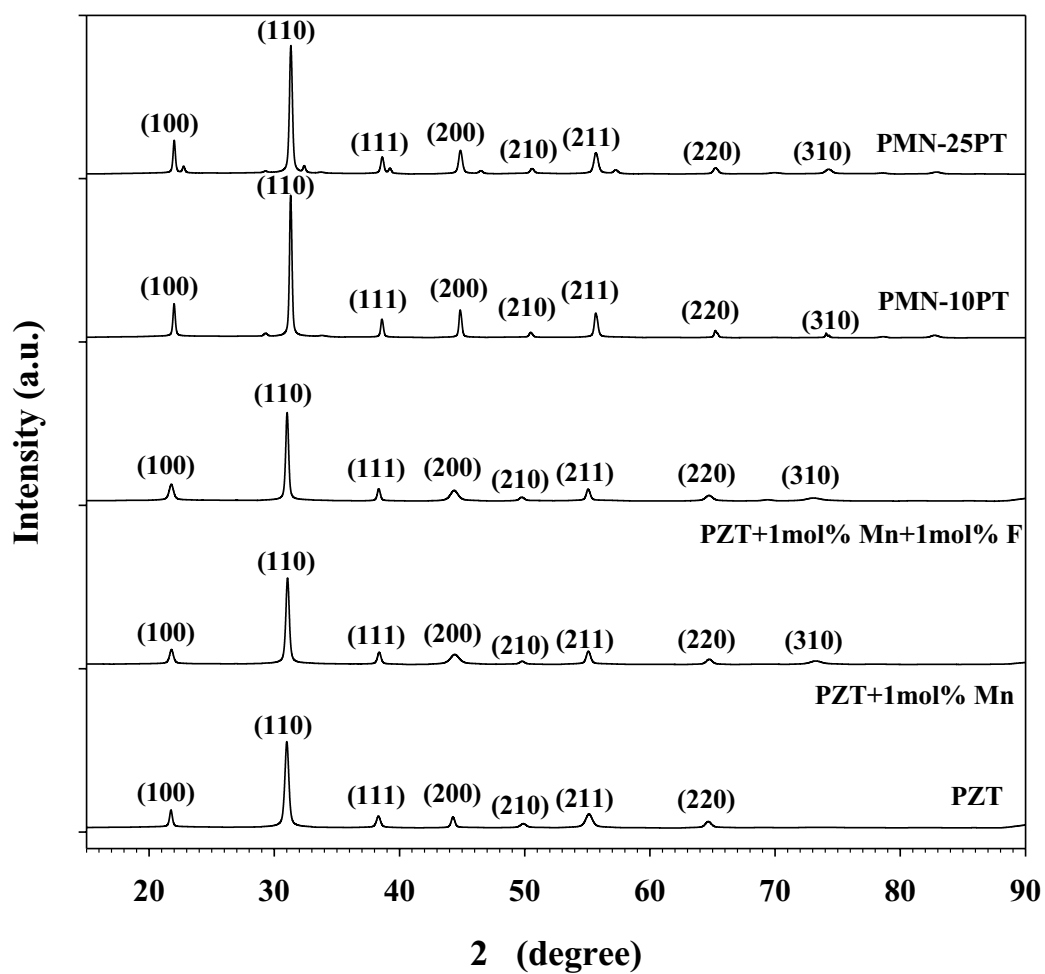
Figure 4.8 XRD pattern of PZT, PZT+1%Mn, PZT+1%Mn+1%F,

PMN-10PT and PMN-25PT.
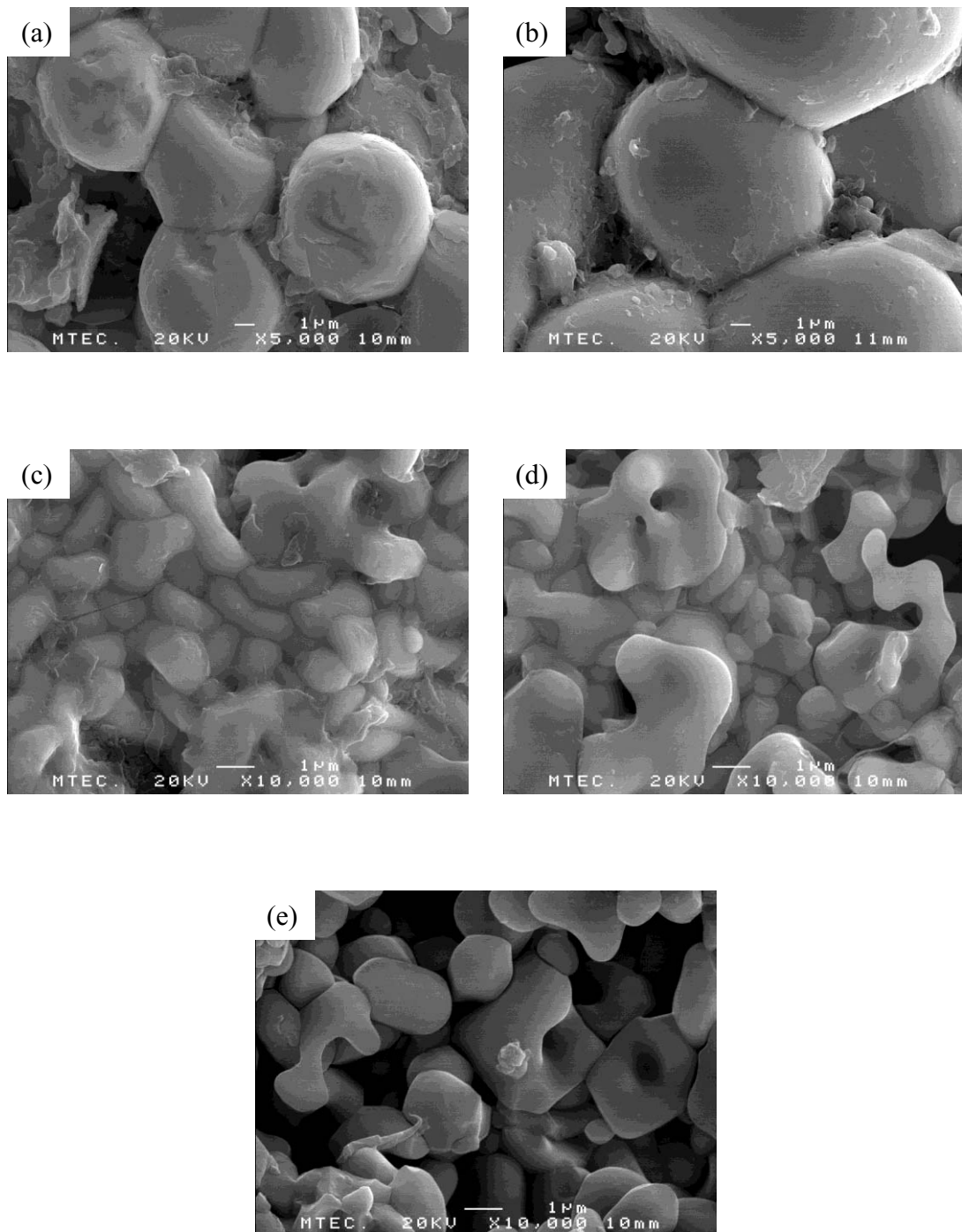
Figure 4.9 Microstructure and average grain size of (a) PMN-10PT (b) PMN-25PT

(c) PZT+1mol% Mn+1mol% F (d) PZT+1mol% Mn and (e) PZT sample observed

by SEM.

Figure 4.9 shows the SEM micrographs of the morphology of the piezoceramics. The PT and Mn respectively introduced in PMN and PZT systems resulted in differences in shape and average grain size of the samples. It can be seen clearly that the PMN-25PT has regular cubic grains and the Mn-doped PZT has smaller grains with a combination of different shapes. A summary of the properties of various compositions is shown in Table 4.1. A relatively dense morphology and regular grain patterns of the PMN-25PT led to higher values of piezoelectric coefficient d_{33}, mechanical quality factor Q_M and squared coupling coefficient k^2. It should be a better choice of piezoceramic samples for energy harvesting applications. However, the performance in terms of energy harvesting for both compositons is analysed in the next section. It is obvious that PMN-25PT and PZT-Mn exhibited a great piezoelectric activity with low loss which appropiate for use in energy harvesting application.

Table 4.1 Summary of various properties of piezoceramic samples

sample	ε_{33}^{T} (nF.m^{-1}) (1kHz)	tan (1kHz)	d_{33} (pC.N^{-1})	$-d_{31}$ (pm.V^{-1})	Q_m	k^2	s_{11}^{E} ($\times 10^{-12}$ m^2/N)
PMN-10PT	9.0	0.0603	No response	-	-		-
PMN-25PT	1.9	0.03	235	17	127	0.11	15.2
PZT	8.4	0.07	111	0.8	357		17.6
PZT-Mn	6.5	0.02	145	53	197	0.02	24.8
PZT-Mn-F	5.6	0.03	140	0.8	303		15.1

4.5.2 Electronic Aspect

4.5.2.1 Theoretical Study

The first step for the design of the harvesters consisted in determining the optimal sample thickness in order to maximize the coupling coefficient. This process has been done using ANSYS FE software, and results are depicted in Figure 5.3. These results show that the optimal thickness of the PZT-based sample is much less than the PMN-PT (200 μm vs. 600 μm), the latter featuring a significantly higher coupling coefficient ($k^2 = 0.07$ for the PMN-25PT while $k^2 = 0.045$ for the PZT + 1mol%Mn). Hence, one can expect that the PMN-PT-based harvester would be more efficient. However, due to minimal limit and uncertainties during the cutting process, the sample thickness are respectively 0.36 mm and 0.54 mm for the PZT + 1mol%Mn and for the PMN- 25PT.
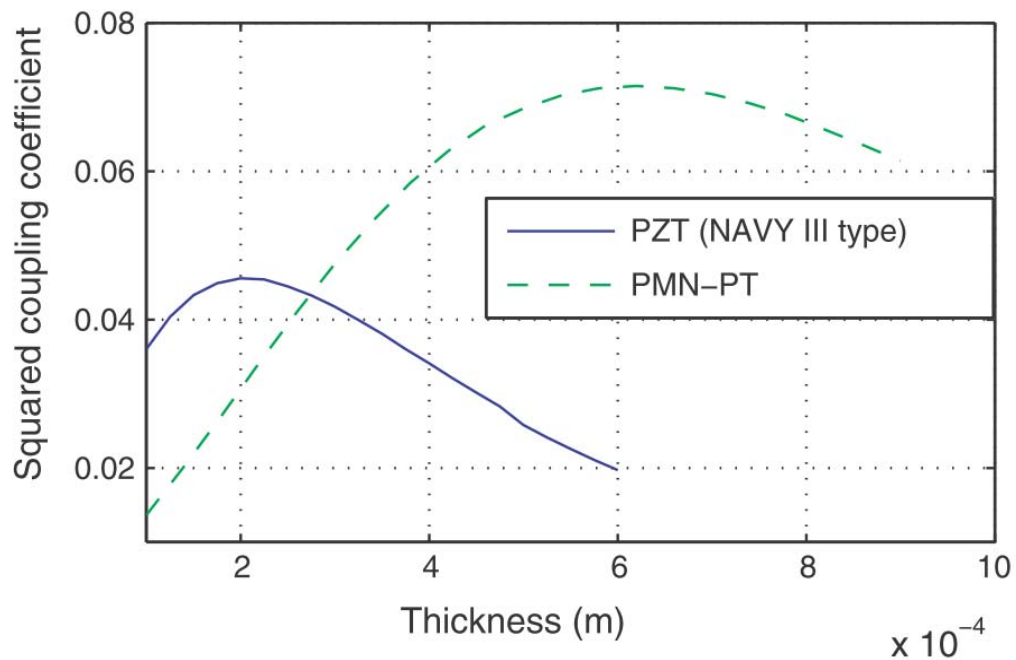
Figure 4.10 Evolution of the global electromechanical coupling coefficient as a function of the sample thickness.

In order to assess and compare the power generation abilities of the materials, preliminary experimental measurements have been carried out in order to determine the model parameters for each cantilever beam. The experimental

procedure is similar to the one exposed in (Badel *et al*., 2006), and obtained parameters are given in Table 4.2.

Table 4.2 Experimental parameter identification

Parameter	Value	
	PZT+1mol%Mn	**PMN-25PT**
Dynamic mass M	11×10^{-2} g	9×10^{-2} g
Structureal damping coefficient C	3.3×10^{-3} N·s·m^{-1}	3.5×10^{-3} N·s·m^{-1}
Short-circuit stiffness K_E	27.8 N·m^{-1}	26.2 N·m^{-1}
Force factor	$3.0\times10\text{-}5$ N·V^{-1}	$6.5\times10\text{-}5$ N·V^{-1}
Blocking capacitance C_0	3.8 nF	5.4 nF
Resonance frequency f_0	79 Hz	88 Hz
Inversion coefficient	0.85	0.85

The power outputs of the standard and SSHI interfaces as a function of the resistance and of the figure of merit given by the product k^2Q_M of the squared coupling coefficient by the mechanical quality factor are depicted in Figure 4.11, and the maximum harvested powers in Figure 4.12. These figures clearly demontrates the ability of the SSHI interface for enhancing the energy harvesting abilities for low values of k^2Q_M, while both the standard and SSHI techniques feature similar maximum output power for high value of the figure of merit. Figure 4.12 displays that the SSHI get closer to this limit much quicker than the standard approach (Guyomar *et al.*, 2005; Lefeuvre *et al*., 2006; Shu *et al*., 2007), however, no particular investigation of the energy harvesting abilities of different ceramic compositions using the standard or nonlinear interfaces has been studied.
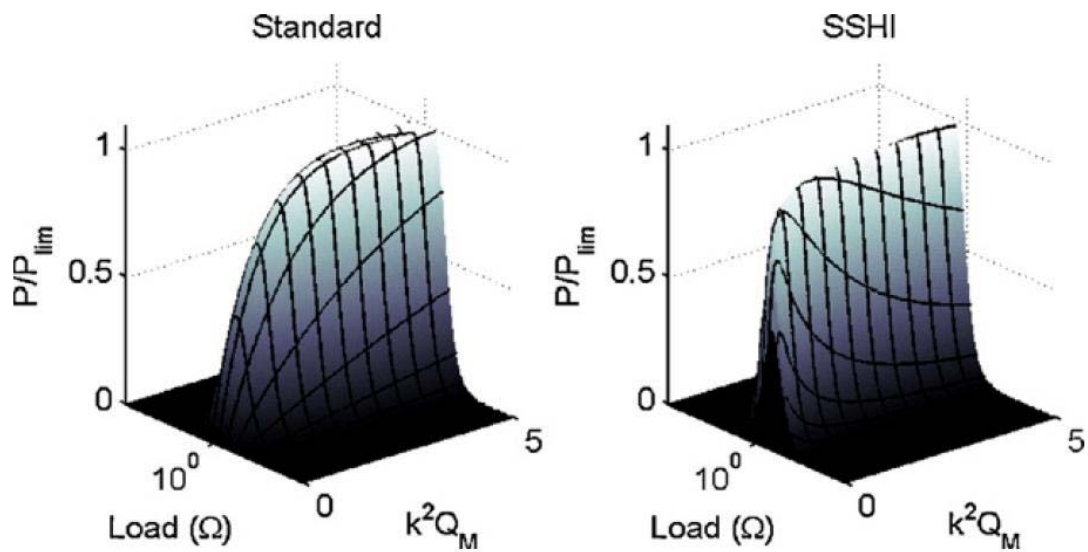
Figure 4.11 Normalized power output as a function of the load and k^2Q_M (= 0.85).
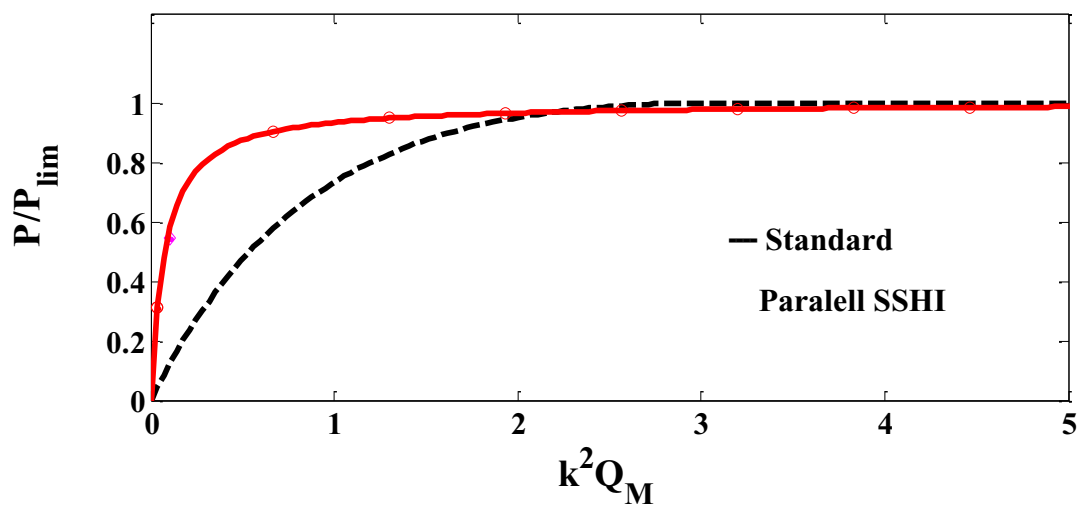
Figure 4.12 Normalized maximum power output as a function of k^2Q_M (= 0.85).

4.5.2.2 Experimental

It consists of driving the cantilever beam using an electromagnet connected to a function generator, which applies an electromagnetic force on the magnetic tip mass. An inductive proximity sensor is used in order to monitor the displacement (Figure 4.13). This sensor is also connected to a DSP (dSpace ^{TM} system) for detecting the minimum and maximum values of the displacement (such a detection can nevertheless be done in a truly self-powered fashion as it will be discussed in the next section). This system is controlling the digital switches (2N7000 MOSFETs) connected to the piezoelectric element through an inductance of 100 mH, in order to apply the nonlinear treatment. In addition to the switching interface, the harvesting stage is composed of a full diode bridge rectifier (DF005) and smoothing capacitor of 10 μF. This interface is connected to a resistance box, whose value can be made varying in order to determine the power generation abilities of the device with respect to the load R_L.

Each sample is bonded on a spring steel cantilever beam whose dimensions are $55\times17\times0.5$ mm^{-3}, and featuring a $6\times6\times2.5$ mm^{-3} magnetic tip mass of 0.78 g, as depicted in Figure 4.13. Hence, in the followings, the analysis will be done considering the whole electromechanical device made of the beam, the piezoelectric material and the tip mass.
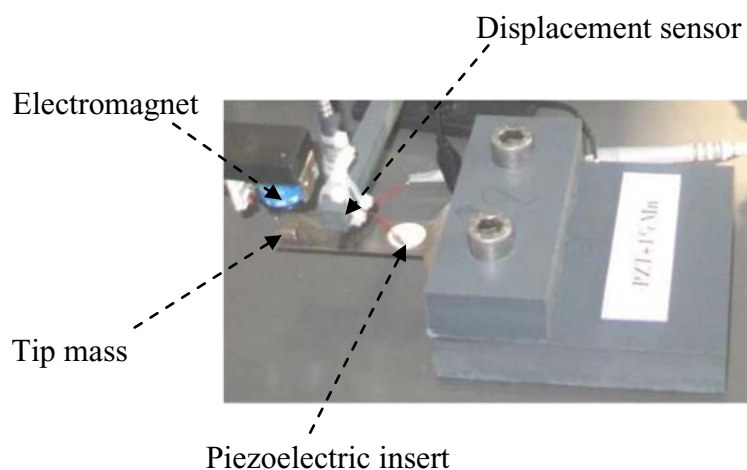
Figure 4.13 Energy harvesting structure in experimental set-up.

4.5.2.3 Results and discussion

Obtained results using either the standard or SSHI approach for energy harvesting are depicted in Figure 4.14. As expected, this figure clearly demonstrates that the PMN-based sample is much more effective for converting energy using the standard technique. However, a major result of this work is the ability of the SSHI to significantly decrease the power generation difference from one composition to another.
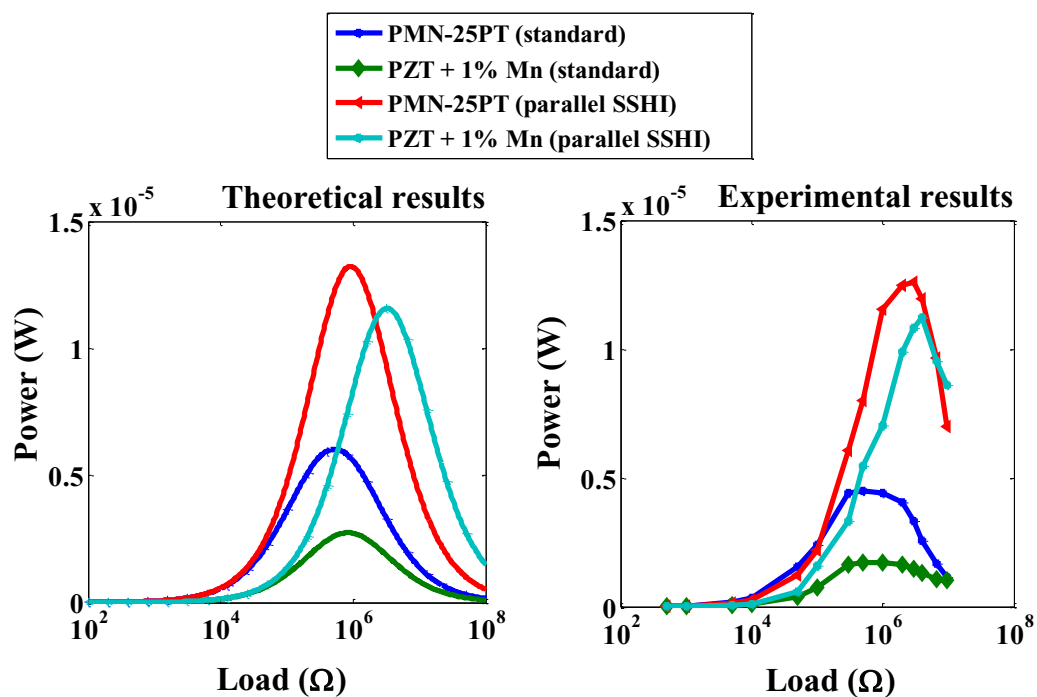
Figure 4.14 Experimental harvested power using standard and SSHI approaches $(F_M = 0.64 \text{ mN})$.

As expected from the theoretical power output predictions, experimental results not only indicate that the SSHI approach allows a significant gain in terms of harvested power, but above all allows the use of less efficient (and therefore cheaper) piezoelectric materials without compromising the power generation abilities of the harvester (or equivalently permits using less amount of material). Such an effect is mainly explained by the damping effect that arises for structures featuring high values of the figure of merit $k^2 Q_M$. Actually, as the nonlinear technique permits

an artificial increase of the coupling coefficient (Table 4.3), the critical value of k^2Q_M (equals to   as shown by equation. (4.18) for which the power limit P_{lim} is reached is greatly reduced.

Table 4.3 Energy harvesting ability comparison.

	PZT + 1mol%Mn	PMN-25PT	PMN-25PT gain
Harvested energy in standard approach	1.7 μW	4.5 μW	160%
Harvested energy using SSHI	11.2 μW	12.6 μW	12%
Global coupling coefficient	9.32%	17.3%	86%
Equivalent coupling coefficient using SSHI	24.4%	32.7%	34%

4.6 Implementation Considerations

The elaboration, design and implementation of the microgenerator were considered in terms of materials and electronic interface in details was discussed in this section.

From the material side, it has been demonstrated that the PZT+1mol% Mn features lower conversion abilities than the PMN-25PT. However, the elaboration of the latter is much more delicate and complex (and thus costly) because of the need of adjusting finely the quantity of MgO in order to minimize the pyroclore phase. Hence, the synthesis is usually made into three steps (Yamada 1999):

1. Preparation of the mixed oxide $MgNb_2O_6$ (columbite method)
2. Mixing with $PbO + TiO_2$
3. Calcination

Filter   Switch

Comparator
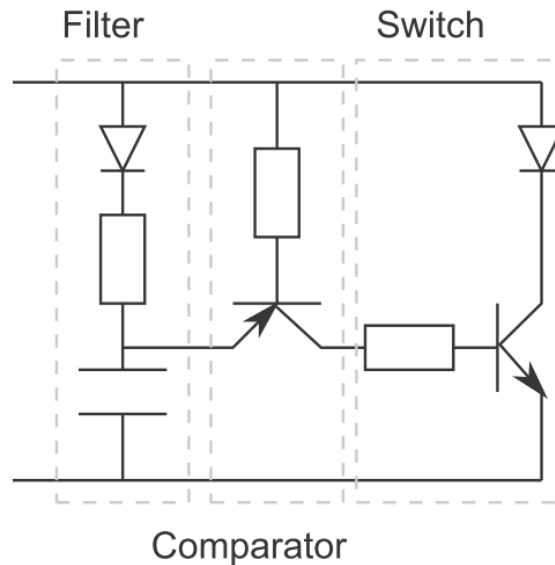
Figure 4.15 Self-powered maximum detector combined with the digital switch.

In contrast, the elaboration of Mn-doped PZT powder is much easier (it only consists in mixing the reagents together) and the pure single phase PZT easier to obtain, making it simpler and cheaper to produce. In terms of electronic interfaces, the main challenge is the implementation of the digital switch. However, it has been demonstrated in the litterature that this device can be easily made self-powered using a very few amount (typically 3-5%) of the electrostatic energy available on the piezoelectric element under classical working conditions (Richard *et al*., 2007, Lallart *et al*., 2008), therefore having no significant impact on the total harvested power. The principles of operations of this self-powered switching device consist of comparing the piezoelectric voltage signal with its delayed version. Then when the delayed version is lower than the original piezovoltage while being positive, a maximum value is detected (the minimum detection is done by inverting the electrodes of the circuit). Such operations can simply be done using off-the-shelf components (resistors, capacitors and transistors), making its integration quite easy while having a very low cost (Figure 4.15). From Figure 4.14, it can also be shown that the optimal load when using the nonlinear interface also increases compared to the standard case. Nevertheless, it has been demonstrated that, in order to match the optimal value of the connected load, several configurations can be adopted (Ottman *et al*., 2002, Han *et al*., 2004).

In particular, the studies presented in (Ottman *et al*., 2003) and (Lefeuvre *et al*., 2007) show that using DC/DC converters operating in discontinuous mode allows the adaptation between the energy extraction interface and storage stage, therefore ensuring a maximal harvested power whatever the load connected to the system. Therefore, from these observations and from the previous analyses and experimental investigations, it can be drawn that using highly coupled electromechanical systems for energy harvesting applications is not as advantageous as it may be thought, as the power is limited due to the induced damping effect (Figure 4.12). Instead, using nonlinear interfaces that allow artificially increasing the coupling coefficient of the material is a low-cost, easily embeddable and efficient way for improving the energy harvesting abilities, resulting in a dramatically reduced cost while achieving similar performance than expensive materials featuring high natural coupling coefficients.

4.7 Conclusions

This chapter exposes the comparison of several energy harvesters both from the material and electronic aspects. From two different compositions of piezoelectric materials, it has been shown that the PMN- PT features higher coupling coefficient than the PZT-based sample, making such a composition a better choice for energy harvesting purposes at a first glance. Although PMN-PT based harvester effectively allows harvesting approximately twice the power of PZT-based device when using a classical electrical interface, the use of a nonlinear approach for enhancing the conversion abilities of piezoelectric elements dramatically reduces the difference between the considered microgenerators.

CHAPTER 5

VALIDATIONS OF ENERGY HARVESTING ON PVDF

This chapter aims to present the realization of the PVDF for energy harvesting. The performance of the PVDF-based materials for converting vibration energy to electrical energy is described theoretically and experimentally.

5.1 Review of Previous Work

As presented in Chapter 2, poly(vinylidene) fluoride is a thermoplastic polymer. The molecular formula is $(-CH_2-CF_2-)_n$ PVDF is synthesized by addition polymerization of the $CH_2=CF_2$ monomer

$$n(CH_2=CF_2) \xrightarrow{\text{Catalyst}} -(CH_2-CF_2)_n-$$
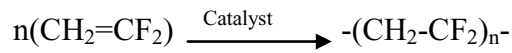
PVDF is a semi-crystalline polymer. The crystalline form consist of a non-polar *alpha* phase and a highly polar -phase (Figure 5.1). Where the -phase is a non-polar phase, whereas the -phase has the hydrogen and fluorine atoms arranged to give maximum dipole moment per unit cell.

(a)   (b)
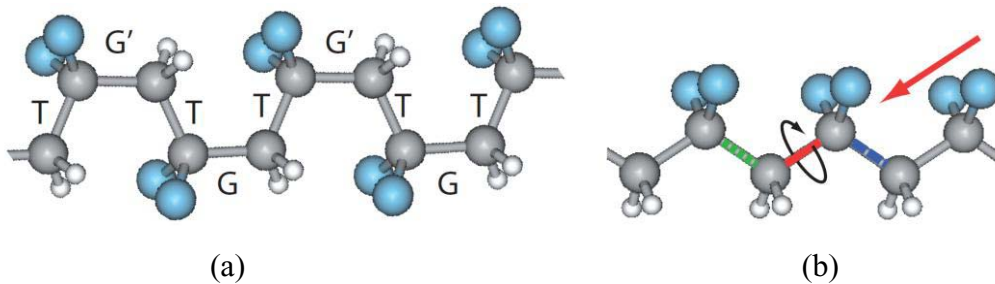
Figure 5.1 Two phases of the PVDF are presented: (a) -phase consisting of a series of non-polar anti-parallel chains, whereas (b) -phase is a series of polar parallel chains (Gysel, 2008).

In order to enhance the piezoelectric properties of PVDF, the stretching and poling process is the most common approach. The stretching is for transforming the desire phase and can be ascribed by the so-called "cold drawing" approach. Cold drawing is a solid transformation process which is conducted near room temperature and below the melting transition temperature of the crystalline or semi-crystalline polymer. However, the thermoplastic such PVDF, is brittle at room temperature and can only be drawn at an elevated temperature. The process yields a high degree of chain axis alignment by stretching or drawing the polymer with major deformation in the neck region. Applied tensile drawing stress resulting in thinning and elongation of crystal and rotation of molecules or bundles in the drawing direction; increasing the draw ratio is known to increase the Young's modulus and breaking strength by improving the degree of molecular alignment or extension. The dipole moments are randomly oriented until the polymer is electrically polarized. Under the application of an electric field, the polymer chains inside the crystallites align themselves along the field by rotating the dipoles around the chain axis. The piezoelectric response of PVDF polymers is the result of a net polarization (Figure 5.2).
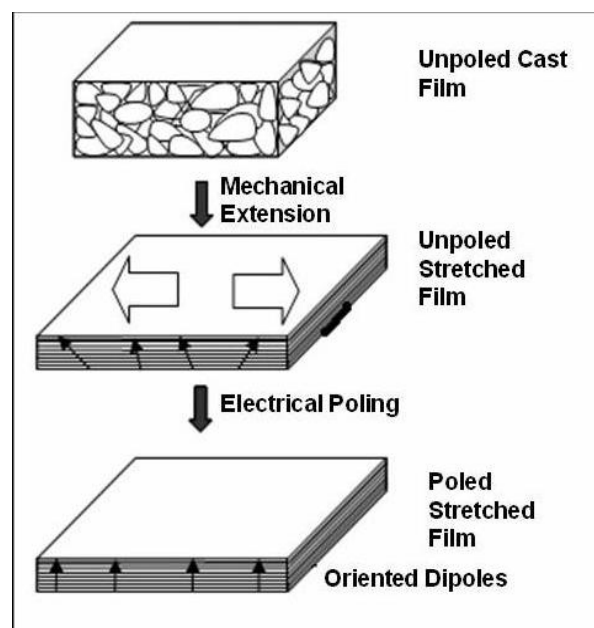
Figure 5.2 Main procedure for preparation of PVDF sample. (Mani, 2005).

To further improve the piezoelectric performance of piezopolymers, several researches have focused on the effect of temperature and drawing ratio to piezoelectric properties and so on. Also, the temperature and electric field for poling are interesting. For example, Eberle and and Eisenmenger (1991) investigated the effect of temperature between 25 $^{\circ}$C and 120 $^{\circ}$C to align the dipole at a constant electric field (60 MV·m^{-1}). They found that the alignment of the dipole took place in a central poling zone during some hours of poling at 25 $^{\circ}$C. The poling time was necessary reduced to some pint in order to align the dipoles in this narrow zone when the temperature was increased up to 120 $^{\circ}$C. Another example, changes in the reciprocal space has been examined for the poled -form of PVDF. The results are consistent with a phase transition from -form to an oriented polar form ($_p$) involving the rotation of the TGTG$^-$ chains at the poling temperature near 1 MV·m^{-1}. While the polar structure as such -phase was formed as higher fields near 5 MV·cm^{-1} was apllied (Davis *et al*., 1978). In addition, simultaneous stretching and corona poling of PVDF films at elevated temperatures in batch mode greatly enhanced the piezoelectric constants. When poled under optimum conditions, a maximum piezoelectric constant of about 60 pC·N^{-1} was obtained using the optimum formation conditions. The thermal stability of the piezoelectric constant was greatly improved by applied electric field of about 0.55 MV·cm^{-1} at poling temperature, 80 $^{\circ}$C and 4.5 drawing ratio (Kaurat *et al*., 1991). Also, using the corona poling at a slow rate of drawing about 20 mm·min^{-1} the piezoelectric coefficient as high as 40 pC·N^{-1} has been obtained (Pantelis, 1984). Almost all researches report that drawing the PVDF at a temperature between 60 $^{\circ}$C - 80 $^{\circ}$C enhances the efficiency of the transformation phase (- to -phase). However, the consequent increase in chain mobility allows crystals orientation in the draw direction, without considerable deformation of crystal was observed at temperatures over 100 $^{\circ}$C (Liu *et al*., 2002).

5.1.1 *A Brief History on Using PVDF in Energy Harvesting*

Since the discovery of piezoelectric and pyroelectric properties of PVDF in 1969 by kawai, the number of publications on PVDF and PVDF-reinforced composite materials has grown very quickly, as evidenced by several recent reviews

on electromechanical behavior, fabrication, and application (Lang and Muensit, 2006) of such material. In 20 century, the most research interest focused on the renewable materials/energy as the demand for portable electronics and wireless sensors is growing rapidly (Sodano *et al.*, 2004). A significant amount of research has been occupied is improving performance of the PVDF and its copolymer as an energy harvester to harvest energy from the ambient environment such as acoustic signal, low-level vibration in household, work place, various moving objects including human movement.

Shoe-mounted PVDF piezoelectric transducer is one of the most interesting applications in this field. One example is taping stave PVDF mounted under the insole to harness the energy dissipated in bending the ball of the foot. The shoe scavenged energy from toe-off by bending a bimorph stave made from two eight-layer stacks of 28-micron PVDF sandwiching a 2-mm flexible plastic substrate bonded with epoxy (Figure 5.3). The hexagonal design shape was chosen to conform to the footprint and bending distribution of a standard shoe sole (Figure 5.4). Bending the stave elongates, the PVDF sheets on the outside surface are pulled into expansion, while those on the inside surface are pushed into contraction with respect to its plastic core in order to produce voltages across silver electrodes on each sheet through the dominant -31 longitudinal mode of piezoelectric coupling in PVDF (Figure 5.5). The output power of about 1.3 mW, calculated from measured voltage during a standard walk (0.9 Hz), was sufficient determined by terminated traducer with optimal resistive load (250 kΩ) which was connected in parallel to static capacitance as show in Figure 5.6 (Shenck and Paradiso, 2001; Kymissis *et al.*, 1998).
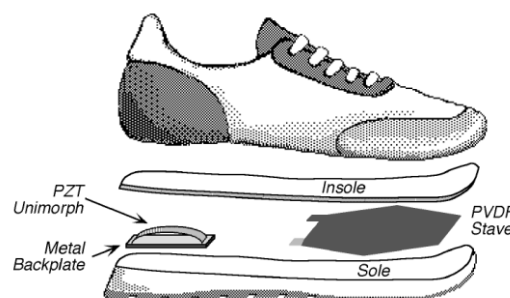
Figure 5.3 Integration of a PVDF bimorph stave under the insole

of a running shoe.
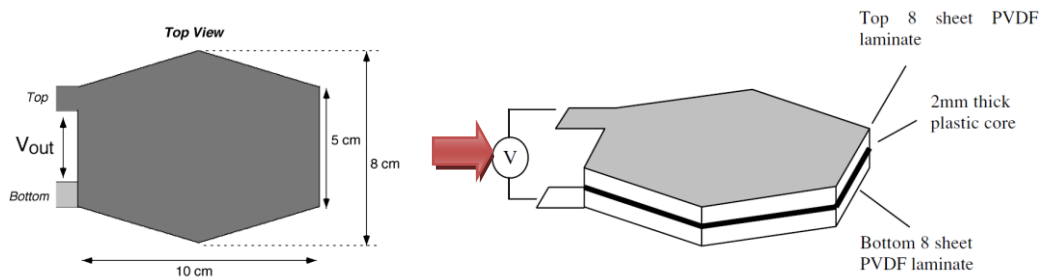
Figure 5.4 Layout of the PVDF shoe insole (Beeby, *et al*., 2006).
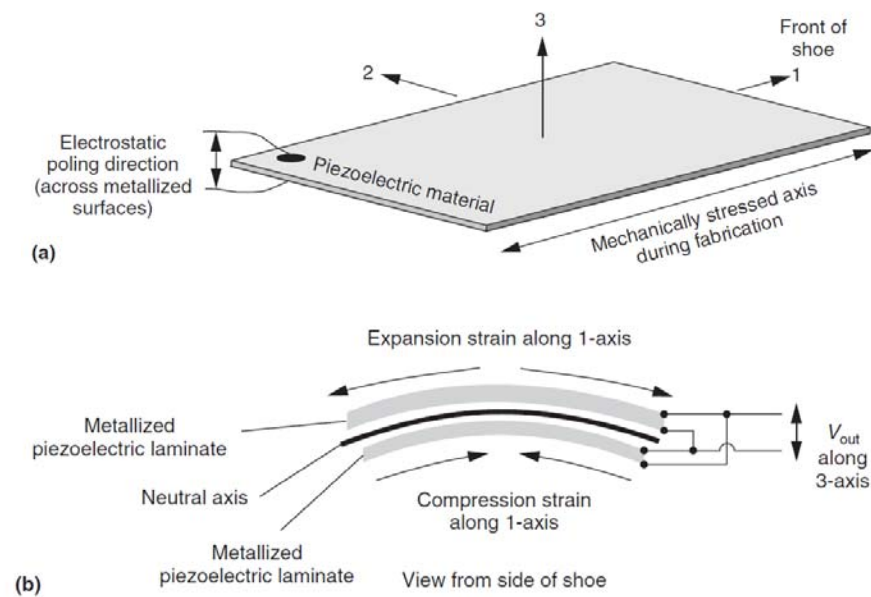
Figure 5.5 Conventional axis definition for a piezoelectric material (a) and applications rely on 31-mode (b) in bending.
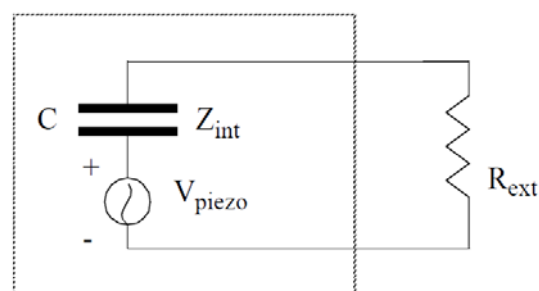
Figure 5.6 Circuit diagram of power test circuit.

Another example is the insertion of PVDF unimorph strips in heel strike. Each of the unimorph strips consist of one 0.5 inch tall, 52 μm thick silver laminated PVDF film bonded to the PET plastic film substrate with cyanoacrylate. The induced strain in PVDF is derived from the compression of polycarbonate which in turn bends the PET film. The analytical power of about 0.198 mW is generated from the shoe transducer at 470 kΩ with 1 Hz excitation and 3 mm displacement.

Figure 5.7 Complete shoe with transducer inserted in the heel and capacitor circuit attached. (Fourie,2009).

Another application worth mentioning is the artificial leaf project of Cornell University researchers so-called 'Piezo-tree' (Figure 5.8) that uses the flittering of leaves to produce electricity. The Piezo-tree's flexible plate and film made from flexible Polyvinylidene Fluoride (PVDF). The movement of leaves generate an AC signal by converting wind energy into electrical energy stored in a capacitor after rectifying it with a full-wave bride and can derive power of about 100 pW. The low power value is unable to drive even a common LED because of the weak piezoelectric strain coefficient of PVDF. Therefore, the researchers attached a piece of plastic film to the end of the leaf along the direction of air flow to enhance the power to around 100 times.
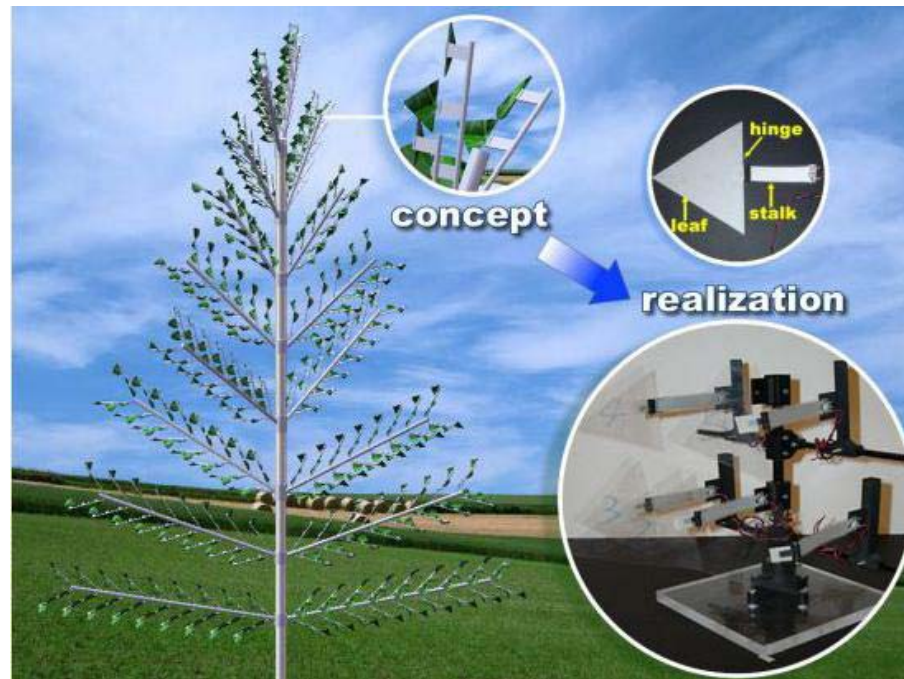
Figure 5.8 Schematic diagram of 'Piezo-tree' based-artificial-leaf-produces-electricity (http://www.energyharvestingjournal.com/).

Additionally, the capturing of energy from raindrops using a 25 micrometer thick piezoelectric PVDF is also an interesting model in this field which was created by the CEA/Leti-Minatec in France. The power can recover up to 12 mW for system works (Figure 5.9) with raindrops ranging in diameter from 1 to 5 mm. However, the energy produced depends on the size of the raindrop, oscillation frequency (frequency of rain drop) and the size of the piezoelectric film.

Figure 5.9 Testing apparatus of capturing energy from raindrop
(http://www.energyharvestingjournal.com).

An important method to enhance the amount of energy harvested from piezoelectric element is the utilizing coupling mode. There are two practical coupling modes (Figure 5.10), the -31 is the mode in which the poling direction is perpendicular to the applied force, another one is the -33 mode, a force is applied in the same direction as the poling direction. The bending beam and the compression of a piezoelectric block that are poled on their top and bottom surfaces are the example of the -31 and -33 mode, respectively. Even though, the -31 mode has a lower coupling coefficient, k, than that of the -33 mode, however it is the most commonly mode used coupling mode Baker *et al.,* (2005). In addition, the resonant frequency of a system operating in the -31 mode is much lower which makes the system more appropriate to be motivated at the resonance frequency of natural environment frequency as a result in higher power (Roundy *et al.,* 2003)
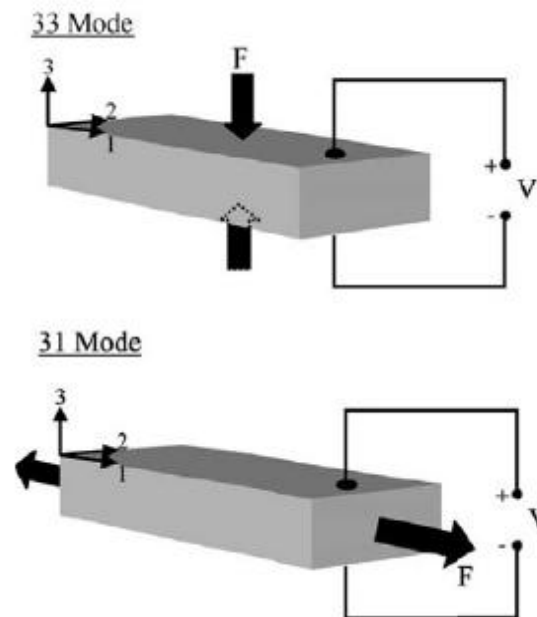
Figure 5.10 Illustration of -33 mode and -31 mode operation for piezoelectric

materials. (Anton and Sodano, 2007 originate from Roundy *et al.,* 2003).

5.2 Materials and Methods

5.2.1 Preparation of the PVDF Inserted on the Cantilever Beam

As mentioned in Chapter 3, the neat PVDF is a non-polar -phase, to enhance such polar structures it was stretched to its final dimension without rupture. To increase the   -phase, the stretched sample was electroded by sputtering an aluminium layer and subsequently subjected to a DC electric field of 40 MV·m^{-1} in a silicone-oil bath at 100 ^{o}C for 2 h. Then it was boned on the steel beam by epoxy glue (Figure 5.11). For PVDF composite, as discussed in Chapter 3 low-loaded composites are promising for certain applications such as energy harvesting. Unfortunately, it was broken during drawing so that this work used merely neat PVDF for converting mechanical energy into electrical energy. Additionally, concerning the electrical losses in the circuit, there is only the diodes for the standard circuit which can be neglected when the voltage is high enough (10V), while the diodes and the losses

in the switching circuit (SSHI) relate to the voltage just before switching process (V_{sw}) and the inversion coefficient as depicted in equation (5.1).

$$\text{Energy loss in SSHI circuit } = (1 - \gamma^2) \times V_{sw}^2 \qquad (5.1)$$

Owing to the energy loss in SSHI circuit which is too high for low-coupling coefficient material such as PVDF, this work focused on the evaluation of the neat PVDF by using the standard approach.
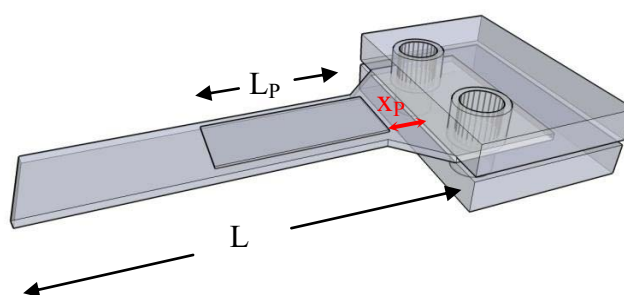
Figure 5.11 A schematic of a beam with a piezoelectric polymer rigidly boned on the surface of the beam.

5.2.2 Sample Characterization

Xray diffractometer (Philips X'pert X-ray diffraction system) was used to distinguish the phases of the sample. The monomers and phases that existed in the PVDF were precisely determined by a Fourier Transform Infra-Red (FTIR) spectra recorded in the range of 4000 - 500 cm^{-1} (Perkin-Elmer, EQUINOX 55, Bruker, with KBr as blank). All the samples including their morphology and infra-structure were visualized by using an Atomic Force Microscopic (AFM) technique (Nanosurf, Swizerland). The sample was then heated from room temperature (25 $^{\circ}$C) to 250 $^{\circ}$C at a heating rate of 10 $^{\circ}$C·min^{-1} to perform a thermal analysis by using a Differential Scanning Calorimetry (DSC) apparatus (Perkin Elmer). Its melting temperature, T_m and enthalpy could be determined at the onset of the thermal peaks and from the peak areas, respectively. The percentage of the molecules in the crystalline phase (crystallinity) was calculated from the heat of fusion of the sample to that of a

100%-crystalline PVDF (i.e., 104.7 J·g^{-1}). The fraction of -phase was calculated according to Greorio and Cestari. Dielectric constant, $_r$ and dielectric loss (tan) were measured by a HP-4263B LCR Meter. By using a resonance method, an electromechanical coupling factor can be determined from the resonant and antiresonant peaks

5.2.3 Experimental Set-up

The driving cantilever beam using an electromagnet connected to a function generator, which applies an electromagnetic force on the magnetic tip mass. The benefit in placing the mass at the tip of the beam is to reduce the resonances of the vibrating structure. A photonic sensor (MTI-2100, MTI Instrument, Inc) was used in order to monitor the displacement (Figure 5.12). This sensor is also connected to an oscilloscope (TDS 420 A Trektronix) for detecting the minimum and maximum values of the displacement. In addition to the switching interface, the harvesting stage is composed of a full diode bridge rectifier (W04M) and smoothing capacitor of 1 μF. This interface is connected to a resistance box, whose value can be made to vary in order to determine the power generation abilities of the device with respect to the load R_L.

Each sample was bonded on a spring steel cantilever beam whose dimensions are 55×17×0.5 mm^{-3}, and featuring magnetic tip mass of 1.645 g, as depicted in Figure 5.12. Hence, in the followings, the analysis will be done considering the whole electromechanical device made of the beam, the piezoelectric material and the tip mass.
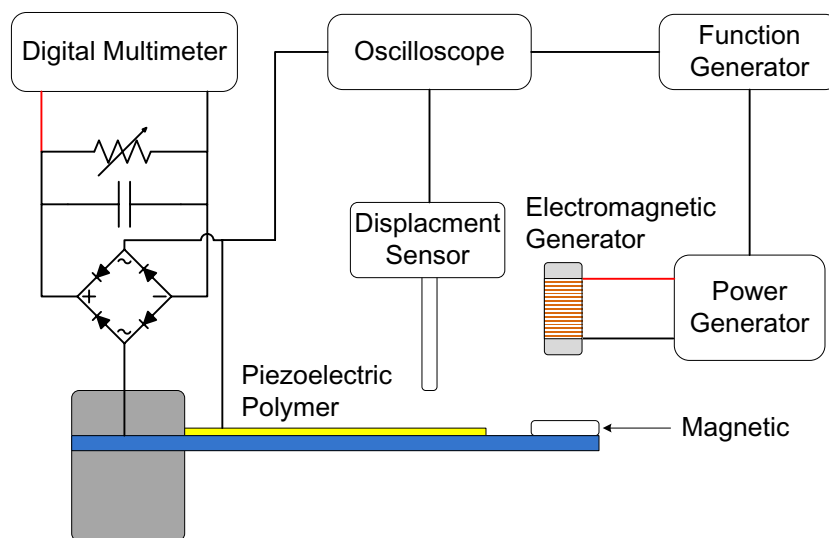
(a)
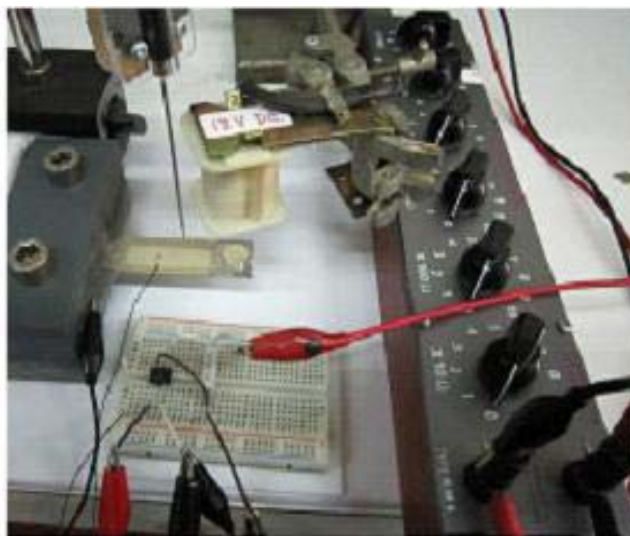
(b)

Figure 5.12 Energy harvesting structure (a) schematic view and (b) a pictorial view.

5.3 Results and Discussion

As mentioned in Chapter 4, piezoelectric materials generate a charge/voltage proportional to the rate of applied mechanical stress. In other words, produced voltage/charge varies with the displacement magnitude which also relate to piezoelectric material dimension and thickness. As seen in Figures 5.13-5.16 the displacement magnitude tend to depend on the dimension of PVDF so that the higher area as a results in larger displacement (high applied mechanical stress) or greater in charge generated by PVDF. Contrarily, the greater in mass (thickness) of PVDF insert lead to decline in bending displacement of the beam in turn to decrease in deformation of PVDF (low applied mechanical stress).
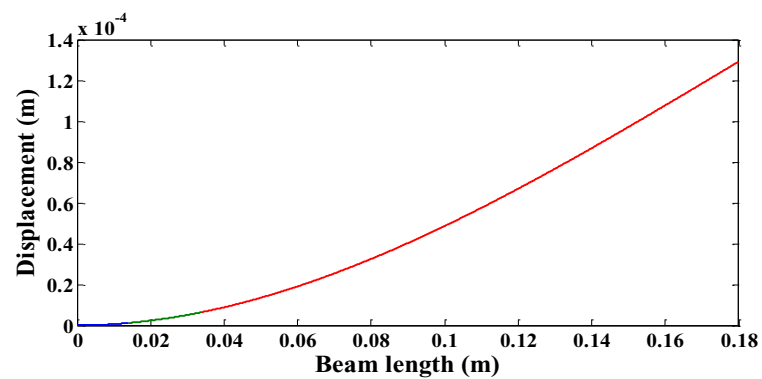
(a)
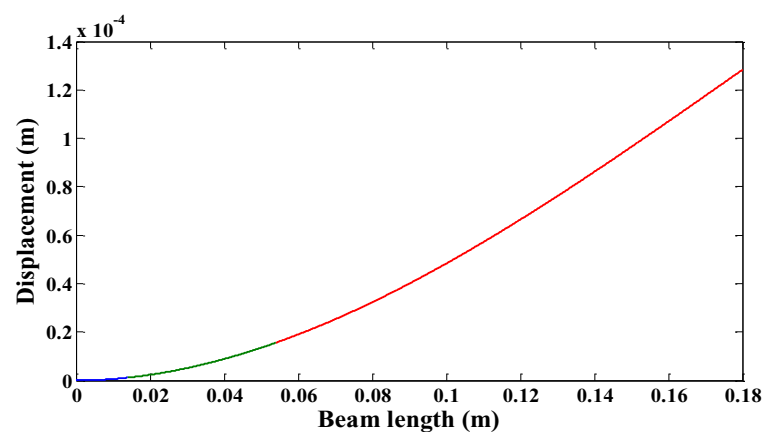
(b)

Figure 5.13 Normalized bending displacement as a function of length of beam for 28 μm-commercial PVDF at the length of PVDF (green line) of about (a) 2 cm and (b) 4 cm.
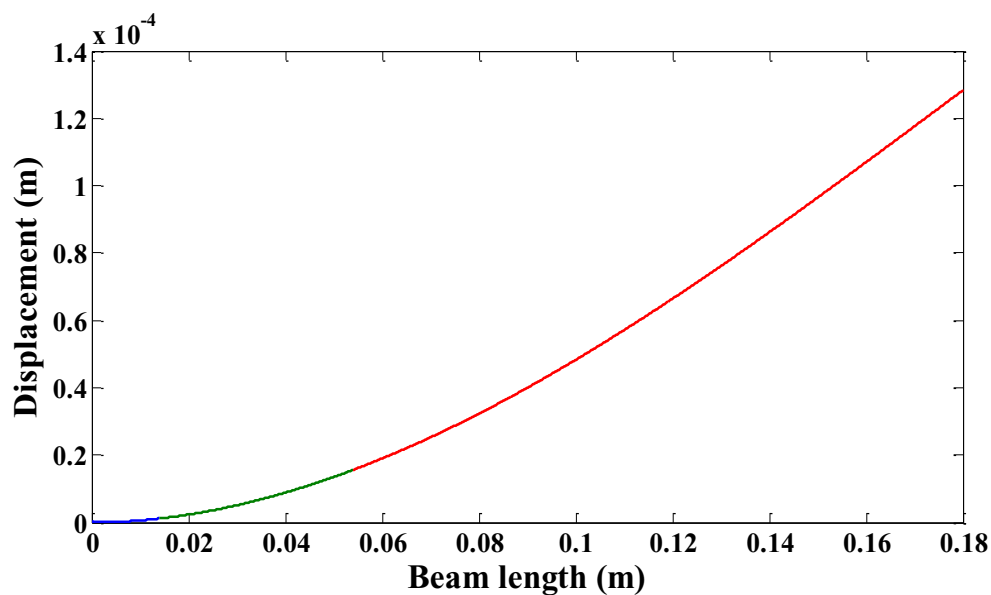
Figure 5.14 Normalized bending displacement as a function of length of beam for 28 μm-commercial PVDF at the length of PVDF of about 4 cm (green line).
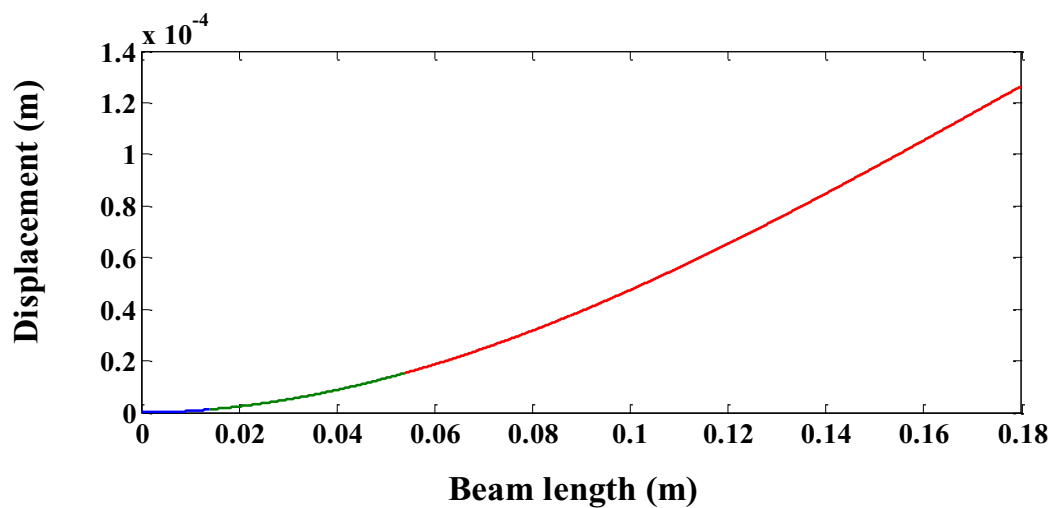
Figure 5.15 Normalized bending displacement as a function of length of beam for 52 μm-commercial PVDF at the length of PVDF of about 4 cm (green line).
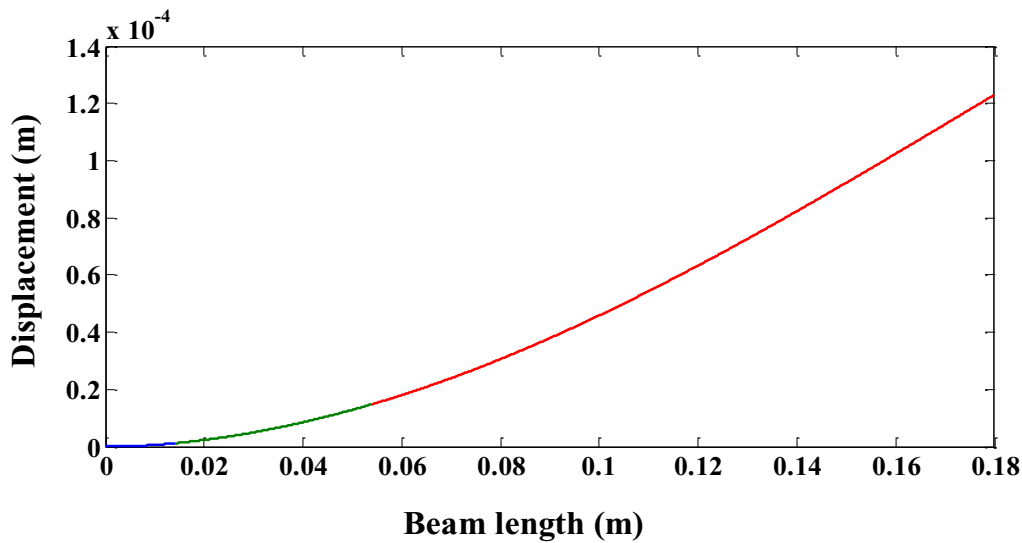
Figure 5.16 Normalized bending displacement as a function of length of beam for 100 μm-poled PVDF at the length of PVDF of about 4 cm (green line).

To predict a relationship of coupling coefficient (k^2) and the harvested power with the width and length of the beam at the constant force and dimension of the piezoelectric materials. The results clearly showed that the increase in coupling coefficient depended on the thickness of the piezoelectric material which led to the increase in output power as seen in the Figures 5.17-5.19. Additionally, the dimension of the beam also affected these values (coupling coefficient and output power). Moreover, the output power was a strong influence on the conversion efficiency between electrical and acoustic energy (k^2) greater than the bending magnitude of the beam which refers to the piezoelectric mass on the beam.

In the energy harvesting application, the great piezoelectric properties were required for the sample in which case, the PVDF sample must be a -phase. The XRD pattern of poled sample in the vicinity of 20.6 $^{\circ}$ shows a very high fraction of -phase when compared to the as-recieved one (Figure 5.20). In the case of -phase, three minor peaks were observed at about 18.5º, 26.8º and 36.3° corresponding to (020), (021) and (100) reflection in orthorhombic (Rakbamrung and Muensit, 2010; Ma, 2008). All the properties for PVDF materials are listed in Table 5.1.
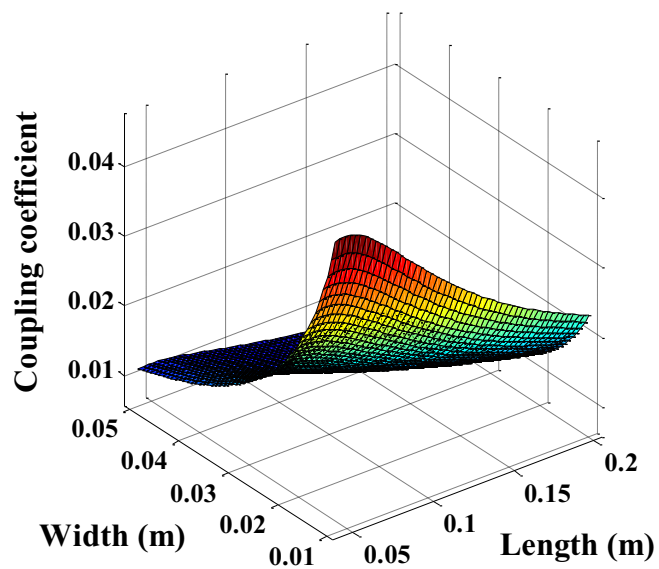
(a)
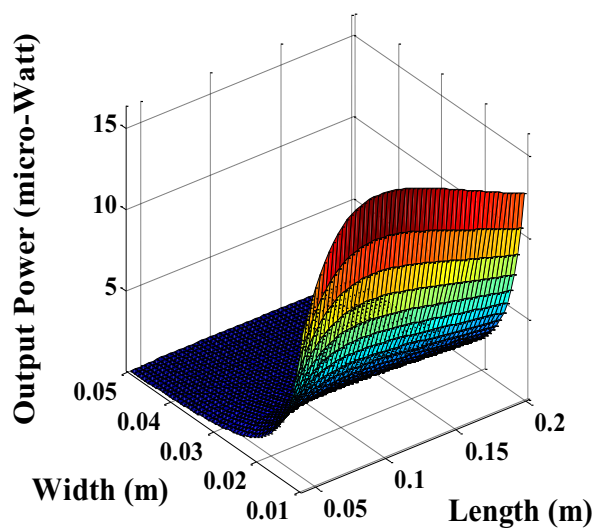
(b)

Figure 5.17 Normalized (a) coupling coefficient and (b) power output as a function
of width and length of beam for 28 μm-commercial PVDF.
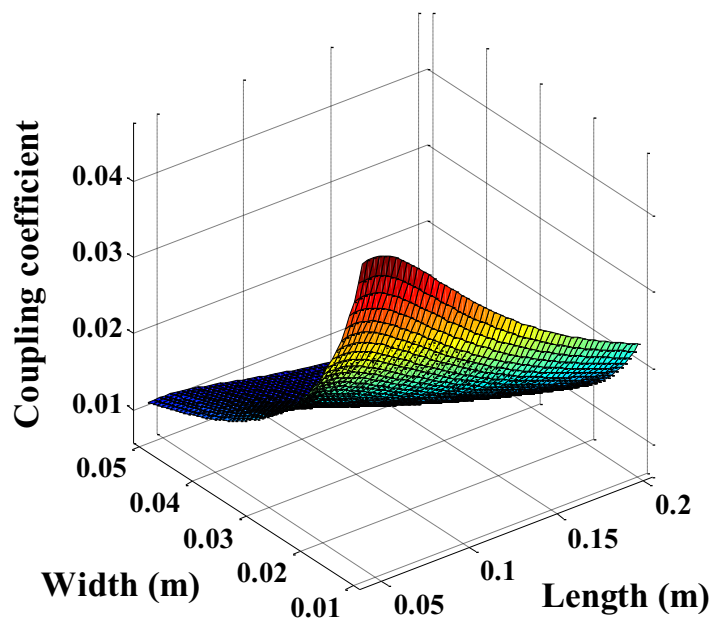
(a)
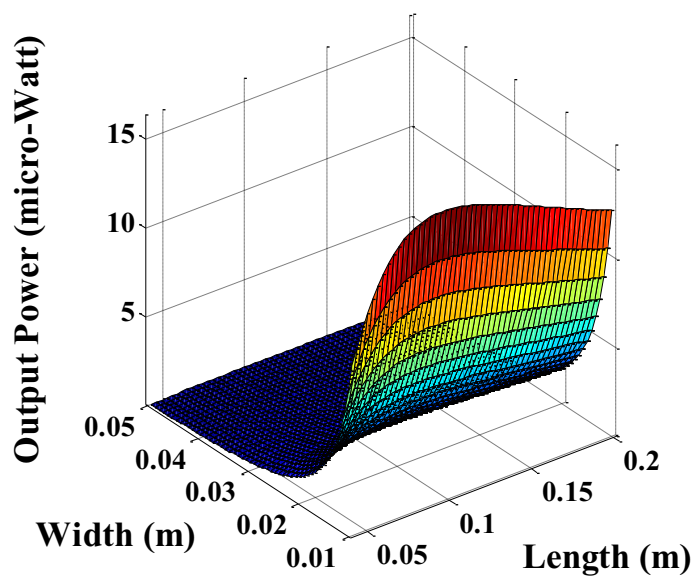
(b)

Figure 5.18 Normalized (a) coupling coefficient and (b) power output as a function of width and length of beam for 52 μm-commercial PVDF.
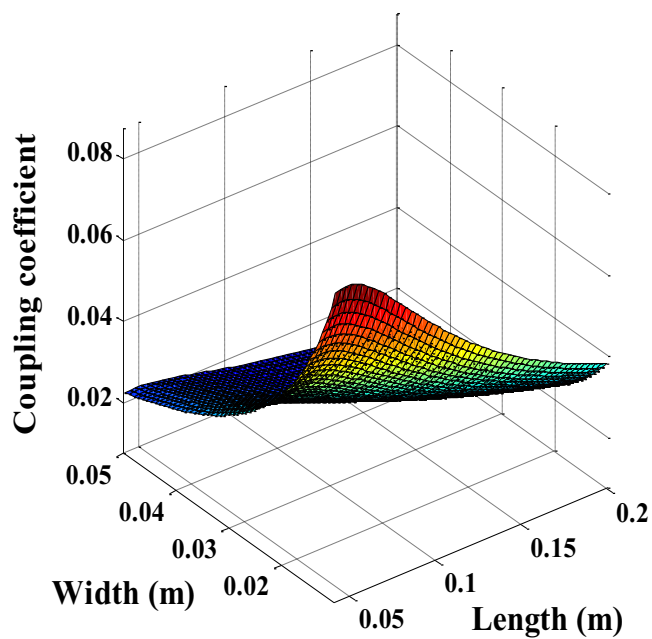
(a)
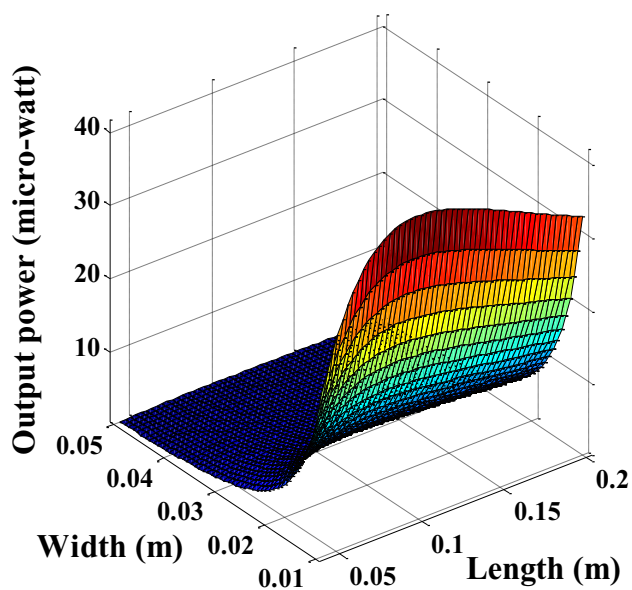
(b)

Figure 5.19 Normalized (a) coupling coefficient and (b) power output as a function of width and length of beam for 100 μm-poled PVDF.
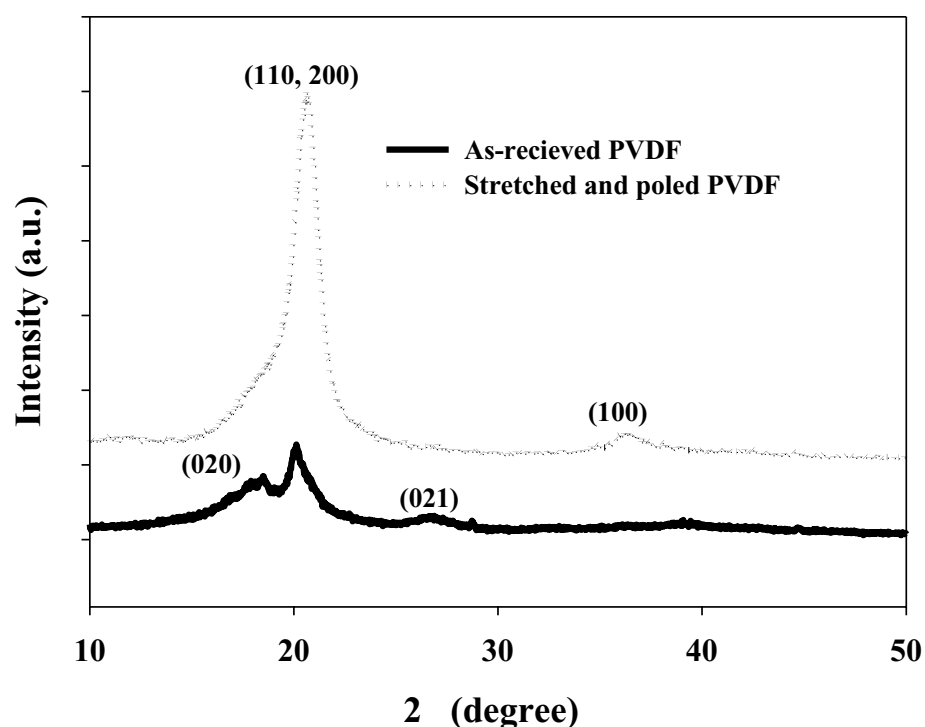
Figure 5.20 XRD patterns for as-received/neat PVDF and stretched and poled PVDF.

From Table 5.1, an increase in melting point (T_m) of PVDF with stretched and poled suggested that its crystals are thicker than another as supported by the result of its crystallinity. The result can be ascribed as the effect of the relatively high temperature and applied mechanical force which lead to the closely packed polymer chain intern to the formation of -phase. The more packing polymer chain and higher melting temperature as occurred in -phase is because of the conformation of all trans planar zigzag in its structure. FTIR spectra of - and -phase can be observed in all samples. The FT-IR spectrum ascribed the C=C (874, 1683 cm^{-1}), C-H (835, 1400 cm^{-1}), and C-F (762, 1167, 1230 cm^{-1}) stretching vibrations. The transmittance band in the wave number of about 762, 798, 874 and 1230 cm^{-1} was clearly characteristic for the non polar TGTG conformation as so called the -phase of PVDF. The required -phase as major phase appeared in the PVDF after stretched and poled. The vibration band which correspond to the -phase are described by CF_2 bending and CH_2 rocking.

Table 5.1 List of the properties for prepared PVDF in comparison to those of the commercial piezoelectric one (Measurement Specialties, Inc.).

	Commercial PVDF	**Neat PVDF**	**Poled PVDF**
Dimension	1 cm × 4 cm × 52 μm	1 cm × 4 cm × 50 μm	1 cm × 4 cm × 50 μm
Density (g/cm^3)	1.6	1.8	1.8
T_m (^{o}C)	171.5	159.0	160.8
Crystallinity (%)	52.8	57.3	51.6
FTIR data	In-plane bending or rocking (745 cm^{-1}) referred to -phase	CF$_2$-bending, CH$_2$-rocking referred to -phase	In-plan bending (745 cm^{-1}) referred to -phase
-phase (%)	45.24	-	42.70
$_r$, tan (1 kHz)	12, 0.01	5, 0.02	9, 0.02
Coupling factor	-	-	0.0293
Young's Modulus (psi)	160,000	-	160,000
Elastic compliance* (x10^{-11} m^2/N)	90.9		90.9
d_{33} (pm/V), g_{33} (m^2 /C)	62.14, 0.59	-	59.20, 0.74
d_{33} g_{33} (GJ/m^3)	27.5	-	22.73

*based on the Young's Modulus of the commercial PVDF

Using the AFM approach with non-contact mode provides a 3D profile of the surface on a microscale and using a feedback loop to monitor changes in the amplitude due to attractive Van der waals forces the surface topography can be measured. In Figure 5.21 the neat surface of the PVDF sample has a root-mean-square roughness of 15 nm. It was 10 nm in the stretched one and further reduced to be 8 nm after the poling process. The darkened area in the figure corresponds to the antiparallel-orientation molecular regions which were lesser and smaller in the poled

sample (Figure 5.22), indicating the transformation from   to   phase which correspond to the results in XED analysis (Figure 5.23). However, the images were not clearly displayed in the poling domain due to the low resolution of this method.

(a)   **(b)**   **(c)**
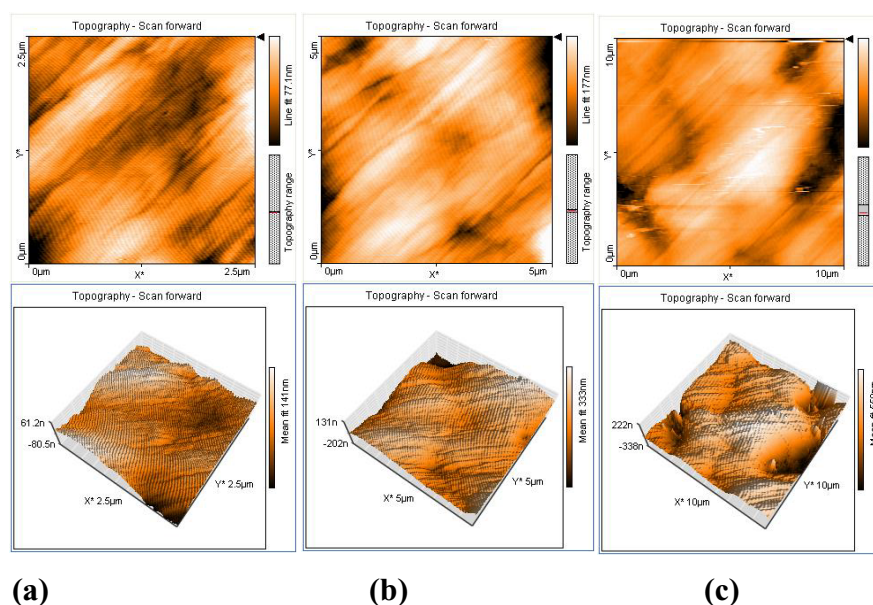
Figure 5.21 AFM images of the surfaces for the neat PVDF in the dimension of (a) 6.25 μm^2, (b) 25 μm^2 and (c) 100 μm^2.

(a)   **(b)**   **(c)**
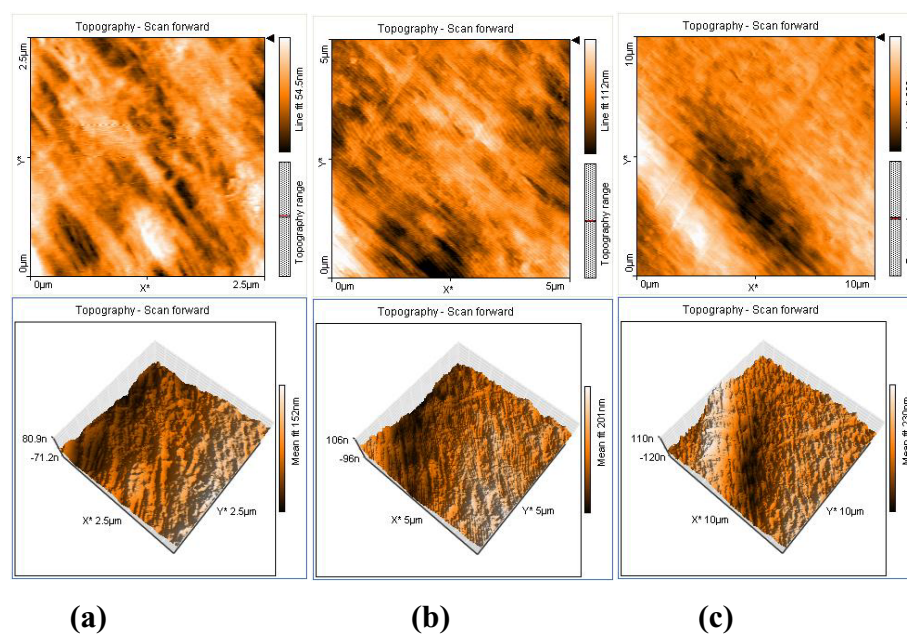
Figure 5.22 AFM images of the surfaces for the Stretched PVDF in the dimension of (a) 6.25 μm^2, (b) 25 μm^2 and (c) 100 μm^2.
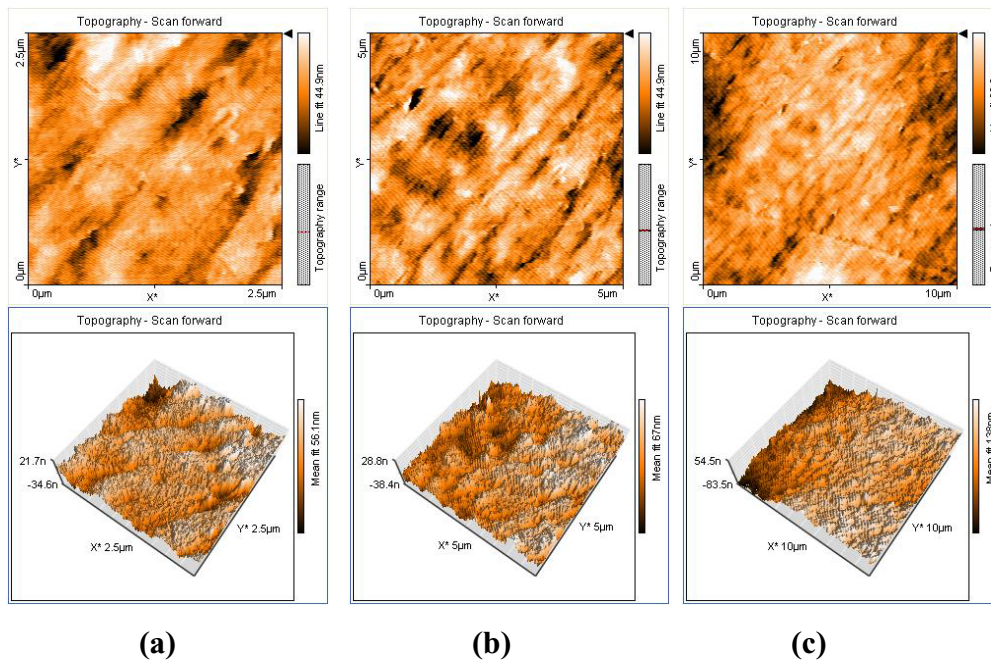
Figure 5.23 AFM images of the surfaces for the Stretched and poled PVDF in the dimension of (a) 6.25 μm^2, (b) 25 μm^2 and (c) 100 μm^2.

The load-dependent power delivered from each element was clearly shown in Figures 5.24-5.28. The harvested power depended extremely on the dimension of the piezoelectric materials as seen in Figures 5.24-5.27. Higher (dipole) area raised the generated charge more than using the increasing bending displacement of the beam. While the thickness of the piezoelectric material led to the enormous decrease in output power because of the low bending displacement (low applied stress) as seen in Figure 5.17. The charge/voltage generated and other parameter of PVDF samples showed in Table 5.2. The maximum harvested power of 2.6, 1.4 and 1.7 μW at 1.5 V were respectively obtained for 28 μm-commercial, 50 μm-poled and 52 μm-commercial PVDF elements, resulting in the respective values of the maximum power density of 229.6, 72.5 and 82.7 $\mu W \cdot cm^{-3}$ which can be used in wireless sensor applications (Roundy, 2003). The harvested power was shown to be very sensitive to the permittivity and final thickness of the material for the same optimal load of 1.6 MΩ.
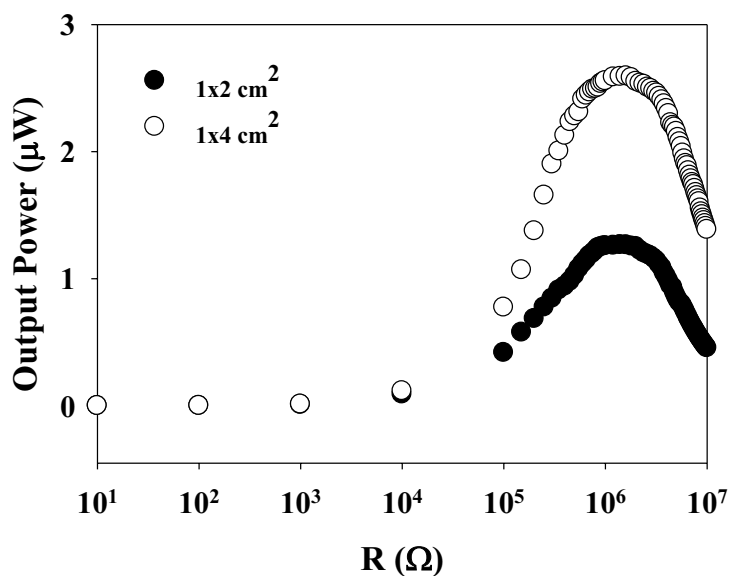
Figure 5.24 Experimental harvested power as a function of resistive load for 28 μm-commercial PVDF
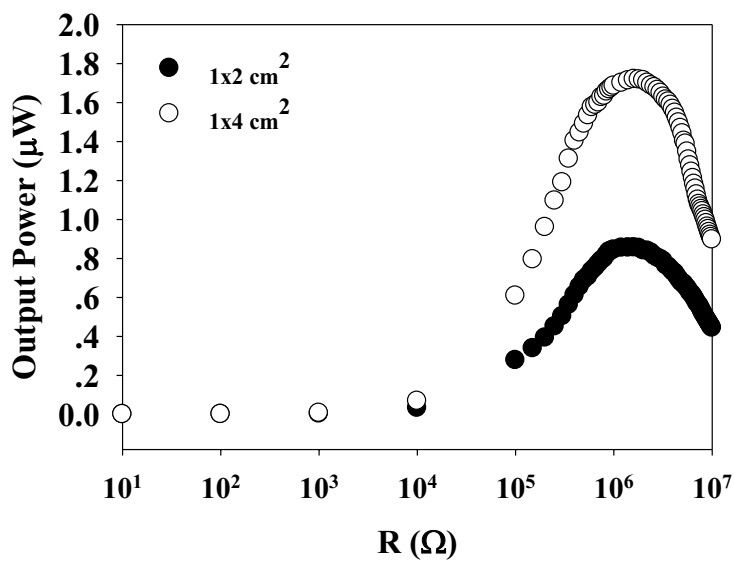
Figure 5.25 Experimental harvested power as a function of resistive load for 52 μm-commercial PVDF.
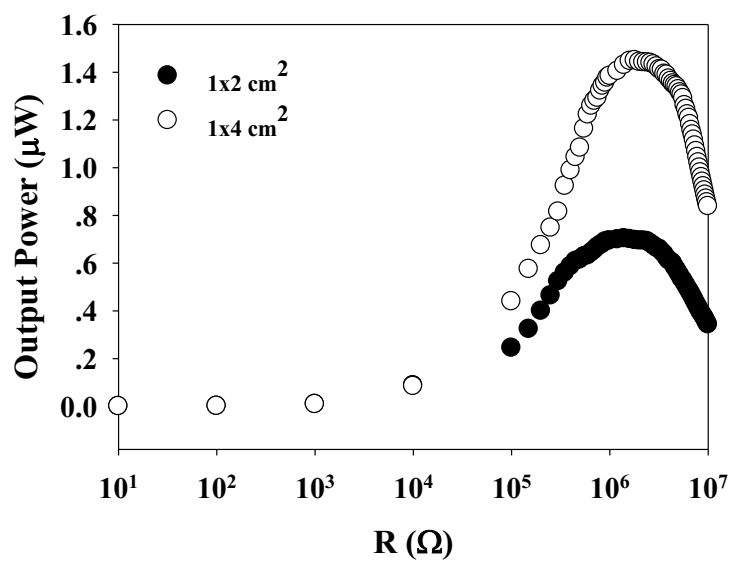
Figure 5.26 Experimental harvested power as a function of resistive load for 50 μm-poled PVDF.
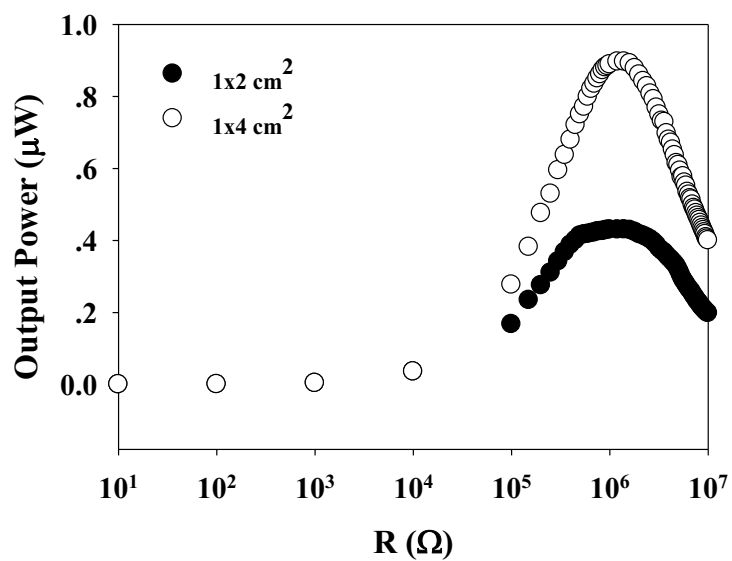
Figure 5.27 Experimental harvested power as a function of resistive load for 100 μm-poled PVDF.
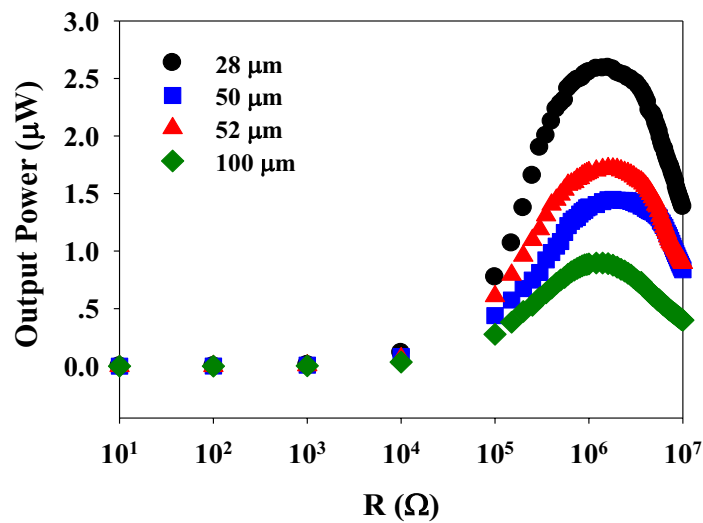
Figure 5.28 Experimental harvested power as a function of resistive load for all the PVDF sample of the dimension of 1x4 cm^2.

Table 5.2 Energy harvesting ability comparison

Sample thickness (μm)	$V_{DC(max)}$ (V)	$P_{(max)}$ (μm)	$I_{(max)}$ (μA)	Power density$_{(max)}$ (μm·cm^{-3})
28	2.0	2.6	1.3	229.6
50	1.6	1.4	0.9	72.5
52	1.7	1.7	1.0	82.7
100	1.1	0.9	0.8	22.4

5.4 Conclusions

The piezoelectric activity in the PVDF material strongly depends upon the active volume within the crystalline phase of the polymer. PVDF is a low coupling material and it is thus important in adjusting the material properties and interfaced circuit. The prepared PVDF could harvest energy from vibration to useful electrical power and reach the value of an order of 2 μW for the matching load of 1.6 MΩ at a relatively low operating frequency (Roundy *et al*., 2003). These polymers

can thus be utilized as energy resources. The implementation of various electrical circuits to enhance its electrical output is challenging.

CHAPTER 6

CONCLUSION AND FUTURE WORKS

6.1 Main Conclusions

Piezoelectric materials have long been used in various application fields. The field where the piezoceramic PZT and piezopolymer such as PVDF have great potential is in energy harvesting. This work paid attention to the fabrication of the PVDF polymer and altered its material properties by adding conductive filler of low density and high electron density like copper into the PVDF matrix. In this work the copper particles of micrometer and nanometer dimensions were dispersed homogeneously in the PVDF matrix in which the nonionic Brij-30 surfactant was priorily added. The optical and electron microscopic techniques including the AFM were used to investigate the uniformity of the filler in the composite samples. The FTIR analysis confirmed that the dispersion of the copper filler was improved by adding the Brij-30. From the abrupt change in dielectric and electrical properties of the composite at the volume fraction 0.6 of the filler, the percolation threshold could be deduced. This is an extraordinarily high volume fraction, resulting from the use of the surfactant. The composite with the surfactant below 0.05% and the filler of micron size had the dielectric constant measured at 1 kHz of 3. This value is 8 for the composite with nanofiller and the same amount of the surfactant. These composites were, however, of too high dielectric loss (>1). The temperature-dependence dielectric properties of the latter were further studied. The relaxation behavior as increasing frequency was found in the composite. The composite with the low content of the nanofiller, i.e. 4% possesses the capacitance measured at 100 Hz of more than 0.5 nF (ε_r 50). This value is in a useful range in energy harvesting and this implies that the composites with the high content of the fillers are not necessary for energy harvesting application. However, in the following energy conversion measurements, the composite with nanofiller was always ruptured. This was likely due to the fact that the composite still contained tiny clusters of the filler which became the origin of the

failure of the sample under testing. The neat PVDF element was then chosen for further studies on converting the low frequency vibration into a usable electrical energy. The comparison was first made between two compositions of the well-known piezoceramics, i.e. PMN-PT and Mn-PZT using either standard or SSHI harvesting circuit. It was found that the latter enhanced the energy conversion in both compositions with a small discrepancy in energy conversion capability. The power of more than 10 microwatt (PMN-PT) obtained from the piezoceramics was high enough to be dissipated in related circuitry and thus the self-powering vibrating system could be carried out in this case. When the concept of nonlinear processing was applied to the stretched and poled PVDF element, the output power was not obtained. The standard circuit was then selected in this case. At a resonance of 60-70 Hz of the vibrating system with the PVDF sample attached onto the beam and a constant amplitude of the displacement of the beam, the output power of 2 μW was delivered by the PVDF element at the matching load of 1.6 MΩ. It is interesting to note that although the piezoceramics were compatibe with the non-linear technique, the power density is 15-30 μW$\cdot$cm^{-3} which is less than that of the PVDF (22-70 μW$\cdot$cm^{-3}) obtained by using the standard approach. Therefore, the PVDF material is highly promising as a candidate in energy harvesting. It is important that both the material property and the interconnected electronics are taken into account. The implementation of the PVDF element into a technological advancement in energy harvesting applications and related technologies such as wireless sensor, portable electronics and self-powered device is necessary to do further investigation.

6.2 Future Works

Some difficulties which arose during the course of this work are:

(a) the high dielectric loss in PVDF composites,

(b) the agglomeration of the fillers in the PVDF ,

(c)   the limitation of using the self-powered SSHI circuit for energy harvesting on PVDF material,

The following topics are of interest for further study:

(a) the development of an interface circuit for low-coupling coefficient materials such as PVDF,

(b) an enhancement in energy conversion harvested with PVDF or other promising polymers such as poly(vinylidene-hexafluorpropylene) or (P(VDF-HFP)) copolymer and polyurethane elastomer.

REFERENCES

Abdelaziz, M. 2004. Characterization, electrical and magnetic properties of PVDF films filled with $FeCl_3$ and $MnCl_2$ mixed fillers, *Journal of Magnetism and Magnetic Materials* 279: 184-194.

Anton, S.R. and Sodano, H.A. 2007. A review of power harvesting using piezoelectric materials (2003–2006). *Smart Materials and Structure* 16**:**R1–R21.

Arnold, D. 2007. Review of microscale magnetic power generation. *IEEE Transactions on Magnetics* 43:3940–3951.

Badel, A. 2005. Récupération d'énergie et contrôle vibratoire par elements piézoélectriques suivant une approche non linéaire. PhD thesis, Université de Savoie/ INSA de Lyon, In Lallart, M. 2008. Amélioration de la conversion électroactive de matériaux piézoélectriques et pyroélectriques pour le contrôle vibratoire et la récupération d'énergie - Application au contrôle de santé structural auto-alimenté. PhD thesis, Université de Savoie / INSA de Lyon.

Badel, A., Benayad, A., Lefeuvre, E., Lebrun, L., Richard, C. and Guyomar, D. 2006. Single Crystals and Nonlinear Process for Outstanding Vibration Powered Electrical Generators. *IEEE Transaction on Ultrasonics, Ferroelectrics, and Frequency Control* 53:673-684.

Badel, A., Lagache M., Guyomar D., Lefeuvre E. and Richard C. 2007. Finite Element and Simple Lumped Modeling for Flexural Nonlinear Semi-passive Damping. *Journal of Intelligent Material Systems and Structure* 18:727-742.

Badel, A., Sebald, G., Guyomar, D., Lallart, M., Lefeuvre, E., Richard, C., Qiu, J. 2006a.Wide Band Semi-Active Piezoelectric Vibration Control by Synchronized Switching on Adaptive Continuous Voltage Sources. *Journal of the Acoustical Society of America* 119:2815–2825.

Badel, A., Sebald, G., Guyomar, D., Lallart, M., Lefeuvre, E., Richard, C. and Qiu, J. 2006b. Piezoelectric vibration control by synchronized switching on adaptive voltage sources: Towards wideband semi-active damping. *Journal of the Acoustical Society of America* 119:2815-2825.

Bahadorimehr, A. 2010. Micro-Electro-Mechanical Systems (MEMS). http://bahadorimehr.blogspot.com/ (2010 September 23).

Baker, J., Roundy, S. and Wright, P. 2005. Alternative geometries for increasing power density in vibration energy scavenging for wireless sensor networks *Proceeding 3rd International Energy Conversion Engineering Conference, San Francisco, CA, August,* pp. 959–70.

Beeby, S.P., Tudor, M.J. and White, N.M. 2006. Review Article Energy harvesting vibration sources for microsystems applications. *Measurment Science and Technololy* 17:R175–R195.

Boucher, E., Guiffard, B., Lebrun, L. and Guyomar, D., 2004. Influence of the niobium orfluorine concentration on the properties of Mn doped lead zirconate titanate ceramics. *Journal Applied Physics* 43:5378-538.

Bur, A.J., Barnes, J.D. and Wahlstrand, K.J. 1986. A study of thermal depolarization of polyvinylidene fluoride using X-ray pole-figure observations. *Journal of Applied Physics* 59:2345–54.

Camposa, J.S., Ribeiro, A.A. and Cardoso, C.X. (2007). Preparation and characterization of PVDF/CaCO$_3$ composites. *Materials Science and Engineering B* 136:123–128.

Carpi, F. and Smela, E. 2009. *Biomedical Applications of Electoactive Polymer Actuators*. UK:Wiley.

Chandrakasan, A., Amirtharajah, Goodman, R. J., Rabiner, W., 1998. Trends in low power digital signal processing. *Proceedings of the 1998 IEEE International Symposium on Circuits and Systems* 604-607.

Choi, W.J., Jeon, Y., Jeong, J.H., Sood, R. and Kim, S.G. 2006. Energy Harvesting MEMS Device Based on Thin Film Piezoelectric Cantilevers, *Journal of Electroceramics* 17:543–548.

Dang, Z.M., Wu, J.P., Xu, H.P. Yao, S.H. and Jiang, M.J. 2007. Dielectric properties of upright carbon fiber filled poly(vinylidene fluoride) composite with low percolation threshold and weak temperature dependence. *Applied Physics Letters* 91:072912-3.

Dasaesamoh, A. 2008. Dielectric Transducer Fabricated from Polymer-Matrix Composite. M.Sc. Thesis. Faculty of Science. Prince of Songkla University, Thailand.

Dasaesamoh, A., Muensit S., Lertsuriwat, P. and Sirisathitkul, C. 2009. Fabrication of Magnetic PVDF Composites, Poster Presentational at Siam Physics Congress 2009, March 2009, Petchaburi, Thailand.

Dasgupta, D.K., Doughty, K. and Brockley, R.S. 1980. Charging and discharging currents in polyvinylidene fluoride. *Journal Physics D: Applied Physics* 13: 2101.

Davis, C.L. and Lesieutre, G.A. 2000. An actively tuned solid-state vibration absorber using capacitive shunting of piezoelectric stiffness. *Journal of Sound and Vibration* 232(3):601-617.

Davis, G.T., Mckinney, J.E., Broadhurst, M.E., Roth, S.C. 1987. *Journal of Applied Physics* 49:4998.

Davis, W. R., Zhang, N., Camera, K., Chen, F., Markovic, D., Chan, N., Nikolic, B., Brodersen, R. W., 2001. A design environment for high throughput, low power dedicated signal processing systems. *Proceedings of the IEEE 2001 Custom Integrated Circuits Conference* 545-8.

Dias, C.J. and Das-Gupta, D.K. (1996). Inorganic ceramic/polymer ferroelectric composite electrets. *IEEE Transaction on Dielectrics and Electrical Insulation* 3(5): 706-734.

Dias, C.J. and Das-Gupta, D.G. 1996. *IEEE Transaction Dielectric Electronics Insulation* 3:706.

Dvey-Aharon, H., Sluckin, T.J., Taylor, P.L. and Hopfinger, A.J. 1980. Kink propagation as a model for poling in poly(vinylidene fluoride). *Physics Review B* 21:3700–7.

Eberle, G. and Eisenmenger, W. 1991. Dynamics of poling PVDF between 25 $^{\circ}$C and 120 $^{\circ}$C. CH3029-6/91/0000-0388 Copyright 1991 IEEE. 388-393.

Eric, O. Torres, Gabriel, A., Mora, R. 2005. Long-Lasting, Self-Sustaining, and Energy-Harvesting System-in-Package (SiP) Wireless Micro-Sensor Solution. International Conference on Energy, Environment and Disasters (INCEED 2005), July 24-30, 2005, Charlote, NC, USA. 1-33.

Fang, H.B., Liu, J.Q., Xu, Z.Y., Dong, L., Chen, D., Cai, B.C. and Liu, Y. 2006. A MEMS Based Piezoelectric Power Generator for Low Frequency Vibration Energy Harvesting. *Chinese Physics Letters* 23:732-734.

Fishcher, J.E., Dai, H., Thess, A., Lee, R., Hanjani, N.M., Dehaas, D.L. and Smalley, R.E. 1997. Metallic resistivity in crystalline ropes of single-wall carbon nanotubes. *Physics Review B* 55:15-18.

Flapping leaf generator for wind energy harvesting. 2009. Energy Harvesting Journal. http://www.energyharvestingjournal.com/articles/flapping-leaf-generator-for-wind-energy-harvesting-00001791.asp?sessionid=1 (2010 November 23).

Fourie, D. "n.d." Shoe-Mounted PVDF Piezoelectric Transducer for Energy Harvesting Manuscript to be submitted to the Journal of Intelligent Material Systems and Structures, http://web.mit.edu/dfourie/www/PaperNicePrint2.pdf. (2010 October 5).

Gandhi, F. and Chapuis, G. 2002. Passive damping augmentation of a vibrating beam using pseudoelastic shape memory alloy wires. *Journal of Sound and Vibration* 250:519–539.

Gentry, C.A., Guigou, C. and Fuller, C.R. 1997. Smart foam for applications in passive–active noise radiation control, *Journal of the Acoustical Society of America* 101:1771-1778.

Gerald, R.H., Roy, C.P. and Aime, S.D. 2000. The Impact of Piezoelectric PVDF on Medical Ultrasound Exposure Measurements, Standards, and Regulations1. *IEEE transactions on ultrasonics, ferroelectrics, and frequency control* 47:1321-1334.

Glatkowski, P.J. 2003. Carbon nanotube based transparent conductive coating, In 48th International SAMPE Symposium, 2146-2152.

Glynne-Jones, P., Tudor, M. J, Beeby, S. P. and White N. M. 2004. An electromagnetic, vibration powered generator for intelligent sensor systems. *Sensors and Actuators A* 110:344–349.

Greorio, R. and Cestari, M. 1994. *Journal of Polymer Science Part B: Polymer Physics* 32:859.

Gross, B., Seggern, H.V. and Gerhard-multhaupt, R. 1985. Carrier mobilities in poly(vinylidene fluoride). *Journal Physics D* 18:2497.

Guyomar, D., Badel, A., Lefeuvre, E., and Richard, C. 2005. Towards energy harvesting using active materials and conversion improvement by nonlinear processing. *IEEE Transaction on Ultrasonics, Ferroelectrics, and Frequency Control* 52:584-595.

Guyomar, D., Lebrun, L. , Putson, C. , Cottinet, J.P., Giffard, B. and Muensit, S. 2009. Electrostrictive energy conversion in polyurethane nanocomposites. *Journal of Applied Physics* 106:014910.1-014910.9.

Guyomar, D., Sebald, G., Pruvost, S., Lallart, M., Khodayari, A., and Richard, C., 2009. Energy Harvesting from Ambient Vibrations and Heat. *Journal of Intelligent Material Systems and Structure* 20: 609-624.

Guyomar, D., Richard, C., Badel, A., Lefeuvre, E. and Lallart, M. 2009. Chapter 8 Energy Harvesting using Non-linear Techniques. In *Energy Harvesting Technologies*. Priya, S. and · Inman, D.J. New York:Springer.

Hajeesae, S. and Muensit, S. 2006. Theory and measurements for 0-3 $BaTiO_3$/PVDF composite. *Songklanakarin Journal of Science and Technology* 2:413-418.

Han, J., Von-Jouanne, A., Le, T., Mayaram, K., and Fiez, T.S. 2004. Novel power conditioning circuits for piezoelectric micro power generators. *In Proceeding IEEE Applied Power Electronics Conference and Exposition* (APEC), 3:1541-1546.

Heat of Fusion / Crystallization / Melting Point / Glass Transition by DSC (Differential Scanning Calorimeter. 2010. Intertek Plastics Technology Laboratories, http://www.ptli.com/testlopedia/tests/DSC-d3417.asp (2010 November 23).

Hongbing, S., Liqing, X., Jun, C. et al. 1998. Radiation effects of poly(vinylidene fluoride) (PVDF) (I) Mechanism of accelerating damage of crystal in high dose zone, *Science in China (Series A)* 41:438-442.

Horowitz, S. B., Sheplak, M., III, L. N. C. and Nishida, T. 2006. A MEMS Acoustic Energy Harvester. *Journal of Micromechanics and Microengineering* 16: S174–S181.

Hosokawa, M., Nogi, K., Naito, M. and Yama, T. 2007. *Nanoparticle technology handbook*. pp.5-20. Netherlands:Elsevier.

Ikeda, T. 1990. Fundamentals of Piezoelectricity. New York:Oxford University.

Introduction to Fourier Transform Infrared Spectrometry. 2010. Thermonicolet cooperation.. http://mmrc.caltech.edu/FTIR/FTIRintro.pdf (2010 September 23).

Iwauchi, K. 1960. *Journal of Applied Physics* 10:1520.

Jaffe, B., Roth, R.S. and Marzull, S. 1954. Piezoelectric properties of lead zirconate-lead titanate solid-solution ceramics. *Journal of Applied Physics* 25: 809-810.

Jeon, Y. B., Sood, R., Jeong, J. H. and Kim, S. 2005. MEMS power generator with transverse mode thin film PZT. *Sensors & Actuators A* 122:16–22

Jonscher, A. K. 1983. Dielectric Relaxation in Solids. London:Chelsea Dielectric Press.

Johnson, C. D. 1995. Design of passive damping systems. *Journal of Vibration and Acoustics* 117:171–176.

Kakutani, K. 1970. Dielectric absorption in oriented poly(vinylidene fluoride). *Journal of Polymer Science A -2: Polymer Physics* 8:1177.

Kaurat, T., Natht, R. and Perlman, M.M. 1991. Simultaneous stretching and corona poling of PVDF films. *Journal of Physics D: Applied Physics* 24:1848-1852.

Kawai, H. 1969. The Piezoelectricity of Polyvinylidene Fluoride. *Japan Journal of Applied Physics* 8:975-976.

Kelly, J., Leonard, M., Tantigate, C. and Safari, A., 1997. Effect of Composition on the Electromechanical Properties of (1−x)Pb(Mg1/3Nb2/3)O3xPbTiO3 Ceramics. *Journal of the American. Ceramic Society* 80:957964.

Kepler, R.G, Anderson, R.A. 1978. Ferroelectricity in polyvinylidene fluoride. *Journal of Applied Physics* 49:1232–5.

Kima, K.M., Park, N.-G., Ryu, K.S. and Chang, S.H. 2006. Characteristics of PVdF-HFP/TiO$_2$composite membrane electrolytes prepared by phase inversion and conventional casting methods Electrochimica Acta 51: 5636-5644.

Kobayashi, Y., Tanase, T., Tabata, T., Miwa T.,and Konno, M. 2008. Fabrication and dielectric properties of the BaTiO$_3$–polymer nano-composite thin films. *Journal of the European Ceramic Society* 28:117-122.

Kumart, A. and Perlman, M.M. 1993. Simultaneous stretching and corona poling of PVDF and P(VDF-TriFE) films. II. Journal of Physics D: Applied Physics 26:469-473.

Kymissis, J., Kendall, C., Paradiso, J. and Gershenfeld, N. 1998. Parasitic power harvesting in shoes *Proceeding. 2nd IEEE International Conference. Wearable Computing, California,* pp. 132-9.

Jonscher, A. K. 1983. *Dielectric Relaxation in Solids*. London:Chelsea Dielectric Press.

Lallart, M. 2008. Amélioration de la conversion électroactive de matériaux piézoélectriques et pyroélectriques pour le contrôle vibratoire et la récupération d'énergie - Application au contrôle de santé structural auto-alimenté. PhD thesis, Université de Savoie / INSA de Lyon,

Lallart, M., Garbuio, L., Petit, L., Richard, C., and Guyomar, D., 2008. Double Synchronized Switch Harvesting (DSSH): A New Energy Harvesting Scheme For Efficient Energy Extraction *IEEE Transaction on Ultrasonics, Ferroelectrics, and Frequency Control* 55:2119-2131.

Lallart, M., and Guyomar, D., 2008. An optimized self-powered switching circuit for nonlinear energy harvesting with low voltage output. *Smart Material and Structure 17:*1-8.

Lallart, M., Guyomar, D., Jayet, Y., Petit, L., Lefeuvre, E., Monnier, T., Guy, P., and Richard, C., 2008. Synchronized Switch Harvesting applied to Selfpowered Smart Systems : Piezoactive Microgenerators for Autonomous Wireless Receiver. *Sensors and Actuators A: Physical* 147:263-272.

Lallart, M., Lefeuvre, E., Richard, C. and Guyomar, D., 2008. Self-Powered Circuit for Broadband, Multimodal Piezoelectric Vibration Control. *Sensor & Actuator. A: Physics* 143:277- 382.

Lang, S.B. and Muensit, S. 2006. Review of some lesser-known applications of piezoelectric and pyroelectric polymers. *Applied Physics A: Materials and Processing* 85:125-134.

Law, H.H., Rossiter, P.L., Simon, G.P. and Koss, L.L.1996. Characterization of mechanical vibration damping by piezoelctric materials. *Journal of Sound and Vibration* 197:489-513.

Lee, I. and Sung, H.J. 1999. Development of an array of pressure sensors with PVDF film. *Experiments in Fluids* 26:27-35.

Lefeuvre, E., Audigier, D., Richard, C., and Guyomar, D. 2007. Buck-boost converter for sensorless power optimization of piezoelectric energy harvester. *IEEE Transaction Power Electron* 22(5):2018-2025.

Lefeuvre, E., Badel, A., Petit, L., Richard, C., Guyomar, D. 2006a. Semi Passive Piezoelectric Structural Damping by Synchronized Switching on Voltage Sources. *Journal of Intelligent Material Systems and Structure* 17:653–660.

Lefeuvre, E., Badel, A., Richard, C., Petit, L., and Guyomar, D., 2006b. A comparison between several vibration-powered piezoelectric generators for standalone systems. *Sensor & Actuators A* 126:405-416.

Li, Y.J., Xu, M., Feng, J.Q. and Dang, Z.M. 2006. Dielectric behavior of a metal-polymer composite with low percolation threshold. *Applied Physics Letter* 89**.**

Liang, X.Y, Campopiano, D.J. and Sadler, P.J. 2007. *Chemical Society Reviews Articles* 36:968–92.

Lin, C., Wang, H. and Yang, W. 2010. Variable percolation threshold of composites with fiber fillers under Compression. *Journal of Applied Physics* 108:013509.

Liu, Y., Yu, J., Wang, X. and Chen, X. 2002. Effects of drawing temperature on phase transition in poly(vinylidene fluoride) films. *Ferroelectrics* 273:3-8.

Lovinger, A. J. 1981. Crystallization of the beta-phase of poly (vinylidene fluoride) from the melt. *Polymer* 22:412-413.

Lovinger, A.J. 1982. In Developments in Crystalline Polymers, edited by D. C. Bassett. London and New Jersey:Applied Science.

Lovinger, A. 1982. *Poly(viylidene fluoride), in Developments in Crystalline Polymers-1*. London: Applied Science Publishers.

Lovinger, A. J. 1983. Ferroelectric Polymer. *Science* 220:1115-1121.

Lu, F., Lee, H. P. and Lim, S. P. 2004. Modeling and Analysis of Micro Piezoelectric Power Generators for Micro-Electro-Mechanical-Systems Applications. *Smart Materials and Structures* 13: 57-63.

Maaroufi, A., Haboubi, K., Amarti, A.E. and Carmona, F. 2004. Electrical resistivity of polymeric matrix loaded with nickel and cobalt powders, *Journal of Material Science* 39: 265-270.

Mani, S. Surface characterization of polyvinylidene fluoride (PVDF) in its application as an actuator master of science. (2007). Mechanical Engineering Submitted to the Office of Graduate Studies of Texas A&M University.

Mason, W.P. and Jafee, H. 1954. Methods for measuring Piezoelectric, Elastic, and Dielectric Constants of Crystals and Ceramics. *Proceedings of the IRE*. 42:921-930.

Mazen, S.A. and Zaki, H.M. 2003. Effect of tetra ionic substitution on the dielectric properties of Cu-ferrite. *Physica Status Solidi (a)* 199:305-320

Mitcheson, P., Miao, P., Start, B., Yeatman, E., Holmes, A. and Green, T. 2004. MEMS electrostatic micro-power generator for low frequency operation. *Sensors and Actuators A* 115:523–529.

Moisala, A., Li, Q., Kinloch, I.A. and Windl, A.H. 2006. Thermal and electrical conductivity of single- and multi-walled carbon nanotube-epoxy composites, *Composites Science and Technology* 66:1285-1288.

Myers, D. 2006. *Surfactant science and technology*. USA:Wiley-interscience.

Naegele, D. and Yoon, D.Y. 1978. Orientation of crystalline dipoles in poly(vinylidene fluoride) films under electric field. *Applied Physics Letter* 33:132–4.

Nakagawa, K. and Ishida, Y. 1973. Dielectric relaxations and molecular motions in poly(vinylidene fluoride) with crystal form II. *Journal of Polymer Science: Polymer Physics Edition* 11 : 1503.

Ng, T.H., and Liao, W.H., 2005. Sensitivity analysis and energy harvesting for a selfpowered piezoelectric sensor. *Journal of Intelligent Material System and Structure* 16:785-797.

Ng, W.Y., Ploss, B.H., Chan L.W., Shin, F.G. and Choy, C.L. 2000. *In Proceeding. 12th IEEE International Symposium Applications Ferroelectrics* 2:767.

Nicolais, L. and Carotenuto, G. 2005. *Metal-polymer nanocomposites*. USA:Wiley-interscience.

Osaki, S., Uemura, S. and Ishida, Y. 1971. *Journal of Polymer Science Polymer Physics* 9: 585.

Ottman, G. K., Hofmann, H. F., Bhatt, A. C. and Lesieutre, G. A. 2002. Adaptive Piezoelectric Energy Harvesting Circuit for Wireless Remote Power Supply. *IEEE Transaction Power Electron* 17(5):669-676.

Ottman, G.K., Hofmann, H.F. and Lesieutre, G.A. 2003. Optimized piezoelectric energy harvesting circuit using step-down converter in discontinuous conduction mode. *IEEE Transaction Power Electron* 18:696-703.

Paradiso, J.A. and Starner, T. 2005. Energy scavenging for mobile and wireless electronics. *IEEE Pervasive Computing* 4:18-27.

Park, J-M., Kim, S-J., Jang, J-H., Wang, Z., Kim, P-G., Yoon, D-J., Kim, J., Hansen, G. and DeVries, K. L. 2008. Actuation of electrochemical, electro-magnetic, and electro-active actuators for carbon nanofiber and Ni nanowire reinforced polymer composites. *Composites: Part B* 39:1161–1169.

Park, S.E., Lopath, P.D., Shung, K.K., and Shrout, T.R., 1997. Relaxor-based single crystal materials for ultrasonic transducer application. *Material Research Innovations* 1:20-25.

Pantelis, P. 1984. Molecular electronics: 2 Properties and applications of piezoelectric polymers. *Physics Technology* 15:239-261.

Priya, S. and Inman D.J., eds, 2005. *Energy Harvesting Technologies*. New York:Springer Science.

Rabaey, J., Ammer, J., Karalar, T., Li, S., Otis, B., Sheets, M. and Tuan, T. 2002. PicoRadios for Wireless Sensor Networks: The Next Challenge in Ultra- Low-Power Design. *Proceedings of the International Solid-State Circuits Conference*, San Francisco, CA, February 3-7.

Rakbamrung, P. and Muensit, N. 2010. Low- and high-loaded electroactive polyvinylidene fluoride polymers**. *Journal of Material Science Engineering* 4:23.

Reddy, M. B., Reddy, P.V. 1991. Low-frequency dielectric behaviour of mixed Li-Ti ferrites. *Journal Physics D: Applied Physics* 24:975-981.

Rothon, R.N. 2002. Particulate Fillers for Polymers, Summary,1st Ed., ChenTec:UK Quoted in Abdelaziz, M. 2004. Characterization, electrical and magnetic properties of PVDF films filled with FeC_{l3} and MnC_{l2} mixed fillers, *Journal of Magnetism and Magnetic Materials* 279:184-194.

Roundy, S. J. 2003. Energy scavenging for wireless sensor nodes with a focus on vibration to electricity conversion. Engineering PhD Thesis, The University of California, Berkeley.

Roundy, S.,Wright, P. K. and Rabaey, J. 2003. A Study of Low Level Vibrations as Power Source for Wireless Sensor Nodes. *Computer Communications* 26: 1131–1144.

Sadiku, M.N.O. 1995. Elements of Electromagnetics. New York:Oxford University Press Inc.

Sawyer, L.C. and Grubb, D.T.. 1996. *Polymer Microscopy*. pp. 98. UK:Chapman & Hall.

Sebald, G., Benayad, A., Qiu, J., Guiffard, B. and Guyomar, D. 2006. Electromechanical characterization of $0.55Pb(Ni_{1/3}Nb_{2/3})O_30.45Pb(Zr_{0.3}Ti_{0.7})$-$O_3$ fibers with Pt core. *Journal Applied Physics* 100:054106.

Sebald, G., Lefeuvre, E. and Guyomar, D. 2008. *IEEE transactions on ultrasonics, ferroelectrics, and frequency control* 55:538.

Sebald, G., Seveyrat, L., Guyomar, D., Lebrun, L., Guiffard, B. and Pruvost, S., 2006. Electrocaloric and pyroelectric properties of 0.75Pb(Mg1/3Nb2/3)O3 − 0.25PbTiO3 single crystals. *Journal Applied Physics* 100:124112.

Serguei, M.L., Olga, S.G. and Serguei, N.T. 2009. Metal-polymer PVDF/nickel composites and evaluation of their dielectric and thermal properties. *Journal of Electrostatics* 1-6.

Shenck, N.S. and Paradiso, J.A. 2001. Energy scavenging with shoe-mounted piezoelectrics *IEEE Micro.* 21**:**30-42.

Shin, H., Kim, H., Ha, J., Lim, K.-S. and Lee, M. 2008. Langmuir–Blodgett Ag nanoparticle monolayer patterned by pulsed laser-induced selective desorption. *Superlattices and Microstructures* 44:657-663.

Shu, Y. C. and Lien, I. C. 2006b. Efficiency of Energy Conversion for a Piezoelectric Power Harvesting System. *Journal of Micromechanics and Microengineering* 16: 2429–2438.

Smith, J.G., Connell, J.W., Delozier, D.M., Lillehei, P.T., Watson, K.A., Lin, W., Zhou, B. and Sun, Y.-P. 2004. Space durable polymer/carbon nanotube films for electrostatic charge mitigation. *Polymer* 45:825-836.

Sodano, H., Inman, D., and Park, G. 2005. Generation and storage of electricity from power harvesting devices. *Journal of Intelligent Material Systems and Structures* 16:67–75.

Suh, D-H., Lee, D-H., and Kim, N-K. 2002. Phase developments and dielectric / ferroelectric responses in the PMN − PT system. *Jornal of the European Ceramic Society* 22:219-223.

Sun, J. Q., Jolly, M. R. and Norris, M. A. 1995. Passive, adaptive and active tuned vibration absorbers - a survey. *ASME Transactions* 117 :234–242.

Tashiro, K. 1995. Crystal structure and phase transition of PVDF and related copolymers. In: Nalwa H.S. *Ferroelectric polymers: chemistry, physics, and applications.* 63-181. New York: Marcel Dekker.

Taylor, G.W., Gagnepain, J.J., Meeker, T.R., Nakamura, T. and Shuvalov, L.A. 1985. *Piezoelectricity.* New York:Gordon and Breach Science Publishers.

Tawansi, A., Oraby, A.H., Abdelrazek, E. M., Ayad, M. I., and Abdelaziz M. 1998. Effect of Local Structure of $MnCl_2$-Filled PVDF Films on Their Optical, Electrical, Electron Spin Resonance, and Magnetic Properties. *Journal of Applied Polymer Science,* 70:1437–1445.

Tim, R., Dargaville, M.C., Celina, J.M., Elliott, P.M., Chaplya, G.D., Jones, D.M., Mowery, R.A., et al. 1998. *Ferroelectrics* 216:63.

Tim, R. Dargaville, M.C., Celina, J.M., Elliott, P.M., Chaplya, G.D., Jones, D.M., Mowery, R.A., et al. 2005. Characterization, Performance and Optimization of PVDF as a Piezoelectric Film for Advanced Space Mirror Concepts, 2005. Sandia National Laboratories SAND2005-6846: California.

Thipmonta N, 2006. Pyrohysteresis of Ferroelectric Polymers. Master of Science Thesis, Department of Physics, Faculty of Science, Prince of Songkla University.

Wang, L. and Dang, Z-M. 2005. Carbon nanotube composites with dielectric constant at low percolation threshold. *Applied Physics Letters* 87: 042903-3.

Wang, T.T., Herbert, J.M. and Glass, A.M. 1988. *The Applications of Ferroelectric Polymer.* New York:Blackie.

Williams, C.B. and Yates, R.B. 1996. Analysis of a Micro-Electric Generator for Microsystems. *Sensors and Actuators A* 52: 8–11.

Wu, C.-G., Lu, M.-I., Tsai, C.C. and Chuang, H.J. 2006. PVdF-HFP/metal oxide nanocomposites: The matrices for high-conducting, low-leakage porous polymer electrolytes, *Journal of Power Sources* 159: 295-300.

Xie, J., Mane, X. P., Green, C.W., Mossi, K.M. and Leang K.K. 2010. Performance of Thin Piezoelectric Materials for Pyroelectric Energy Harvesting. *Journal of Intelligent Materials Systems and Structures* 21:243-249.

Xu, H-P., Dang, Z-M., Yao, S-H. and Jiang, M-J. 2007. Exploation of unusual electrical properties in carbon black/binary-polymer nanocomposites. *Applied Physics Letters* 90:152912-3.

Yamada, H., 1999. Pressureless Sintering of PMN-PT Ceramics. *Journal of the European Ceramic Society* 19:1053-1056.

Yao, S-H., Dang, Z-M., Jiang, M-J. and Xu. H-P. 2007. Influence of aspect ratio of carbon nanotube on percolation threshold in ferroelectric polymer nanocomposite. *Applied Physics Letters*, 91:212901-3.

Zhai, Y., Liu, Y., Chang, X., Ruan, X. and Liu, J. 2008. Metal ion-small molecule complex imprinted polymer membranes: Preparation and separation characteristics. *Reactive & Functional Polymers* 68:284–291.

Zhang Q. 2004. Effects of Mn doping on the ferroelectric properties of PZT thin films*, Journal of Physics D: Applied Physics*, 37:98-101.

Zhu, G.D., Zeng, Z.G., Zhang, L. and Yan, X.J. 2008. Piezoelectricity in b-phase PVDF crystals: A molecular simulation study. *Computational Materials Science* 44:224-229.

VITAE

Name   Ms. Prissana Rakbamrung

Student ID   5010230027

Educational Attainment

Degree	Name of Institution	Year of Graduation
B.Sc.(Physics)	Prince of Songkla University	2003
M.Sc.(Physics)	Prince of Songkla University	2007

Scholarship Awards during Enrolment

Partenariat Hubert Curien (PHC) Program (Grant No. 20591ZL), 9/2009-12/2009

PhD Fellowship, Prince of Songkla University (Grant No. 950002), 2007-2010

NANOTEC Center of Excellence at PSU, 2010

List of Publications and Proceedings

Publications

1. **Rakbamrung, P.** and Muensit, N. 2010. Low- and high-loaded electroactive polyvinylidene fluoride polymers, *Journal of Materials Science and Engineering* 4:23-31.

2. **Rakbamrung, P.**, Lallart, M., Guyomar, D., Muensit, N., Thanachyanont, C., Lucat, C., Guiffard, B., Petit, L., and Sukwisut, P. 2010. Performance comparison of PZT and PMN-PT piezoceramics for vibration energy harvesting using standard or nonlinear approach, *Sensor and Actuators A: Physical* 163:493-500.

Proceedings

1. **Rakbamrung, P.** and Muensit, S. 2008. Electroactive polymer composites for applications in electronic devices. The 2nd Thailand Nanotechnolog Conference [TNC] Nanomaterials 2008 for Health, Energy and Environment, 13-15 August, 2008, Phuket, Thailand.

2. **Rakbamrung, P.** and Muensit, N. 2010. Low and high content nano-loaded electroactive polyvinylidene fluoride polymer. IEEE International Nano Electronics Conference (INEC), 3-8 January 2010, Hong Kong, China.

3. Nantakan Muensit, **Panu Thainiramit** and Prissana Rakbamrung. 2011. Mechanical-to-electrical energy harvested with polyvinylidene fluoride. Siam Physics Congress SPC2011 Physics for all, 23-26 March 2011, Kanchanaburi, Thailand.